

Technische Universität München  
Max-Planck-Institut für Astrophysik

---

SIMULATION OF AXISYMMETRIC  
FLOWS IN THE CHARACTERISTIC  
FORMULATION OF GENERAL  
RELATIVITY

---

**Florian Siebel**

Dissertation



Technische Universität München  
Max-Planck-Institut für Astrophysik

# Simulation of axisymmetric flows in the characteristic formulation of general relativity

**Florian Siebel**

Vollständiger Abdruck der von der Fakultät für Physik der Technischen Universität München zur Erlangung des akademischen Grades eines

**Doktors der Naturwissenschaften**

genehmigten Dissertation.

Vorsitzender: Univ.-Prof. Dr. Franz von Feilitzsch

Prüfer der Dissertation: 1. Priv.-Doz. Dr. Ewald Müller  
2. Univ.-Prof. Dr. Manuel Drees

Die Dissertation wurde am 28.10.2002 bei der Technischen Universität München eingereicht und durch die Fakultät für Physik am 09.12.2002 angenommen.



# Contents

<b>1</b>	<b>Introduction</b>	<b>1</b>
1.1	Gravitational wave astronomy . . . . .	1
1.2	Supernova physics . . . . .	3
1.2.1	Historical supernovae . . . . .	4
1.2.2	The classification of supernovae . . . . .	4
1.2.3	Core collapse supernovae . . . . .	6
1.2.4	Going further . . . . .	8
1.3	Simulations of gravitational collapse . . . . .	9
1.3.1	Newtonian simulations . . . . .	10
1.3.2	General relativistic simulations . . . . .	10
1.4	The characteristic formulation of numerical relativity . . . . .	11
1.5	A summary of the results presented in this thesis . . . . .	14
1.6	Organization of the thesis . . . . .	15
<b>2</b>	<b>Characteristic numerical relativity and hydrodynamics</b>	<b>17</b>
2.1	The Einstein equations for the Bondi metric . . . . .	18
2.2	The relativistic perfect fluid equations . . . . .	21
2.2.1	General relativistic hydrodynamics in axisymmetry . . . . .	21
2.2.2	Equations of state . . . . .	23
2.2.3	Equilibrium models for spherically symmetric stars . . . . .	25
2.3	Gravitational waves . . . . .	25
2.3.1	Gravitational waves at null infinity . . . . .	26
2.3.2	Approximate gravitational waves . . . . .	29
<b>3</b>	<b>The numerical implementation</b>	<b>33</b>
3.1	Implementation of the fluid equations: High-resolution shock-capturing methods	34
3.1.1	Reconstruction schemes . . . . .	35
3.1.2	Approximate Riemann solvers . . . . .	37
3.1.3	The recovery of the primitive variables . . . . .	39
3.2	Implementation of the metric equations . . . . .	41
3.2.1	Solving the wave equation . . . . .	41
3.2.2	Solving the hypersurface equations . . . . .	43
3.2.3	The Courant condition . . . . .	44
3.2.4	The origin treatment . . . . .	44
3.3	The fluid metric coupling . . . . .	45

3.4	Gravitational wave extraction . . . . .	45
3.4.1	Numerical extraction of the Bondi news . . . . .	45
3.4.2	Numerical extraction of approximate gravitational waves . . . . .	45
<b>4</b>	<b>Code tests</b>	<b>47</b>
4.1	Tests for the metric solver . . . . .	47
4.1.1	Linearized gravitational waves . . . . .	47
4.1.2	SIMPLE . . . . .	48
4.2	Tests concerning relativistic stars . . . . .	49
4.2.1	Equilibrium relativistic stars . . . . .	49
4.2.2	Global energy conservation . . . . .	52
4.3	Tests concerning supernova core collapse . . . . .	54
4.3.1	Shock reflection test . . . . .	54
4.3.2	Convergence tests . . . . .	55
<b>5</b>	<b>Relativistic stars interacting with scalar fields</b>	<b>59</b>
5.1	Mathematical framework . . . . .	60
5.1.1	Einstein equations . . . . .	60
5.1.2	Scalar field equations . . . . .	61
5.1.3	Hydrodynamic equations . . . . .	61
5.1.4	Global quantities . . . . .	62
5.2	Numerical implementation . . . . .	63
5.3	Code calibration . . . . .	64
5.3.1	Null cone evolution of stable stars . . . . .	64
5.3.2	Scalar field dynamics in a regular spacetime . . . . .	67
5.3.3	Global energy conservation . . . . .	67
5.4	Dynamics of scalar field - relativistic star interactions . . . . .	69
<b>6</b>	<b>Non-radial pulsations of relativistic stars</b>	<b>75</b>
6.1	The perturbations . . . . .	77
6.2	Fixed background evolutions . . . . .	78
6.3	Metric-fluid coupled evolutions . . . . .	81
6.4	Gravitational waveform . . . . .	84
<b>7</b>	<b>Simulation of supernova core collapse</b>	<b>87</b>
7.1	Initial models . . . . .	87
7.2	The dynamics of core collapse supernovae . . . . .	89
7.2.1	Collapse and bounce . . . . .	89
7.2.2	Fluid oscillations in the outer core . . . . .	95
7.3	Gravitational waves from core collapse supernovae . . . . .	96
7.3.1	Quadrupole gravitational waves . . . . .	96
7.3.2	The Bondi news signal . . . . .	101
7.4	Summary . . . . .	106
<b>8</b>	<b>Conclusion and outlook</b>	<b>109</b>

# Chapter 1

## Introduction

### 1.1 Gravitational wave astronomy

*We can propagate [gravitational waves] with the speed of thought.*  
Sir Arthur Eddington

In the early days of the theory of general relativity, the existence of gravitational waves was strongly under discussion. The debate focused on the problem whether gravitational waves are a consequence of general relativity or whether they are pure gauge effects (see e.g. [34]). Due to the nonlinear nature and the complexity of general relativity, it took almost 40 years to unambiguously show [18] that gravitational waves involve energy transfer and thus are a real prediction of the theory.

More than one decade later, R.A. Hulse and J.H. Taylor discovered the binary pulsar system PSR B1913+16 [73], on which further analysis revealed very convincing, but indirect evidence for the existence of gravitational waves [147, 156].<sup>1</sup> Newer measurements for the binary pulsar system PSR B1534+12 are also in agreement with general relativistic predictions [140].

Gravitational waves are weak fluctuations of the geometry of spacetime, which manifest themselves in small changes of the measured distances. The strongest gravitational waves are created by the aspherical movement of large masses, in particular by the variation of large (mass) quadrupole moments. As a consequence, astrophysical sources are the most promising sources of gravitational radiation. In contrast to electromagnetic waves, the amplitude of a gravitational wave decays linearly with the distance from the source. Optimistic estimates for astrophysical sources predict a relative length change on earth due to passing gravitational waves of the order of  $\delta L/L = 10^{-20}$ . In addition, gravitational waves only carry a tiny proportion of the source's energy away. As the effect of gravitational waves on earth is so weak, there are no successful direct measurements yet. However, the experimental effort for their detection has increased dramatically within the last years. Many different experiments around the world exist, which can be subdivided into resonant detectors and gravitational wave laser interferometers.

---

<sup>1</sup>They measured the change in the orbital period of the system as  $\dot{P}_b = (-2.403 \pm 0.002) \times 10^{-12}$ , in comparison to the value predicted due to emission of energy in gravitational waves using the quadrupole formula  $\dot{P}_b = (-2.40 \pm 0.09) \times 10^{-12}$ .

Resonant detectors were first implemented in the seminal experiment of Weber [154, 155]. They consist of bars of cryogenic<sup>2</sup> material (e.g. aluminium) with masses of several tons. Gravitational waves passing through the detector create mechanical resonances, i.e. oscillations of the mass which can be potentially measured. Currently, five resonant detectors, sensitive in the frequency range between 700 – 900 Hz, are in operation. These are [3] ALLEGRA (USA), AURIGA and NAUTILUS (Italy), EXPLORER (at CERN) and NIOBE (Australia). With sensitivities of up to  $10^{-19}$  localized in a small frequency window, current resonant detectors are at the threshold of what is generally believed to be necessary for successful detections. New spherical gravitational wave resonant detectors with improved sensitivity are planned.

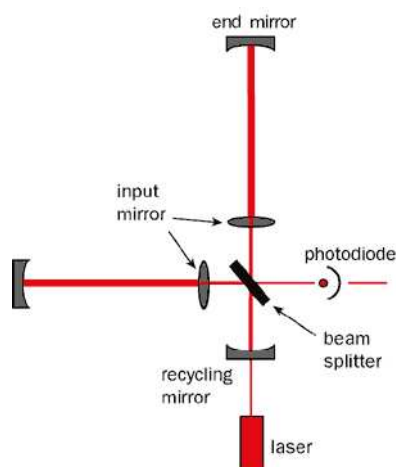


Figure 1.1: Sketch of a gravitational wave laser interferometer. The beam splitter separates the laser beam into orthogonal paths. The difference in the paths length can be measured as interference pattern at the photodiode. The input mirrors aim at increasing the effective arm length by forming Fabry-Perot cavities with the end mirrors. The recycling mirror enhances the laser power.

detectors are not sensitive because of gravity gradient noise at the earth's surface. There are already plans for third generation gravitational wave detectors (e.g. the European project EURO), which, due to an increased laser power and due to signal recycling aim to reach much higher sensitivities.

Independent of the type of detector, several experiments are needed to localize a burst of gravitational waves in the sky with the help of triangulation techniques. Once the capabilities to detect gravitational waves are developed enough, one could in principle localize a source and point optical telescopes towards the region of interest. Furthermore, gravitational wave astronomy will open in itself a new window in the sky beyond the electromagnetic spectrum.

In the following we will enumerate different astrophysical scenarios, which are believed to

<sup>2</sup>Strong cooling is necessary to lower the thermal noise as much as possible.

<sup>3</sup>Note, however, that with the use of Fabry-Perot cavities, the effective optical path length is much larger.

Gravitational wave laser interferometers (Michelson interferometers), on the other hand, are based on a completely different approach. They measure the length change due to passing gravitational waves in an interference pattern, which is created from a split laser beam running along orthogonal paths (Fig. 1.1, see also [72] and references therein for more details). Earth-bound detectors have typical arm lengths of several hundred meters.<sup>3</sup> Currently, the TAMA300 (Japan), the GEO600 (Germany, UK), the VIRGO (Italy, France) and LIGO (USA, two detectors) interferometers are in operation or will start operation later this year. One additional detector in Australia, AIGO, is under construction. After a first period of operation, LIGO will be updated to a second generation detector starting in 2005. Another experiment in space, LISA, will be launched in 2011, if the test mission SMART-2 (planned for 2006) is successful. With LISA, due to the extreme arm length of the detector,  $5 \times 10^6$  km (comparable to the distance earth - sun), the low frequency range between  $10^{-4}$  and  $10^{-1}$  Hz will be accessible, where ground-based gravitational wave



be important sources of gravitational waves to be detected with the current or next generation gravitational wave detectors, without going into the details of the current estimates (the evaluation of the efficiency of the different scenarios is still under discussion [66]).

- Coalescence of compact binaries

By a “compact binary” we mean a binary system consisting of compact objects, i.e. a neutron star (NS) or a black hole (BH). The coalescence of these objects is estimated to be the most promising source of gravitational waves to be detected with the current generation of gravitational wave laser interferometers. For recent, comprehensive studies, see [9, 80].

- Stellar core collapse

Non-spherical collapse of stellar configurations is believed to be a strong source of gravitational waves. However, because stellar collapse is not yet well understood there are still large uncertainties in the understanding of gravitational wave emission [72]. For a comprehensive overview, see [112, 50] - more details will be given in Sec. 1.3.

- Non-radial oscillations of neutron stars

In the absence of instabilities, gravitational waves from pulsating neutron stars are believed to be rather weak. Nevertheless, as there are many neutron stars in our galaxy a possible detection with the next generation gravitational wave detectors seems feasible [84]. Neutron stars exhibit a rich spectrum of oscillation modes, which depend on the radius and mass of the star, and hence on the equation of state (EoS) (see e.g. [83, 85]). The main goal in studies about oscillations of neutron stars (once it is possible to detect gravitational waves from them) is the determination of the EoS at supra-nuclear densities. The current estimates of the gravitational waves from oscillating neutron stars can be found in [84].

For the currently operating gravitational wave detectors it is of great importance to have a detailed knowledge of *wave forms* expected from astrophysical sources. This allows the use of *matched filtering* techniques to improve the sensitivity of the experiments enormously. Obtaining reliable estimates for gravitational wave signals emitted from the different sources is one of the key motivations for *numerical relativity*, where the partial differential equations of general relativity are solved with the help of computers. Except for the black hole binary system, all mentioned sources of gravitational waves involve matter, which makes necessary to solve the hydrodynamic equations as well.

## 1.2 Supernova physics

Supernovae [4] are very violent cosmic explosions of stars, which are related to a sudden and intense increase of the measured luminosity of the object, which in general outshines the rest of the whole host galaxy for several days. Supernovae are not only very promising sources of gravitational waves, but are also very important phenomena of astrophysics as a whole. In a supernova explosion, large amounts of matter, including heavy elements, are transferred to the interstellar medium, which is important for the formation of stars. Moreover, supernovae produce galactic winds, and a substantial contribution of cosmic rays is created in these explosions.

### 1.2.1 Historical supernovae

Only a few supernova explosions have been doubtlessly observed in our own galaxy within the last 1000 years [93, 26]. The earliest one of those was the supernova explosion of the year 1006, which is recorded in Arabic, Japanese and Chinese sources [109]. A further record of a supernova explosion in the Milky Way dates back to the year 1054, when Chinese and Japanese astronomers discovered a new luminous object which left behind today's famous Crab nebula, a supernova remnant with a faint neutron star in its center. More than 300 years later, two of the most prominent astronomers of the Renaissance period, the Danish astronomer Tycho Brahe and Johannes Kepler, each observed a supernova explosion. In 1572, Tycho Brahe observed a "new star" in the constellation of Cassiopeia, and in 1604, Johannes Kepler observed another supernova in the constellation of Ophiuchus. Unfortunately, since the invention of the telescope shortly afterwards, which was first used in 1609 by Galileo, no further supernova event has been recorded in the Milky Way.<sup>4</sup> The first supernova explosion beyond our own galaxy was discovered in 1885 by E. Hartwig and independently by L. Gully in the Andromeda galaxy. At that time it was not yet known that Andromeda is an independent galaxy. In 1933, Walter Baade and Fritz Zwicky concluded (see [109]) that due to the large distances of supernovae explosions, the total radiated energy in supernovae must be of the order of  $10^{51}$  to  $10^{53}$  erg (which corresponds to about  $5 \times 10^{-4}$  to  $5 \times 10^{-2}$  times the rest mass energy of the sun). A very important step forward in the understanding of supernova explosions came in 1987. On 2/23/1987 a supernova explosion was discovered in the Large Magellanic Cloud (about 170 000 light years away). Supernova 1987A was not only the most luminous one since the supernova event in 1604, it also was possible for the first time to identify a progenitor star related to the explosion, the blue supergiant *Sanduleak -69 202* with an estimated mass of about  $18M_{\odot}$ . Moreover, a hail of neutrinos from this event arrived on earth. About two dozen of these neutrinos were detected independently by three different neutrino experiments.

### 1.2.2 The classification of supernovae

Historically [102], supernovae were subdivided into two classes, supernovae I and supernovae II (henceforth SN I and SN II). Whereas SN II display hydrogen Balmer absorption lines in their spectrum, these lines are absent for SN I. Both classes can be further subdivided according to their spectra and light curves: SN I are subdivided into SN Ia, SN Ib and SN Ic, according to the presence of the absorption lines for He  $\lambda$  5876 Å and for Si  $\lambda$  6355 Å. In the spectrum of SN Ia, both absorption lines are present. In contrast, SN Ib only show the He  $\lambda$  5876 Å absorption line. Finally, both lines are absent for a SN Ic. Type II supernovae are further classified as SN II-L and SN II-P, according to the presence of a linear decay in the light curves or a specific plateau. Fig. 1.2 shows the typical spectra and Fig. 1.3 the typical light curves of the different types of supernovae. A comprehensive treatment of light curves from supernovae can be found in [37].

This historical classification based on observations is not reflected in our current understanding of the energy source and the progenitors (see [107]). When classifying supernovae according to the energy source, the main division line lies between SN Ia and the other types. Observationally, SN Ia occur in all types of galaxies, and in particular in elliptical galaxies where the proportion of old stars is high. This observation strongly suggests that the progenitors of SN Ia

<sup>4</sup>However, there is indirect evidence from recent observations of the supernova remnant Cas A which suggests that Cas A exploded in the late 17th century, probably in 1680.

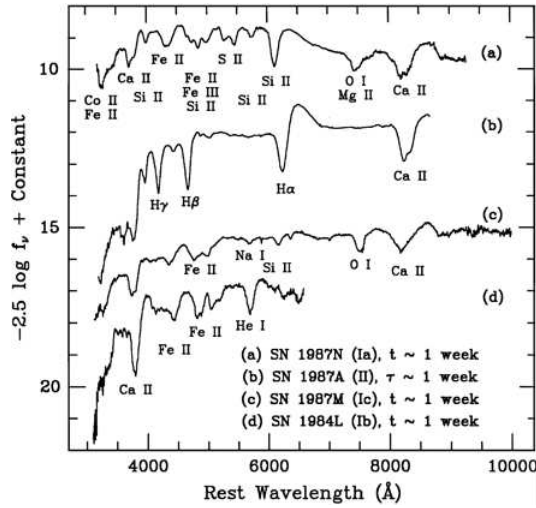


Figure 1.2: Typical spectra of the different types of supernovae averaged over the the first week after maximum (taken from Filippenko. [37]).

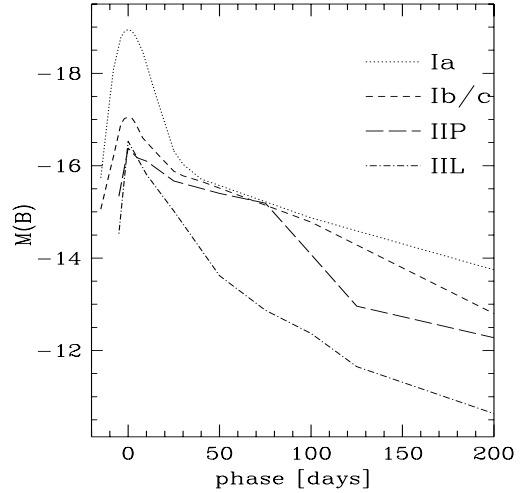


Figure 1.3: Typical lightcurves of the different types of supernovae. Plotted is the absolute magnitude  $M$  in the blue frequency band (B band) as a function of time in days (taken from Cappellaro et al. [24]).

are old stars. According to the favorite models the progenitors are carbon-oxygen white dwarfs in a binary system. The companion star, which has lost its hydrogen envelope to the white dwarf, further transfers mass to the white dwarf, until the latter reaches the Chandrasekhar mass, i.e. the maximum mass of a white dwarf for which the pressure exerted by the relativistic gas of degenerate electrons exactly balances the gravitational force. Close to the Chandrasekhar mass limit, the mass transfer from the companion can ignite a thermonuclear explosion. The light curves of SN Ia are powered by the decay of  $^{56}\text{Ni}$  (synthesized during the explosion) into  $^{56}\text{Co}$  and finally into  $^{56}\text{Fe}$ . The  $\gamma$ -rays created in the decay are Compton scattered (i.e. scattered by electrons), which finally creates the observed light curves and spectra. The total energy released during the explosion is of the order of  $10^{51}$  erg. For the other types of supernovae the favorite model prescribes the observed energies to the release of gravitational binding energy in a gravitational collapse. Host galaxies of SN II, SN Ib and SN Ic are spiral galaxies, where they occur in the spiral arms with a large number of hydrogen-rich, young massive stars. Hence, there is strong evidence that the progenitors are massive young stars. SN Ib/Ic progenitors may have lost their hydrogen or even part of the helium envelope by either stellar wind (Wolf-Rayet stars with masses  $M \geq 30M_{\odot}$ ) or due the mass transfer to a close companion. Stellar evolution models show that SN II progenitors must have masses  $M \geq 9M_{\odot}$  in order to produce sufficiently high temperatures to form a central iron core through several stages of nuclear burning. The iron core finally undergoes a gravitational collapse. The progenitors of SN II-L and SN II-P probably differ in the amount of mass of their hydrogen envelope, but are caused by the same explosion mechanism. As already mentioned, the rate of supernovae depends on the type of

the host galaxy. For our own galaxy, one expects [24] on average about 0.4 SN Ia events, 0.2 SN Ib/c events and 1 SN II event per century.

### 1.2.3 Core collapse supernovae

After having gone through successive nuclear burning stages, during which heavy elements have been synthesized, stars with a mass of  $M \geq 9M_{\odot}$  have developed an onion-like shell structure with an *iron core* in the central region (see Fig. 1.4). This iron core consists of elements of the



Figure 1.4: Onion-like shell structure of a type II supernova progenitor. The diagram shows the inner structure of a  $25M_{\odot}$  evolved star. Due to successive nuclear burning stages, shells of hydrogen, helium, carbon, oxygen and silicon have formed. The iron core in the central region has a radius of about 1500 km. The figure was taken from [110].

iron group (Fe, Ni and Co, i.e. those elements with the largest binding energy per nucleon). The iron core can be further characterized by a central density of about  $\rho_c = 10^{10} \text{ g cm}^{-3}$ , a temperature of  $T = 10^{10}\text{K}$ , and an average number density of electrons per baryon of  $Y_e = 0.46$ . For these densities and temperatures, the pressure is mainly generated by the degenerate relativistic electron gas. The electron pressure is much more important than the pressure due to the ions and the radiation pressure,  $p_e \gg p_{ion} \gg p_{rad}$ . Hence the microphysics of the iron core can be modeled well by a polytropic relation  $p = \kappa\rho^{\Gamma}$  with adiabatic exponent  $\Gamma = \frac{4}{3}$  (see [133]). For such a configuration, the Chandrasekhar mass limit is to first order  $M_{Ch} \approx 5.83 Y_e^2 M_{\odot}$ . This formula was derived under simplified assumptions. Corrections taking into account the finite temperature, the Coulomb repulsion of the nuclei, surface effects (the outer boundary of the iron core does not have zero density), as well as general relativity are necessary. Above the Chandrasekhar mass limit, the degenerate electron pressure cannot counterbalance gravity any longer, and the iron core undergoes catastrophic collapse. This can either happen as a consequence of further Si burning, which increases the mass of the iron core,

or due to electron capture by iron group elements (this occurs due to the high densities, and hence high electron Fermi energies), which diminishes the value of  $Y_e$ . For the densities of the iron core in the initial phase of the collapse, the neutrinos produced by electron captures can leave the core without further interaction. Another process, which can lead to the onset of the gravitational instability is the photodisintegration of iron group elements as a consequence of the interaction with energetic thermal  $\gamma$ -radiation. However, photodisintegration is only important for very massive progenitors.

At the onset of the gravitational instability, the trajectories of mass shells in the iron core are well modeled by the effective adiabatic index

$$\Gamma_1 = \frac{\partial \ln p}{\partial \ln \rho} = \Gamma + \frac{4}{3} \frac{1}{Y_e} \frac{\partial Y_e}{\partial \ln \rho} < \Gamma, \quad (1.1)$$

with a typical value of  $\Gamma_1 = 1.3$ . The collapse phase only lasts for several 10 ms. As a consequence, the outer stellar burning shells have no time to react to the collapse of the central region, and the collapse of the iron core can be modeled independently. In the collapse phase, any viscosity and heat transport can be neglected. It is therefore possible to model the collapsing material as an ideal fluid. Furthermore, the evolution is close to adiabatic. Approximately, the core can be divided into two regions: The inner part of the infalling material can be described by a homologous (self-similar) solution [54, 165], where the infall velocity as a function of the radius  $r$  is proportional to the radius  $r$ . This region is called the *inner core*. The outer part of the fluid consists of supersonically infalling material and makes up the *outer core*. These two regions are separated by the *sonic point*, where the amplitude of the infall velocity equals the local speed of sound. At the sonic point, maximum infall velocities of up to  $0.2c$  are reached. For non-rotating models, the collapse can be only stopped when the central density reaches nuclear matter density,  $\rho_n \approx 2 \times 10^{14} \text{ g cm}^{-3}$ . At that density, nuclear repulsive forces between protons and neutrons become important. Finally, the pressure of degenerate nucleons can counterbalance gravity. Since the extreme conditions encountered in this phase can not be reproduced in laboratory experiments, it is not surprising that the EoS is highly uncertain [71, 5]. Approximately, it can be modeled by an effective adiabatic index  $\Gamma_2 = 2 \dots 3$ . On a maximum timescale of only a few milliseconds, the infall of inner core is stopped. Sound waves traveling through the inner core focus at the sonic point, which is located at a radius including a mass of about  $0.5M_\odot$  at that time. A shock wave is created, which travels out with speeds of about  $0.1c$ . Interior to the sonic point, a neutron star forms. Assuming a mass  $M$  and a radius  $R$  of the neutron star, the gravitational binding energy

$$E \approx 3 \times 10^{53} \left( \frac{M}{M_\odot} \right) \left( \frac{R}{10 \text{ km}} \right)^{-1} \text{ erg}, \quad (1.2)$$

is released. Most of this energy is stored in a sea of neutrinos and is radiated away after a time of about 1 s. The neutron star cools down, due to this emission of neutrinos. Analytic arguments show [166] that the shock initially has an energy of about  $5 \times 10^{51} \text{ erg}$ . This is in principle sufficient energy to unbind the outer layers of the star and to produce a supernova explosion. However, as the shock travels out, it loses a large amount of its energy, mainly due to photodisintegration of iron into free nucleons. As a consequence, the shock stalls.

Despite intensive efforts to understand the supernova core collapse explosion mechanism, many important questions have not been solved yet. Neutrinos can in principle deposit enough energy behind the shock to explode the outer layers of the collapsing star (this is the so-called

*delayed explosion mechanism*, see [157, 10]). However, the delayed explosion mechanism is only a relevant mechanism under very specific assumptions. Recent work tries to model neutrino transport consistently and to include general relativistic aspects. For more details, the reader should refer to [77].

Observations during the last decade have found strong evidence that neutron stars receive large kick velocities (of a few hundreds to a thousand km/s) at birth. The origin of these large kick velocities is still unclear. Possible explanations range from hydrodynamically driven asymmetries [22] over neutrinos to asymmetries in the radiated electromagnetic fields (for a recent review see [86]).

### 1.2.4 Going further

As the end product of a core collapse and supernova explosion, a strongly pulsating neutron star (a so-called *proto-neutron star*) will be created. Protoneutron stars are hot and lepton rich objects. The predominant cooling mechanism immediately after formation is neutrino emission, by which they transform to ordinary neutron stars over a timescale of several seconds. Until today, the inner structure of neutron stars, i.e. the EoS under the extreme condition of highly condense matter, is only very poorly known. As a consequence, there is a variety of competing theories of the inner structure of neutron stars. Although the models' predictions vary substantially, present observations are far from being decisive concerning the correctness of the different theories.

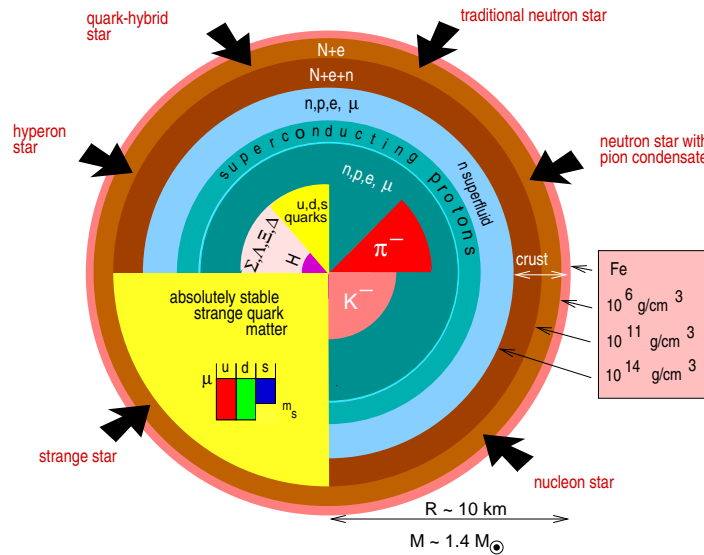


Figure 1.5: Inner structure of a neutron star for different models of the EoS. The typical radius of a neutron star is  $R \approx 10\text{km}$ , the typical mass  $M \approx 1.4M_{\odot}$ . The diagram was taken from [153].

In Fig. 1.5, several different scenarios are visualized. All the scenarios model the outer layers of the star by a crust. In the traditional picture of neutron stars, the interior region consists of neutrons, protons and electrons, which are surrounded by a shell of superfluid neutrons (see e.g. [133]). Alternatively, a high density EoS with pion condensation has been proposed [100,

132]. The possibility of kaon condensation was discussed [19], which would give rise to a nucleon star. Finally, many authors have examined the possibility of stars composed of strange quark matter, either in the form of stable quarks, or bound in hyperons, or as a mixture of hadrons and quarks.

Since neutron stars are very compact (masses of more than a solar mass are compressed inside a radius of about 10 km) and have a cold surface, they cannot be observed at large distances in the electromagnetic spectrum. Moreover, the radiation emitted in X-rays stems from the stellar surface. The natural candidate (besides neutrinos in the early stage of the neutron star formation [23]) for obtaining insight into the internal structure of neutron stars are gravitational waves. As in the case of *helioseismology*, the study of oscillations of the sun, *astroseismology* could result in detailed measurements of the interior structure of neutron stars, which would allow to decide between the different models for their inner structure.

*Gamma Ray Bursts* (GRB), which were first detected in the late 1960s by military satellites, are even more violent processes than supernovae. The observed GRB fluxes imply energy emission in  $\gamma$ -rays of up to  $10^{52}$  erg (assuming isotropic emission, the value would be even higher), liberated in a region of the size  $\lesssim 100$  km (for recent reviews, see [98, 99]). The most prominent candidates for such an energy outburst are the coalescence of a binary neutron star system or a neutron star - black hole system, and two scenarios directly linked to gravitational collapse. These are the *collapsar/hypernova* model proposed by Woosley [164, 94] and Paczinsky [114] and the *supranova* model proposed by Vietri and Stella [151]. Whereas the collapsar/hypernova model proposes a “failed” supernova as the energy source for a GRB (i.e., either the direct or delayed collapse of an evolved star to a black hole), the supranova model explains the observed energies by the collapse of a rotating, overcritically massive neutron star, which cools down or loses angular momentum due to the radiation of electromagnetic waves and gravitational waves, and finally becomes unstable. Hence, gravitational collapse may be also very important for the understanding of GRB. For recent observational indications of the link between GRB and SN see [15].

Independent of whether gravitational collapse is the energy source of a GRB, other gravitational collapse scenarios than supernova core collapse are expected to exist in nature. For the theory of general relativity and for gravitational wave astronomy, the gravitational collapse to black holes is particularly interesting (see [112]). For example, the accretion induced collapse of neutron stars, the collapse of population III stars (first generation stars) and the collapse of supermassive stars could all lead the formation of black holes.

### 1.3 Simulations of gravitational collapse

There exists a large number of numerical simulations concerning gravitational collapse, and in particular core collapse supernovae in the literature. An adequate physical description of core collapse supernovae is very demanding, and would have to include a large amount of input from different branches of physics, e.g. multidimensional hydrodynamics, nuclear physics (in particular neutrino physics) and plasma physics, detailed models of nuclear burning, radiation transport and last but not least, general relativity. In general, due to the complexity of the problem, the simulations only focus on particular aspects. Here, we subdivide the simulations according to whether they were performed in Newtonian physics or in general relativity.

### 1.3.1 Newtonian simulations

The physics of supernova core collapse has been studied quite extensively in Newtonian physics. For example, axisymmetric rotational core collapse (neglecting neutrino transport) was studied by Müller and Hillebrandt [108], by Bodenheimer and Woosley [16], by Symbalisty [145] and by Bonazzola and Marck [17]. Several investigations, including those of Mönchmeyer and Müller [104], Janka and Mönchmeyer [78], Mönchmeyer et al. [105], Imshennik and Nadezhin [74], Fryer and Heger [49] and Fryer et al. [50] treated neutrino transport approximatively. Without including neutrino physics or a detailed description of the microphysics, Yamada and Sato [167] performed systematic numerical simulations of core collapse supernovae. Finn and Evans [39] focussed on different numerical methods for the gravitational wave extraction based on the quadrupole approximation. Zwerger and Müller [169] performed parameter studies of core collapse supernovae and extracted the (quadrupole) gravitational wave signal for a comprehensive sample of models. As summarized in [106], the typical gravitational wave amplitudes of the simulated supernova events are in the range which could be detected by the first generation gravitational wave laser interferometers, provided the supernova explosion takes place in our galaxy. Rampp et al. [127] and Brown [20] first studied the problem beyond axisymmetry. Whereas all these simulations focused on the dynamics of the core collapse and bounce, a few other simulations examined the later phase of the explosion (e.g. Kifonidis et al. [81]).

### 1.3.2 General relativistic simulations

Numerical simulations in general relativity were performed already in the early days of computers. The seminal work on relativistic collapse was performed by May and White [97].<sup>5</sup> The field equations of general relativity are a highly complicated and nonlinear set of partial differential equations. Due to their complexity early numerical relativity codes could not be applied to studies of astrophysical interest, except in spherically symmetric situations. In contrast to a Newtonian approximation where the computational problem is well defined and attention can be devoted to astrophysical details, there is no consensus as to what is the optimal, or at least adequate, framework for developing relativistic simulations. The numerical relativist must overcome a daunting list of problems, including the long term stable formulation of the initial value problem and the reliable extraction of physical information (including gravitational waveforms).

Apart from a series of spherically symmetric studies following the early work of May and White, which were all based on Cauchy slicings (see Romero et al. [128] for more details), there is a small number of investigations, e.g. the work of Miller and Motta [101], which used a null slicing of spacetime to calculate gravitational collapse (see the next section for an explanation of the different slicings). With an approach based on null slices Baumgarte et al. studied supernova collapse [7] and the collapse of neutron stars to black holes [8]. Recently, Linke et al. [92] analyzed the spherical collapse of supermassive stars.

Going from spherical symmetry to 2D or 3D simulations, the complexity of the general relativistic field equations increases substantially. This can already be understood from the fact, that there are no gravitational waves in a spherically symmetric spacetime. Early approaches did not only have to face problems of limited computer power, but also the problems of numerical instabilities arising from the formulation of the Einstein equations. Nakamura [111] and Stark and Piran [141, 142] studied the formation of a black hole as the end product of the collapse

<sup>5</sup>The authors refer to “digital” computers, which seems to be redundant from our today’s point of view.



of a rotating massive star. Evans [36] developed an axisymmetric relativistic code, but only applied it to spherical simulations of stellar core collapse. In total, only a few multidimensional simulations of general relativistic gravitational collapse exist today which are of astrophysical interest. Recent studies by Dimmelmeier et al. [30, 31, 32] of axisymmetric rotational core collapse rely on an approximation of general relativity, the so-called conformally flat metric approach [158], in which the gravitational wave degrees of freedom are suppressed. Although the dynamics and the gravitational wave signal are very different in these simulations in comparison to the Newtonian results of [169] for particular models, the overall estimates for the gravitational wave amplitudes are unchanged. There are simulations of axisymmetric rotating stellar collapse to black holes in full general relativity by Shibata [134]. Moreover, Shibata et al. [136] studied rotational collapse of neutron stars to black holes without imposing any symmetry. However, apart from a very recent study by Shibata [135] where no gravitational waves were analyzed, until now, there are no studies of supernova core collapse beyond spherical symmetry in full general relativity, which would be needed to obtain reliable estimates of the gravitational wave signals for this process.

## 1.4 The characteristic formulation of numerical relativity

General relativity is a covariant theory, mathematically formulated as a set of tensor equations. For numerical solutions of the field equations, however, a coordinate system has to be chosen, i.e. one has to formulate the equations as an initial value problem. Interestingly, depending on the choice of coordinates and depending on the choice of metric variables, the mathematical character of the field equations can change.

Starting with a vector field of four dimensional spacetime, spacetime is foliated (i.e. sliced) into a family of hypersurfaces orthogonal to the vector field. Choosing this vector field to be timelike<sup>6</sup> the approach is called *3+1 formalism* or *Cauchy approach*. Of course, for a given spacetime, there is an infinite possible choice of timelike vector fields corresponding to different foliations. In the Cauchy approach, the streamlines of the vector field can be used to define a (time) coordinate to label the different spacelike hypersurfaces. On the other hand, choosing a null vector field as normal to the hypersurfaces defines the *characteristic approach* or *null cone approach* of numerical relativity [163]. Fig. 1.6 visualizes the definition of Cauchy slices and null slices. In the case of null slices, the streamlines of the vector field are tangential to the surface itself (a null vector is orthogonal to itself)<sup>7</sup> and hence they cannot serve to label different hypersurfaces. There are different characteristic initial value formulations, where the difference arises from the choice of coordinates on the hypersurfaces and the coordinates to label the null hypersurfaces. The approach followed in this thesis is based on the characteristic initial value problem of Bondi et al. [18] and Sachs [131] and, in particular, on the worldtube-nullcone formalism of Tamburino and Winicour [146]. The formalism has been developed specifically for addressing ambiguities concerning gravitational radiation and is well adapted to handle the propagation of signals.

As pointed out in the last section there are a few numerical simulations of gravitational collapse in spherical symmetry based on the foliation of spacetime by light cones, i.e. based

---

<sup>6</sup>We chose the signature of the spacetime metric  $g_{ab}$  in such a way, that a vector  $v^a$  is timelike, if  $g_{ab}v^av^b < 0$ , and spacelike, if  $g_{ab}v^av^b > 0$ . For  $g_{ab}v^av^b = 0$ ,  $v^a$  is a null vector.

<sup>7</sup>In an vector space  $V$  with indefinite scalar product, the orthogonal complement  $W^\perp$  of a subspace  $W$  in general does not fulfill  $W^\perp + W = V$ , although  $\dim(W) + \dim(W^\perp) = \dim(V)$ .

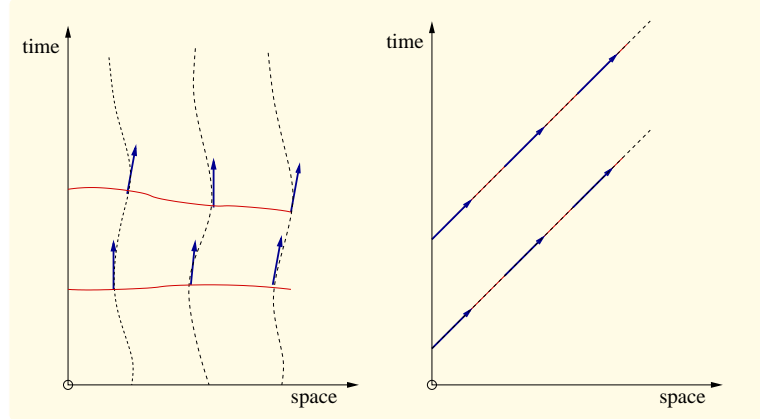


Figure 1.6: Definition of Cauchy slices (left) and characteristic slices (right). We have plotted a spacetime diagram, where null lines are represented by curves of  $45^\circ$  and where we have suppressed two spacelike coordinates. The slices are shown in red, with normal vectors indicated by the blue arrows. These normals are timelike and null respectively.

on null slices. So far, however, no multidimensional numerical simulations of stellar dynamics exist in this approach. At the same time, there is a lot of experience on numerically solving the field equations of general relativity on light cones beyond spherical symmetry in vacuum [163].

Before we can point out the advantages of the characteristic approach, some aspects of the Cauchy approach have to be described. In order to obtain initial data on an initial hypersurface, a set of nonlinear elliptic equations has to be solved, the so-called *constraint equations*. These constraint equations determine the geometry and the extrinsic curvature on the initial surface, i.e. the first and second fundamental forms. An additional set of equations, the so-called *evolution equations* determines the time evolution of the internal geometry and the extrinsic curvature from one hypersurface to the next. Making use of the freedom of choosing variables for the evolution equations, it is possible to write them as a system of symmetric hyperbolic equations [47, 48], for which local existence and uniqueness theorems apply. As numerical experience has shown, this alone is not enough to obtain stable algorithms for their numerical solution. Further numerical complications arise from the fact that the numerical evolution will violate the constraint equations (although, fulfilled exactly on the initial slice, they should be fulfilled forever) and from the boundary treatment of the numerical domain.

The characteristic approach has a number of advantages compared to the Cauchy approach:

- It is physically motivated; the light cones offer a simple and unambiguous physical gauge on which to base the numerical spacetime grid.
- It is unconstrained; the evolved variables capture rather directly the true degrees of freedom of the gravitational field. No elliptic equations have to be solved to determine consistent initial data.
- It is very efficient; even in 3D, there are but two partial differential equations to solve, along with a set of radial integrations along the light cones. No second time derivatives appear in the equations.

- It allows for a well defined compactification [123] of the domain, by which the global spacetime extending to infinity is mapped onto a finite region. For example, Minkowski spacetime with metric  $\eta_{ab}$  can be mapped onto a finite region of the so-called Einstein static universe with metric  $\tilde{\eta}_{ab}$  using a conformal transformation,  $\tilde{\eta}_{ab} = \Omega^2 \eta_{ab}$ . The boundary of the finite region of the Einstein static universe corresponds to infinity in the Minkowski spacetime. In particular, it is possible to define future null infinity, where all null geodesics end. Similar compactification techniques can be applied for a general class of spacetimes describing isolated astrophysical systems, the so-called *asymptotically flat* spacetimes. For more details concerning the Penrose compactification and the mathematical definition of asymptotical flatness, the reader is referred to the textbook [152]. Covering the finite region with a numerical grid leads to perfect outer boundary conditions. In addition, gravitational waves can be extracted without approximation. Since each null hypersurface of the foliation extends to infinity in the physical spacetime, the gravitational radiation can be calculated immediately with no need to resolve the wave forms propagating across the grid.
- Finally, and perhaps most importantly, the above theoretical advantages have been shown in a series of works to translate to remarkably robust and stable numerical codes (see e.g. [58]).

For a recent review of the approach the reader is referred to [163].

All characteristic schemes have as a common disadvantage the necessity either to deal with light caustics or to avoid them altogether. In the presence of caustics, i.e. when different light rays emanating from a point in space refocus, it is not possible to foliate a spacetime with the help of null surfaces without forming coordinate singularities. There have been attempts to include the evolution of caustics into the characteristic approach [28, 144], but in general, to avoid complications, one has tried to eliminate them. Therefore, for the very strong field regime of general relativity, e.g. the merger of binary black holes, it is believed to be simpler to use the 3+1 formalism in the region where caustics may occur and to match this region to an exterior characteristic grid for the gravitational wave extraction. This approach is called Cauchy-characteristic matching (CCM). Until today, CCM has been demonstrated to work reliably in spherical symmetry [57] and for the 3D scalar field equation in Minkowski space [13].

In the characteristic approach, to obtain a complete *regular* spacetime (in contrast to a black hole spacetime where singularities occur), the computational domain must include the vertex of the light cones. This involves prescribing specific regularity conditions at the vertex of the light cones (and for explicit integration methods, severe time-step restrictions), which at present have been resolved only up to axisymmetric configurations [60]. Nevertheless, the approach has remarkable economy and stability, which makes it a good candidate for studies of isolated relativistic objects emitting gravitational radiation. This is the principal motivation for the current work.

The results presented in this thesis show that for a wide and astrophysically interesting class of spacetimes it is sufficient to use the characteristic initial value formulation of the Einstein equations without matching it to a Cauchy region. In particular the study of the nonlinear dynamics of isolated relativistic stars and supernova core collapse is optimally performed within this framework.

The incorporation of perfect fluid matter fields in the characteristic formulation of the Einstein equation was first considered by Isaacson et al. [75] as early as 1983 but the successful

integration of the coupled system had to wait for the development of stable algorithms for the *vacuum* Einstein problem. Gomez et al. developed one dimensional schemes in [64]. Algorithms for axisymmetric spacetimes, including a regular origin, were presented in [60]. Recently, using similar techniques, Papadopoulos [116] evolved axisymmetric vacuum black hole spacetimes. Techniques for extending finite difference algorithms to 3D were presented in [59]. Three dimensional codes excluding the origin of the light cones (hence presently unsuitable for studies of stellar dynamics) were presented in [11, 56]. For an alternative approach see Bartnik and Norton [6].

With reliable algorithms for the vacuum Einstein equations available, Papadopoulos and Font [118] initiated a new line of research for the incorporation of relativistic hydrodynamics into characteristic numerical relativity. This approach carries over the modern machinery from Computational Fluid Mechanics to general relativistic hydrodynamics on light cones. In this procedure, the evolution equations for the matter fields are solved using relativistic high-resolution shock-capturing (HRSC) schemes [40, 119] based upon (exact or approximate) Riemann solvers. A general formalism has been developed. First applications in spherical symmetry have already been presented in the literature: investigations of accreting dynamic black holes can be found in [118, 120]. Studies of the gravitational collapse of supermassive stars are discussed by Linke et al. [91]. We note that there has been already a proof-of-principle demonstration of the inclusion of matter fields in three dimensions by Bishop et al. [12].

## 1.5 A summary of the results presented in this thesis

We have written a new numerical code which solves the coupled Einstein-perfect fluid system in axisymmetry [138]. Our approach relies on the Bondi metric, which uses a foliation based on a family of light cones, emanating from a regular center, and terminating at future null infinity. In our geometric setup we solve the nonlinear equations of general relativity in axisymmetry and the nonlinear equations of general relativistic fluid dynamics for the case of a perfect fluid. Our coordinate system is well adapted to the study of dynamical spacetimes associated with isolated relativistic compact objects such as neutron stars. In particular, the approach allows the unambiguous extraction of gravitational waves at future null infinity and avoids spurious outer boundary reflections.

In order to solve the Einstein equations, we rely on the experience of solving the characteristic field equations in vacuum [163]. Using a compactified spacetime where future null infinity is part of our numerical grid, we solve the partial differential equations of the Einstein-perfect-fluid system to determine the geometry of spacetime. We extract global quantities as the Bondi mass, the total mass of spacetime, and gravitational wave signals at future null infinity without approximation. For the fluid evolution, we use general relativistic high-resolution shock-capturing schemes [40]. Despite of being standard techniques in computational fluid dynamics and being widely used in astrophysical simulations with Newton's law of gravity, we have for the first time applied the techniques to multidimensional fluid evolutions in the characteristic approach of general relativity.

We have thoroughly tested our implementation. Unlike previous numerical relativity codes, our code is long-term stable. It can accurately maintain long-term stability of polytropic equilibrium models of neutron stars. We have demonstrated global energy conservation in a strongly perturbed neutron star spacetime, for which the total energy radiated away by gravitational waves corresponds to a significant fraction of the Bondi mass. Moreover, the code can handle

strong shock fronts moving at ultrarelativistic speeds, which are commonly encountered in astrophysical situations involving large velocities and strong gravitational fields (neutron stars and black holes). We have applied our code to three different topics:

- First, we study the interaction of massless scalar fields with neutron stars by means of numerical simulations of the Einstein-Klein-Gordon perfect fluid system in spherical symmetry [139]. The massless scalar field serves as a simple model for gravitational waves in spherical symmetry, by which many of the concepts of the later multidimensional analysis become relevant. We analyze the nonlinear dynamics of scalar fields scattered off neutron stars with different masses and radii. Depending on the compactness of the stellar model, the scalar wave forces the star either to oscillate in its radial modes of pulsation or even triggers the gravitational collapse to a black hole. We study the transfer of energy from the scalar field to the fluid star. It increases with the compactness of the star, inducing linear or nonlinear oscillations and even the gravitational collapse for the most compact models. The radiative signal, read off at future null infinity, shows quasi-normal oscillations before the setting of a late time power-law tail.
- The second analysis focuses on axisymmetric pulsations of neutron stars [138]. We extract the frequencies of the different fluid modes in fully relativistic evolutions of the Einstein-perfect fluid system. In cases where we can compare our results with independent results based on perturbation theory, we find very good agreement for the frequencies of the different fluid modes. As expected, the gravitational waves from quadrupolar oscillations show the largest amplitude. We also perform a comparison between the gravitational news function, i.e. the exact gravitational wave signal extracted at future null infinity, and the predicted wave using the approximation of the quadrupole formula. Finding good agreement between the two we conclude that the quadrupole radiation formula is a valid approximation for the study of gravitational waves from (weak) pulsations of neutron stars.
- In a third analysis, we study axisymmetric supernova core collapse in full general relativity. The nonlinear dynamics of the collapse is analyzed for a sample of models which differ on the particular parameterized deviation imposed in the equilibrium models of the initial “iron core”. Modeling the iron core by a relativistic polytrope, we follow the increase of the central density by more than four orders of magnitude, where the iron core bounces due to nuclear forces. We study the formation of the neutron star in the central region and the propagation of the outwards traveling shock. Moreover, we analyze the gravitational wave signals obtained from the parametrized collapse models. For these simulations, the validity of the quadrupole approximation breaks down. There are strong indications that this is a consequence of our particular coordinate system, in which we calculate the quadrupole moment of the simulated matter distribution. We extract the Bondi news function for the collapse models, finding a typical principal frequency for the gravitational wave signals of the order of 0.3 kHz to 1 kHz.

## 1.6 Organization of the thesis

We have structured the thesis as follows: In Chapter 2 we summarize the mathematical framework of the characteristic formulation of general relativity. Sec. 2.1 describes the field equations

of general relativity on the light cone. In Sec. 2.2 we discuss the equations of general relativistic fluid dynamics. Finally, Sec. 2.3 deals with the compactification of spacetime and the extraction of gravitational waves in the characteristic approach. Chapter 3 describes the numerical implementation of the Einstein-perfect fluid system. In Sec. 3.1, we describe the high-resolution shock-capturing schemes to solve the fluid equations. We discuss the different reconstruction schemes and approximate Riemann solvers implemented for the fluid update. Sec. 3.2 describes the numerical algorithms, which solve the characteristic Einstein equations. We discuss the numerical methods used for the coupling of the metric and fluid equations (Sec. 3.3) and the extraction of gravitational waves (Sec. 3.4). Chapter 4 describes the comprehensive tests, we have performed to validate the different regimes of our code. These tests assess both the implementation of the Einstein equations alone (Sec. 4.1) and the fully coupled Einstein-perfect fluid system (Sec. 4.2 and Sec. 4.3). In the next three chapters, we describe the results obtained with our code when applying it to the different scenarios already mentioned: Chapter 5 summarizes our findings for the study of the interaction of neutron stars and scalar fields. Since we have included in this chapter a scalar field as an additional matter field, we describe the necessary mathematical foundations and numerical implementations first. Sec. 5.4 describes the outcome of the numerical simulations. In Chapter 6 we present our results on the oscillations of neutron stars. In order to excite the different fluid modes we use the fluid perturbations described in Sec. 6.1. Before solving the full set of equations of the Einstein-perfect fluid system described in Sec. 6.3, we perform nonlinear hydrodynamic simulations in a fixed background (see Sec. 6.2). We discuss the gravitational wave signal from the full simulations in Sec. 6.4. Chapter 7 describes the studies of supernova core collapse. In Sec. 7.1 we introduce the models we use as initial data for our simulations of supernova core collapse. We describe the dynamics of the collapse as extracted from our numerical simulations in Sec. 7.2. Finally, the gravitational wave signals from supernova core collapse are presented in Sec. 7.3. The results of the thesis are briefly summarized in Chapter 8.

## Chapter 2

# Characteristic numerical relativity and hydrodynamics

In the field equations of general relativity, the geometry of spacetime, i.e. the Einstein tensor  $G_{ab}$  is related to the stress energy tensor  $T_{ab}$  of matter. For a given stress energy tensor, the Einstein equation is a second order partial differential equation which determines the metric tensor  $g_{ab}$  of spacetime. We work with the coupled system of Einstein and relativistic perfect fluid equations,

$$G_{ab} = \kappa T_{ab}, \quad (2.1)$$

$$\nabla_a T^{ab} = 0, \quad (2.2)$$

$$\nabla_a(\rho u^a) = 0, \quad (2.3)$$

with the latter two equations being the local conservation laws of stress-energy and current density. As usual,  $\nabla_a$  denotes the covariant derivative of spacetime ( $a \in (0, 1, 2, 3)$ ), and we use the summation convention, where summation is performed over repeated indices. The energy-momentum tensor of a perfect fluid has the form

$$T_{ab} = \rho h u_a u_b + p g_{ab}. \quad (2.4)$$

In this expression  $\rho$  denotes the rest mass density,  $h = 1 + \epsilon + \frac{p}{\rho}$  is the specific enthalpy,  $\epsilon$  is the specific internal energy and  $p$  is the pressure of the fluid. The four-vector  $u^a$ , the 4-velocity of the fluid, fulfills the normalization condition  $g_{ab} u^a u^b = -1$ . Using geometrized units ( $c = G = 1$ ) the coupling constant reduces to  $\kappa = 8\pi$ . Whenever we deal with stellar objects, we further use  $M_\odot = 1$ , which defines a natural length scale  $L = GM_\odot c^{-2}$ , i.e.  $L = 1.477 \times 10^5$  cm in cgs units. In order to close the system of fluid equations, an equation of state (EoS) has to be prescribed,  $p = p(\rho, \epsilon)$ .

The physical setup described in Chapter 5, where we include a scalar field as an additional matter field, deviates slightly from what is described in the present chapter. In order to facilitate the presentation, we will discuss the necessary modifications introduced by the scalar field in Chapter 5.

## 2.1 The Einstein equations for the Bondi metric

As a geometric and coordinate framework we use the Bondi (radiative) metric [18] to describe line element of spacetime  $ds^2 = g_{ab}dx^a dx^b$  as

$$ds^2 = - \left( \frac{V}{r} e^{2\beta} - U^2 r^2 e^{2\gamma} \right) du^2 - 2e^{2\beta} dudr - 2Ur^2 e^{2\gamma} dud\theta + r^2 (e^{2\gamma} d\theta^2 + e^{-2\gamma} \sin^2 \theta d\phi^2), \quad (2.5)$$

with coordinates  $(x^0, x^1, x^2, x^3) = (u, r, \theta, \phi)$ , where the  $u$  coordinate is defined by the level surfaces of a null scalar (i.e., a scalar  $u$  satisfying  $\nabla^a u \nabla_a u = 0$ ).  $r$  is the radial coordinate whose level surfaces (two-spheres) have area  $4\pi r^2$ , and  $\theta$  and  $\phi$  are angular coordinates propagated along the different null directions, i.e., they parameterize the light rays on the null cone. Restricting to axisymmetry,  $\phi$  is a Killing coordinate, the metric tensor is independent of the particular value of the coordinate  $\phi$ .<sup>1</sup> The metric functions  $V$ ,  $U$ ,  $\beta$  and  $\gamma$  only depend on the coordinates  $u$ ,  $r$  and  $\theta$ . We choose the origin of the coordinate system  $r = 0$  to lie on the axis of our axisymmetric stellar configurations. Fig. 2.1 shows the physical setting of our coordinate system.

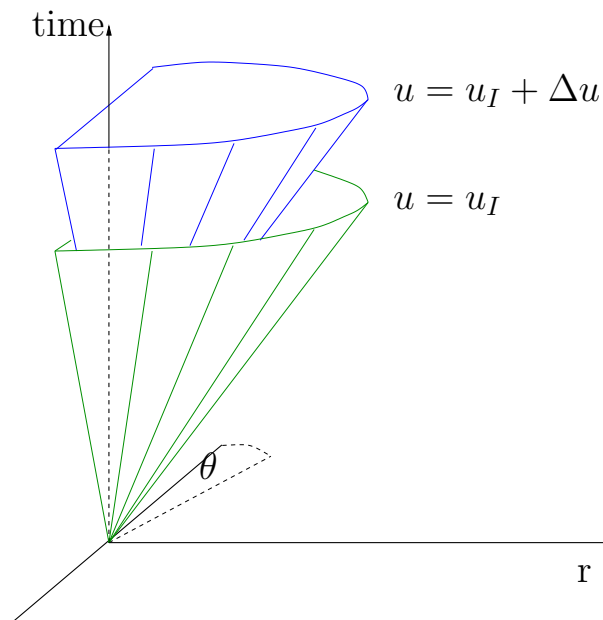


Figure 2.1: Foliation of the spacetime by null hypersurfaces (light cones): Starting from the geodesic of a freely falling particle, which defines the origin of the coordinate system, surface forming light rays are emitted. We define a new time coordinate  $u$  to be constant along each outgoing light cone. The Killing coordinate  $\phi$  is suppressed in the diagram. The origin of the coordinate system coincides with the symmetry axis of the star.

---

<sup>1</sup>Mathematically, a Killing vector  $X^a$  is defined by the Killing equation  $\nabla_a X_b + \nabla_b X_a = 0$ . Killing vectors are related to the symmetries of spacetime. Adapting coordinates to the symmetry defines a Killing coordinate.



With the above assumptions, the gravitational field equations expressed in terms of the Ricci tensor  $R_{ab}$ , which is related to the Einstein tensor  $G_{ab}$  as

$$R_{ab} - \frac{1}{2}g_{ab}R = G_{ab} \quad (2.6)$$

(where  $R = g^{cd}R_{cd}$ ), read explicitly

$$R_{ab} = \kappa \left( \rho h(u_a u_b + \frac{1}{2}g_{ab}) - p g_{ab} \right), \quad (2.7)$$

where the relevant components are

$$\frac{r}{4}R_{rr} = \beta_{,r} - \frac{r}{2}(\gamma_{,r})^2, \quad (2.8)$$

$$2r^2 R_{r\theta} = (r^4 e^{2(\gamma-\beta)} U_{,r})_{,r} - 2r^2(\beta_{,r\theta} - \gamma_{,r\theta} + 2\gamma_{,r}\gamma_{,\theta} - \frac{2}{r}\beta_{,\theta} - 2\gamma_{,r} \cot \theta), \quad (2.9)$$

$$\begin{aligned} -r^2 e^{2\beta} g^{AB} R_{AB} &= 2V_{,r} + \frac{1}{2}r^4 e^{2(\gamma-\beta)} (U_{,r})^2 - r^2 U_{,r\theta} - 4r U_{,\theta} - r^2 U_{,r} \cot \theta \\ &\quad - 4r U \cot \theta + 2e^{2(\beta-\gamma)} \{-1 - (3\gamma_{,\theta} - \beta_{,\theta}) \cot \theta - \gamma_{,\theta\theta} + \beta_{,\theta\theta} \\ &\quad + (\beta_{,\theta})^2 + 2\gamma_{,\theta}(\gamma_{,\theta} - \beta_{,\theta})\}, \end{aligned} \quad (2.10)$$

$$\begin{aligned} -r^2 e^{2\beta} g^{\phi\phi} R_{\phi\phi} &= 2r(r\gamma)_{,ur} + (1 - r\gamma_{,r})V_{,r} - (r\gamma_{,rr} + \gamma_{,r})V - r(1 - r\gamma_{,r})U_{,\theta} \\ &\quad - r^2(\cot \theta - \gamma_{,\theta})U_{,r} + e^{2(\beta-\gamma)} \{-1 - (3\gamma_{,\theta} - 2\beta_{,\theta}) \cot \theta - \gamma_{,\theta\theta} \\ &\quad + 2\gamma_{,\theta}(\gamma_{,\theta} - \beta_{,\theta})\} + r U(2r\gamma_{,r\theta} + 2\gamma_{,\theta} + r\gamma_{,r} \cot \theta - 3 \cot \theta). \end{aligned} \quad (2.11)$$

In Eq. (2.10)  $A, B$  denote the angular coordinates,  $A, B = 2, 3$ . As usual a comma is used to denote a partial derivative.

The Einstein equations decompose into hypersurface equations, evolution equations and conservation laws. The hypersurface equations, Eqs. (2.8)-(2.10), form a hierarchical set for  $\beta_{,r}$ ,  $U_{,r}$  and  $V_{,r}$ . The evolution equation is an expression for  $(r\gamma)_{,ur}$  given by Eq. (2.11). The light-cone problem is formulated in the region of spacetime between a timelike worldtube  $\Upsilon$ , which in our case is located at the origin of the radial coordinate  $r = 0$ , and future null infinity  $\mathcal{J}^+$ . Initial data for  $\gamma$  is prescribed on an initial light cone  $u = 0$  in this domain. Boundary data for  $\beta$ ,  $U$ ,  $V$  and  $\gamma$  is also required on  $\Upsilon$ .

As shown in the original paper of Bondi [18], the contracted Bianchi identities  $\nabla_b G^b_a = 0$  for the vacuum field equations enforce all other Ricci tensor components to vanish, if they vanish on a worldline. In the same way one can show, that the contracted Bianchi identities for the matter system guarantee the validity of all other components of the Einstein equation (2.7) (see [75]).

The reformulation of the above form of the equations for numerical integrations follows the work of Ref. [60]. First, in order to be able to compactify spacetime and to better resolve interesting parts of a spacetime (e.g. a stellar configuration centered at  $r = 0$ ) we allow, starting from a radial coordinate  $x \in [0, 1]$ , for a coordinate transformation of the radial coordinate

$$x \rightarrow r(x), \quad (2.12)$$

with an associated derivative needed later

$$dx/dr = f^2(x). \quad (2.13)$$

This transformation generalizes the results of [60], where the fixed grid  $r(x) = x/(1-x)$  was used. Furthermore, in order to eliminate singular terms at the poles we use the new coordinate [115]

$$y = -\cos \theta \quad (2.14)$$

and we substitute the metric fields  $(V, U, \gamma)$  by the new variables  $(S, \hat{U}, \hat{\gamma})$

$$S = \frac{V-r}{r^2}, \quad (2.15)$$

$$\hat{U} = \frac{U}{\sin \theta}, \quad (2.16)$$

$$\hat{\gamma} = \frac{\gamma}{\sin^2 \theta}. \quad (2.17)$$

The metric, Eq. (2.5), hence, takes the form

$$ds^2 = \left( -\frac{V}{r} e^{2\beta} + U^2 r^2 e^{2\gamma} \right) du^2 - 2f^{-2} e^{2\beta} dudx - 2\hat{U} r^2 e^{2\gamma} dudy + r^2 (e^{2\gamma} \sin^{-2} \theta dy^2 + e^{-2\gamma} \sin^2 \theta d\phi^2). \quad (2.18)$$

The hypersurface equations (2.8)-(2.10) thus read

$$\beta_{,x} = \frac{r}{2} f^2 \bar{y}^2 (\hat{\gamma}_{,x})^2 + \frac{r}{4} f^2 R_{xx}, \quad (2.19)$$

$$\left( r^4 f^2 e^{2(\hat{\gamma}\bar{y}-\beta)} \hat{U}_{,x} \right)_{,x} = 2r^2 \left\{ \beta_{,xy} - \frac{2}{r f^2} \beta_{,y} + 4y \hat{\gamma}_{,x} + \bar{y} [2\hat{\gamma}_{,x} (\bar{y} \hat{\gamma}_{,y} - 2y \hat{\gamma}) - \hat{\gamma}_{,xy}] \right\} + 2r^2 R_{xy}, \quad (2.20)$$

$$\begin{aligned} r^2 f^2 S_{,x} + 2rS &= -1 - 4ry\hat{U} - r^2 f^2 y \hat{U}_{,x} + 2r\bar{y} \hat{U}_{,y} + \bar{y} \left( \frac{r^2}{2} f^2 \hat{U}_{,xy} \right. \\ &\quad \left. - \frac{r^4}{4} f^4 e^{2(\hat{\gamma}\bar{y}-\beta)} (\hat{U}_{,x})^2 \right) - e^{2(\beta-\hat{\gamma}\bar{y})} \left\{ -1 - 12\hat{\gamma} - 2y\beta_{,y} \right. \\ &\quad \left. + \bar{y} [10\hat{\gamma} + 8y\hat{\gamma}_{,y} + 8\hat{\gamma}^2 + 4y\hat{\gamma}\beta_{,y} + \beta_{,yy} + (\beta_{,y})^2] \right. \\ &\quad \left. - \bar{y}^2 [8\hat{\gamma}^2 + 2\hat{\gamma}_{,y}\beta_{,y} + \hat{\gamma}_{,yy} + 8y\hat{\gamma}\hat{\gamma}_{,y}] + 2\bar{y}^3 (\hat{\gamma}_{,y})^2 \right\} \\ &\quad - \frac{r^2}{2} e^{2\beta} g^{AB} R_{AB}. \end{aligned} \quad (2.21)$$

We have used here the notation  $\bar{y} = 1 - y^2$  and  $(\cdot)_{,x}$  and  $(\cdot)_{,y}$  to denote the partial derivatives with respect to  $x$  and  $y$ , in contrast to the partial derivatives with respect to  $r$  and  $\theta$ . Note, that the Ricci tensor components are those in  $x, y$ -coordinates.

Due to this choice of variables, the Einstein equations are non-singular on the polar axis, where  $y = \pm 1$ . Note, that the  $y$ -component of the four-velocity fulfills

$$u_y = \frac{u_\theta}{\sin \theta}, \quad (2.22)$$

which is in analogy to Eq. (2.16).

The evolution equation for  $\hat{\gamma}$  is written in the form of a wave equation for the quantity  $\hat{\psi}$

$$\hat{\psi} = r\hat{\gamma}, \quad (2.23)$$

$$\tilde{g}^{ab}\tilde{\nabla}_a\tilde{\nabla}_b\hat{\psi} = -e^{-2\beta}\hat{H}, \quad (2.24)$$

where quantities denoted with a tilde are defined with respect to the 2-metric

$$d\sigma^2 = -\frac{V}{r}e^{2\beta}du^2 - 2e^{2\beta}du\,dr, \quad (2.25)$$

i.e. explicitly

$$\tilde{g}^{ab}\tilde{\nabla}_a\tilde{\nabla}_b\hat{\psi} = -e^{-2\beta}(2\hat{\psi}_{,ur} - (\frac{V}{r}\hat{\psi}_{,r}),_r), \quad (2.26)$$

and

$$\begin{aligned} \hat{H} = & -\frac{r}{2}f^2\hat{U}_{,xy} - \hat{U}_{,y} - rf^2\hat{\gamma}_{,x}\hat{U}_{,y}\bar{y} + \frac{r^3}{4}f^4e^{2(\hat{\gamma}\bar{y}-\beta)}(\hat{U}_{,x})^2 - (S + rf^2S_{,x})\hat{\gamma} \\ & + \frac{1}{r}e^{2(\beta-\hat{\gamma}\bar{y})}(\beta_{,yy} + (\beta_{,y})^2) + 4\hat{\gamma}\hat{U}_{,y} + 2rf^2\hat{\gamma}\hat{U}_{,xy} + 6rf^2\hat{\gamma}_{,x}\hat{U}_{,y} \\ & - \bar{y}\left(rf^2\hat{\gamma}_{,y}\hat{U}_{,x} + 2rf^2\hat{\gamma}_{,xy}\hat{U} + 2\hat{\gamma}_{,y}\hat{U}\right) + \frac{1}{2r}e^{2(\beta-\hat{\gamma}\bar{y})}\kappa\rho hu_y u_y. \end{aligned} \quad (2.27)$$

For the derivation of the last equation, we have used Eqs. (2.10)-(2.11), the coordinate relations Eqs. (2.12)-(2.14) and Eq. (2.7).

## 2.2 The relativistic perfect fluid equations

In this section, we will describe the form of the hydrodynamic equations for our axisymmetric perfect fluid system. We will further present the equations of state used in our simulations and the method to obtain initial data for the stellar objects.

### 2.2.1 General relativistic hydrodynamics in axisymmetry

Whereas Eq. (2.3) is a strict conservation law, Eq. (2.2) involves source terms when writing the covariant derivatives in terms of partial derivatives. In the presence of a Killing vector field it can be recast as a conservation law. Following [117], the number of source terms in Eq. (2.2) is minimized using the equivalent form

$$\nabla_a T^a_b = 0. \quad (2.28)$$

Nevertheless, in our hydrodynamics code we use the form given by Eq. (2.2) in order to set up the evolution equation for the radial momentum. This is motivated by stability considerations when evolving spherical neutron star models. However, to set up the evolution equation for the polar component of the momentum we use Eq. (2.28). This form of the conservation law eliminates singular behavior of the  $y$ -component of the velocity at the polar axis.

We work with two mathematically equivalent systems for the hydrodynamics. In the first system we include the square root of the metric determinant  $\sqrt{-g}$  in the definition of the conserved quantities. After defining the conserved quantities  $U^u = \sqrt{-g}T^{uu}$ ,  $U^x = \sqrt{-g}T^{ux}$ ,

$U_y = \sqrt{-g}T_y^u$  and  $U^4 = \sqrt{-g}\rho u^u$ , the fluid equations can be cast into a first-order flux-conservative, hyperbolic system for the state-vector  $\mathbf{U} = (U^u, U^x, U_y, U^4)$

$$\partial_u U^u + \partial_j F^{ju} = S^u, \quad (2.29)$$

$$\partial_u U^x + \partial_j F^{jx} = S^x, \quad (2.30)$$

$$\partial_u U_y + \partial_j F_y^j = S_y, \quad (2.31)$$

$$\partial_u U^4 + \partial_j F^{j4} = S^4. \quad (2.32)$$

The flux vectors are defined as

$$F^{ju} = \sqrt{-g} T^{ju}, \quad (2.33)$$

$$F^{jx} = \sqrt{-g} T^{jx}, \quad (2.34)$$

$$F_y^j = \sqrt{-g} T_y^j, \quad (2.35)$$

$$F^{j4} = \sqrt{-g} \rho u^j, \quad (2.36)$$

and the corresponding source terms read

$$S^a = g^{ab} S_b + \sqrt{-g} T_b^c (g^{ab})_{,c}, \quad (2.37)$$

$$\begin{aligned} S_a &= \sqrt{-g} T_c^b \Gamma_{ab}^c \\ &= -\frac{\sqrt{-g}}{2} \rho h u_c u_d (g^{cd})_{,a} + p (\sqrt{-g})_{,a}, \end{aligned} \quad (2.38)$$

$$S^4 = 0, \quad (2.39)$$

where all expressions are evaluated in the coordinate system  $(u, x, y, \phi)$ , and  $\Gamma_{bc}^a$  are the Christoffel symbols.

In a second system, we do not incorporate the metric determinant in the definition of the conserved quantities. For such a system, the continuity equation is in general not a strict conservation law any longer. However, this system has the advantage, that the recovery of the primitive fluid variables from the conserved quantities  $\mathbf{U}$  at the origin does not involve terms which have to be otherwise regularized (as the metric determinant vanishes there). We use this system for the studies of supernova core collapse in Chapter 7. With the definitions for the conserved quantities  $\mathbf{U} = (U^u, U^x, U_y, U^4)$ ,  $U^u = T^{uu}$ ,  $U^x = T^{ux}$ ,  $U_y = T_y^u$  and  $U^4 = \rho u^u$ , the fluxes read

$$F^{ju} = T^{ju}, \quad (2.40)$$

$$F^{jx} = T^{jx}, \quad (2.41)$$

$$F_y^j = T_y^j, \quad (2.42)$$

$$F^{j4} = \rho u^j, \quad (2.43)$$

and the corresponding source terms read

$$S^a = -(\ln(\sqrt{-g}))_{,b} T^{ab} + g^{ab} S_b + T_b^c (g^{ab})_{,c}, \quad (2.44)$$

$$S_a = -\frac{1}{2} \rho h u_c u_d (g^{cd})_{,a} + p - (\ln(\sqrt{-g}))_{,b} T_a^b, \quad (2.45)$$

$$S^4 = -(\ln(\sqrt{-g}))_{,b} \rho u^b. \quad (2.46)$$

### 2.2.2 Equations of state

We turn next to summarize all equations of state (EoS) used in this work. These EoS describe the physical conditions encountered in neutron stars and during supernova core collapse only approximately, more detailed modeling is needed for a realistic description. We note that the understanding of the EoS of neutron stars is still quite limited [71, 5]. Therefore we only consider simple model EoS since the focus of this work lies on a general relativistic description.

We start with the thermodynamical relation [103] for the total energy  $\eta = \rho(1 + \epsilon)$

$$d\eta = \frac{\eta + p}{\rho} d\rho + \rho T ds, \quad (2.47)$$

where  $s$  denotes the specific entropy of the fluid. The relativistic generalization of the speed of sound (see e.g. [43]) is

$$c_s^2 = \left. \frac{\partial p}{\partial \eta} \right|_s. \quad (2.48)$$

Assuming adiabaticity in Eq. (2.47), we find  $d\epsilon = \frac{p}{\rho^2} d\rho$ . Using this equation in the formula for the sound speed (2.48), we obtain

$$hc_s^2 = \left. \frac{\partial p}{\partial \rho} \right|_\epsilon + \frac{p}{\rho^2} \left. \frac{\partial p}{\partial \epsilon} \right|_\rho. \quad (2.49)$$

#### The ideal fluid EoS

For the ideal fluid equation of state, the pressure is proportional to the internal energy as

$$p = (\Gamma - 1)\rho\epsilon \quad (2.50)$$

with the adiabatic index  $\Gamma$ . The sound speed can be easily calculated as

$$hc_s^2 = \frac{p}{\rho}\Gamma. \quad (2.51)$$

#### The polytropic EoS

The polytropic EoS [148] is a special case of a barotropic EoS  $p = p(\rho)$ . The pressure reads

$$p = \kappa\rho^\Gamma, \quad (2.52)$$

where  $\kappa$  is the polytropic constant and  $\Gamma$  the adiabatic exponent. The polytropic index  $n$  is related to  $\Gamma$  by  $\Gamma = 1 + \frac{1}{n}$ . The internal energy is defined according to Eq. (2.50). For adiabatic flows, it can be easily shown, that assuming the relations (2.50) and (2.52) the thermodynamical identity  $d\eta = hd\rho$  (which is equivalent to Eq. (2.47) under the assumption of constant entropy,  $ds = 0$ ) is trivially fulfilled (without recourse to the hydrodynamical equations). Moreover, it follows from the thermodynamical identity  $d\eta = hd\rho$  and the continuity equation, that

$$u_b(\nabla_a T^{ab}) = 0. \quad (2.53)$$

Hence, choosing an index  $c$  with  $u_c \neq 0$  and imposing Eqs. (2.50), (2.52), the continuity equation and all fluid equations  $\nabla_a T^{ab} = 0$  with  $b \neq c$ , the remaining equation  $\nabla_a T^{ac} = 0$  is trivially

fulfilled.

The polytropic EoS is widely used in the literature to obtain general relativistic models of neutron stars (this is the so-called *relativistic star* model). For our models of neutron stars, we mainly choose a stiff adiabatic exponent of  $\Gamma = 2$ .

### The hybrid EoS

For the simulation of supernova core collapse in Chapter 7, we refine the polytropic EoS to include the effect of stiffening at nuclear densities and the effect of thermal heating due to the appearance of shocks. Our EoS was first considered in the work of Janka [79], and was already used for Newtonian supernova core collapse simulations [169, 127] and for general relativistic simulations in the conformally flat metric approximation [30, 31, 32].

For the hybrid EoS, the total pressure consists of a polytropic part, which takes into account the contribution from the degenerate electron gas, as well as the nuclear forces (at high densities), and a thermal part due to the heating of the material by a shock,

$$p = p_p + p_{th}. \quad (2.54)$$

More precisely, the polytropic part is assumed to follow the relation

$$p_p = \begin{cases} \kappa_1 \rho^{\Gamma_1} & \text{for } \rho \leq \rho_n, \\ \kappa_2 \rho^{\Gamma_2} & \text{for } \rho > \rho_n, \end{cases} \quad (2.55)$$

where we assume a nuclear density  $\rho_n = 2 \times 10^{14} \text{ g cm}^{-3}$ . For a degenerate electron gas, we have [133]  $\Gamma = \Gamma_{ini} = 4/3$  and  $\kappa = 4.8974894 \times 10^{14} \text{ [cgs]}$ . To model the physical processes which lead to the onset of the collapse, we reduce the effective adiabatic index from  $\Gamma$  to  $\Gamma_1$  setting  $\kappa_1 = \kappa$  at our initial slice. To model the stiffening of the equation of state at nuclear densities, we assume  $\Gamma_2 = 2.5$ . The value of the polytropic constant  $\kappa_2$  follows from the requirement that the pressure is continuous at nuclear density. The thermodynamically consistent internal energy distribution reads

$$\epsilon_p = \begin{cases} \frac{\kappa_1}{\Gamma_1 - 1} \rho^{\Gamma_1 - 1} & \text{for } \rho \leq \rho_n, \\ \frac{\kappa_2}{\Gamma_2 - 1} \rho^{\Gamma_2 - 1} + E & \text{for } \rho > \rho_n. \end{cases} \quad (2.56)$$

The requirement that  $\epsilon_p$  is continuous at nuclear density leads to

$$E = \frac{(\Gamma_2 - \Gamma_1)\kappa_1}{(\Gamma_2 - 1)(\Gamma_1 - 1)} \rho_n^{\Gamma_1 - 1}. \quad (2.57)$$

For the thermal contribution to the total pressure, we assume an ideal fluid EoS

$$p_{th} = (\Gamma_{th} - 1)\rho\epsilon_{th}, \quad (2.58)$$

with an adiabatic index  $\Gamma_{th} = \frac{3}{2}$  describing a mixture of relativistic and non-relativistic gases. The internal thermal energy  $\epsilon_{th}$  is simply obtained from

$$\epsilon_{th} = \epsilon - \epsilon_p. \quad (2.59)$$

We can summarize the EoS in a single equation

$$p = \kappa \left( 1 - \frac{\Gamma_{th} - 1}{\Gamma - 1} \right) \rho^\Gamma + (\Gamma_{th} - 1) \rho \epsilon - \frac{(\Gamma_{th} - 1)(\Gamma - \Gamma_1)}{(\Gamma_2 - 1)(\Gamma_1 - 1)} \kappa \rho_n^{\Gamma-1} \rho, \quad (2.60)$$

where  $\Gamma$  and  $\kappa$  change discontinuously at nuclear density  $\rho_n$  from  $\Gamma_1$  to  $\Gamma_2$  and  $\kappa_1$  to  $\kappa_2$ . For the sound speed  $c_s$ , we obtain

$$hc_s^2 = \frac{1}{\rho} (\Gamma p_p + \Gamma_{th} p_{th}). \quad (2.61)$$

### 2.2.3 Equilibrium models for spherically symmetric stars

In order to set up equilibrium models for relativistic stars we numerically solve the Tolman-Oppenheimer-Volkoff equations in outgoing null coordinates [119]

$$p_{,r} = \left( \frac{1}{2r} - \frac{1}{2Y} (1 + 8\pi r^2 p) \right) \rho h, \quad (2.62)$$

$$Y_{,r} = 1 + 8\pi r^2 (p - \rho h), \quad (2.63)$$

where  $Y = Ve^{-2\beta}$ . Starting with this equilibrium solution, we also prescribe perturbations for the study of stellar oscillations (Chapter 6) and gravitational collapse (Chapter 7). In these cases, in order to obtain consistent initial data, we have to solve the hypersurface equations (2.8)-(2.10) imposing the normalization condition of the 4-velocity.

## 2.3 Gravitational waves

One of the main advantages of the characteristic approach is the possibility of treating gravitational waves without approximation. By using a compactified coordinate  $x \in [0, 1]$  with  $\lim_{x \rightarrow 1} r(x) = \infty$  to cover an asymptotically flat spacetime, we have future null infinity  $\mathcal{J}^+$  on our grid, where we can unambiguously extract waveforms (see [45] for a recent review). Fig 2.2 shows a schematic Penrose diagram of spacetime of an isolated neutron star or a supernova event. The figure includes two null slices, which start at the origin of the coordinate system and extend to future null infinity. For a comparison, Fig 2.3 shows the same diagram, now with two Cauchy slices. Extending these Cauchy slices to infinity, they would end at spacelike infinity  $i^0$ . However, this approach cannot be used for a numerical evolution of data forward of time, as outgoing waves at large distances cannot be resolved any more. As a consequence, the Cauchy approach has to deal with outer boundaries of the numerical domain. These outer boundaries are difficult to handle - not only because of possible numerical instabilities - one also has to ensure that no incoming gravitational radiation is created due to the boundary treatment. Moreover, for the gravitational wave extraction in the Cauchy approach, one in general linearizes the metric equations at the outer boundary around a background metric.

In contrast, having included  $\mathcal{J}^+$  on the grid, the characteristic approach can work with gravitational waves in the fully nonlinear theory of general relativity. Hence, it does not suffer from the problem most Cauchy numerical relativity codes have to deal with, i.e. extracting approximate gravitational waveforms at a finite distance (for a comparison, see [63, 76]).

We will describe the gravitational wave extraction at null infinity in more detail in Sec. 2.3.1. At the same time it is possible to establish the quadrupole radiation formula on the null cone, which we describe in Sec. 2.3.2.

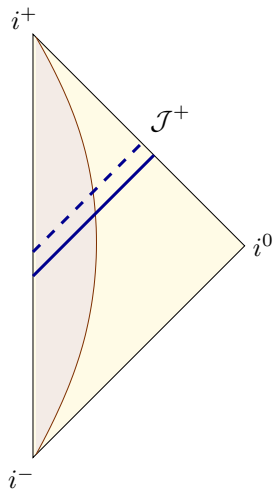


Figure 2.2: Penrose diagram of a neutron star spacetime. With the help of a conformal mapping, the physical spacetime is mapped onto the compactified region defined by the triangle. The dark pattern shows the part of spacetime filled by the neutron star. All timelike curves, like the radius of the star, start at past timelike infinity  $i^-$  and end at future timelike infinity  $i^+$ . The diagonal lines correspond to two null slices, which start at the origin and end at future null infinity  $\mathcal{J}^+$ .

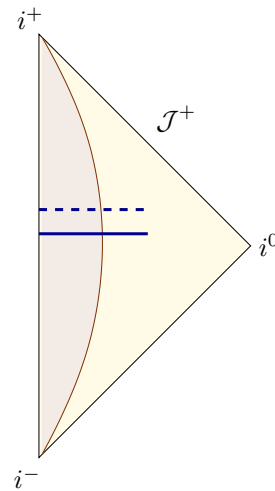


Figure 2.3: Same diagram as Fig. 2.2, but now with two Cauchy slices. Every spacelike curve extending to infinity ends at spatial infinity  $i^0$ . In the case of Cauchy slices, it is not possible to extend the slices to (spatial) infinity in the initial value problem. Boundary conditions have to be prescribed at a finite distance.

### 2.3.1 Gravitational waves at null infinity

In the original paper of Bondi [18], it was shown how to identify the quantities related to the total mass of spacetime (Bondi mass) and to the gravitational radiation (Bondi news) in an asymptotic expansion of the metric fields at future null infinity. In what we describe here, we follow the work of [75]. The main difference between the two approaches stems from the definition of the coordinate systems. In contrast to the original work, where the coordinates were chosen in such a way, that they reduce to Minkowski coordinates for large radii, we have imposed regularity conditions at the vertex of the light cones. Imposing the regularity conditions at the origin, which is necessary to work with regular spacetimes of a neutron star or core collapse, the coordinate system does not reduce to a Minkowski coordinate system for large radii. As a consequence, additional gauge terms appear in the definition of global quantities read off at future null infinity.

Covering the entire radial domain from the origin to infinity with a light cone, we perform a power series expansion of  $\gamma$  around future null infinity in inverse powers of the radial coordinate  $r$

$$\gamma = K + \frac{c}{r} + O(r^{-2}), \quad (2.64)$$

where  $K = K(\theta)$  and  $c = c(\theta)$ . Under this assumption the hypersurface equations (2.8)-(2.10)



yield an asymptotic expansion [75] at infinity as

$$\beta = H + O(r^{-2}), \quad (2.65)$$

$$U = L + O(r^{-1}), \quad (2.66)$$

$$V = r^2(L \sin \theta)_{,\theta} / \sin \theta + r e^{2(H-K)} [1 + K_{,\theta\theta} + 2(H_{,\theta} \sin \theta)_{,\theta} / \sin \theta + 3K_{,\theta} \cot \theta + 4(H_{,\theta})^2 - 4H_{,\theta}K_{,\theta} - 2(K_{,\theta})^2] - 2e^{2H}M + O(r^{-1}), \quad (2.67)$$

where  $H = H(\theta)$ ,  $L = L(\theta)$ , and  $M = M(\theta)$  denotes the Bondi mass aspect, which results in the total mass of spacetime when integrated over the angular domain. A straightforward determination of  $M(\theta)$  at  $\mathcal{J}^+$  by simply reading of the corresponding coefficient in a numerical simulation will be corrupted by numerical errors appearing in the leading, diverging terms in Eq. (2.67). Therefore we follow the procedure proposed in [61] to determine the Bondi mass of a numerical spacetime. We numerically solve the hypersurface equations for the new metric variables  $(\tau, \mu)$  defined by

$$2\tau = (1 - y^2)^{-1/2} r^3 e^{2(\gamma-\beta)} U_{,r} + 2r\beta_{,y} - r^2(1 - y^2)^{-1} e^{2\gamma} [(1 - y^2)e^{-2\gamma}]_{,ry}, \quad (2.68)$$

$$2\mu = -V + r^2[(1 - y^2)^{1/2}U]_{,y} + r^3 e^{2\beta} \left[ \frac{1}{2r} (1 - y^2) e^{-2\gamma} \right]_{,yyr} + e^{2\beta} [(1 - y^2) e^{-2\gamma} \tau]_{,y} \quad (2.69)$$

(see [61] for more details). The mass aspect enters the leading term of  $\mu$  in an asymptotic expansion at null infinity. More precisely, the Bondi mass  $M_B$  can then be readily computed as

$$M_B = \frac{1}{4\pi} \int \omega^{-1} e^{-2H} \mu|_{x=1} \sin \theta \, d\theta \, d\phi, \quad (2.70)$$

where  $\omega$  denotes the conformal factor relating the two-geometry

$$d\hat{s}^2 = e^{2K} d\theta^2 + \sin^2 \theta e^{-2K} d\phi^2 \quad (2.71)$$

to the two-geometry of a unit sphere

$$d\hat{s}_B^2 = d\theta_B^2 + \sin^2 \theta_B d\phi_B^2, \quad (2.72)$$

i.e.

$$d\hat{s}_B^2 = \omega^2 d\hat{s}^2. \quad (2.73)$$

The total energy emitted by gravitational waves during the time interval  $[u, u + du]$  in angular directions  $[\theta, \theta + d\theta] \times [\phi, \phi + d\phi]$  is [75]

$$dE = \frac{1}{16\pi} \omega^{-1} e^{-2H} \left\{ 2c_{,u} + \frac{(\sin \theta \, c^2 \, L)_{,\theta}}{\sin \theta \, c} + e^{-2K} \omega \sin \theta \left[ \frac{(e^{2H} \omega)_{,\theta}}{\omega^2 \sin \theta} \right]_{,\theta} \right\}^2 \sin \theta \, d\theta \, d\phi \, du. \quad (2.74)$$

The quantities  $K, c, H$  and  $L$  (see Eqs. (2.64)-(2.66)) are read off from the metric variables at  $\mathcal{J}^+$ , e.g.  $c = -(r^2 f^2 \frac{d\gamma}{dx})|_{x=1}$  (our coordinate transformations  $r = r(x)$  fulfill the requirement that  $r^2 f^2$  is finite).

For the extraction of waveforms seen by a distant inertial observer, we have to transform our coordinate system to a Bondi coordinate system  $(u_B, y_B)$ . Only by introducing inertial observers at infinity, it is possible to rigorously identify gravitational waves in the full theory of

general relativity. Following [11] the Bondi coordinate time  $u_B$  is related to the retarded time  $u$  as

$$du = \frac{1}{\omega} e^{-2H} du_B, \quad (2.75)$$

whereas the angular Bondi coordinate  $y_B = -\cos(\theta_B)$  can be calculated from

$$dy = \frac{1}{\omega^2} dy_B. \quad (2.76)$$

With the definition of the Bondi news function

$$N = \frac{1}{2} \frac{e^{-2H}}{\omega^2} \left\{ 2c_{,u} + \frac{(\sin \theta \ c^2 \ L)_{,\theta}}{\sin \theta \ c} + e^{-2K} \omega \sin \theta \left[ \frac{(e^{2H} \omega)_{,\theta}}{\omega^2 \sin \theta} \right] \right\}, \quad (2.77)$$

and after integrating over angles  $\phi = \phi_B$ , one recovers the expression for the total energy radiated according to Bondi [18]

$$dE = \frac{1}{2} N^2 dy_B du_B. \quad (2.78)$$

This relation allows us to check global energy conservation

$$ec := M_B(u) - M_B(u=0) + \int_0^u \int_{-1}^1 dE = 0. \quad (2.79)$$

For the calculation of the Bondi mass, Eq. (2.70), as well as for the calculation of the Bondi news, Eq. (2.77), we have to determine the conformal factor  $\omega$ . Using the definition Eq. (2.73) and the relation  $d\phi = d\phi_B$ , it can be shown that the coordinate  $y_B = -\cos(\theta_B)$  reads

$$y_B(y) = \tanh \left( \frac{1}{2} \int_{-1}^y \frac{e^{2K} - 1}{1 - \tilde{y}^2} d\tilde{y} + \frac{1}{2} \int_1^y \frac{e^{2K} - 1}{1 - \tilde{y}^2} d\tilde{y} + \int_0^y \frac{1}{1 - \tilde{y}^2} d\tilde{y} \right). \quad (2.80)$$

The choice of the integration constants in the integrals ensures regularity of  $y_B$ , i.e.  $\lim_{y \rightarrow \pm 1} y_B = \pm 1$  and for spacetimes with equatorial plane symmetry,  $y_B$  is symmetric as well. The conformal factor can be written as

$$\omega = \frac{2e^K}{(1+y)e^\Delta + (1-y)e^{-\Delta}}, \quad (2.81)$$

where

$$\Delta(y) = \frac{1}{2} \int_{-1}^y \frac{e^{2K} - 1}{1 - \tilde{y}^2} d\tilde{y} + \frac{1}{2} \int_1^y \frac{e^{2K} - 1}{1 - \tilde{y}^2} d\tilde{y}. \quad (2.82)$$

In order to show, that the conformal factor is regular, we write Eq. (2.82) as

$$\Delta(y) = \int_{-1}^y d\tilde{y} \int_0^1 d\alpha e^{2\alpha K} \hat{K} + \int_1^y d\tilde{y} \int_0^1 d\alpha e^{2\alpha K} \hat{K}, \quad (2.83)$$

where using Eq. (2.17) we have defined

$$\hat{K} = \frac{K}{\sin^2 \theta}. \quad (2.84)$$

### 2.3.2 Approximate gravitational waves

The common approach to the description of gravitational waves for a fluid systems relies on the quadrupole formula [87, 103]. The standard quadrupole formula is valid for weak sources of gravitational waves under the assumptions of slow motion and wave lengths of the emitted gravitational waves much smaller than the typical extension of the source. The requirement that the sources of gravitational waves are weak includes the requirement that the gravitational forces inside the source can be neglected. This first approximation can be extended based on Post-Newtonian expansions (for a detailed description see the recent review [14] and references therein, in particular [124]).

Winicour established in a series of papers [159, 160, 76, 161] that the quadrupole radiation formula can be derived in the Newtonian limit of the characteristic field equations. Let  $Q$  be the quadrupole moment transverse to the  $(\theta, \phi)$  direction

$$Q = q^A q^B \left( \frac{x^i}{r} \right)_{,A} \left( \frac{x^j}{r} \right)_{,B} Q_{ij}, \quad (2.85)$$

where

$$Q_{ij} = \int \rho (x_i x_j - \delta_{ij} r^2 / 3) d^3 x \quad (2.86)$$

is the quadrupole tensor and  $q_A$ ,  $A = 2, 3$ , is the complex dyad for the unit sphere metric

$$d\theta^2 + \sin^2 \theta d\phi^2 = 2q_{(A} q_{B)} dx^A dx^B. \quad (2.87)$$

For our axisymmetric setup, Eq. (2.85) reads

$$Q = \pi \sin^2 \theta \int_0^R dr' \int_0^\pi \sin \theta' d\theta' r'^4 \rho \left( \frac{3}{2} \cos^2 \theta' - \frac{1}{2} \right). \quad (2.88)$$

On the level of the quadrupole approximation [161] the *quadrupole news*  $N_0$  reads

$$N_0 = \frac{d^3}{du_B^3} Q. \quad (2.89)$$

With our null foliation it is natural to evaluate the quadrupole moment (2.88) as a function of retarded time, i.e., for the evaluation of the integral we completely relax the assumption of slow motion.

It is well known [38] that the third numerical time derivative appearing in Eq. (2.89) (see also [105]) can lead to severe numerical problems resulting in numerical noise which dominates the quadrupole signal. Hence we make use of the fluid equations in the Newtonian limit to eliminate one time derivative. Defining the ‘‘Newtonian velocities’’

$$v_1 = u^r = \frac{dr}{dx} u^x, \quad (2.90)$$

$$v_2 = r u^\theta = r \frac{u^y}{\sin \theta}, \quad (2.91)$$

the quadrupole radiation formula (2.89) can be rewritten with the use of the continuity equation as the so-called *first moment of momentum formula*

$$N_0 = \frac{d^2}{du_B^2} \left( \pi \sin^2 \theta \int_0^R dr' \int_0^\pi \sin \theta' d\theta' r'^3 \rho (v_1 (3 \cos^2 \theta' - 1) - 3v_2 \sin \theta' \cos \theta') \right). \quad (2.92)$$

In reference [38] it was further shown how to eliminate one additional time derivative making use of the Euler equations. However, the resulting *stress formula* involves the Newtonian potential, which is not easily defined in our null coordinate system. As the use of the first moment of momentum formula gives already good results for the quadrupole news, we henceforth work with Eqs. (2.89) and (2.92) for the estimate of the quadrupole radiation.

Based on the quadrupole approximation, it is straightforward to define the relation between quadrupole strain (i.e. the gravitational wave signal) and the Bondi news. In the quadrupole approximation, the total power radiated in gravitational waves reads [105]

$$\frac{dE}{du_B} = \frac{1}{32\pi} \left( \frac{dA_{20}^{E2}}{du_B} \right)^2, \quad (2.93)$$

$A_{20}^{E2}$  arises as coefficient for the quadrupolar term in the expansion of the quadrupole strain  $h_+$  in spherical harmonics<sup>2</sup>

$$h_+(u_B) = \frac{1}{8} \sqrt{\frac{15}{\pi}} \sin^2 \theta \frac{A_{20}^{E2}(u_B)}{R} \quad (2.94)$$

and can be obtained in the quadrupole approximation as

$$A_{20}^{E2} = \frac{d^2}{du_B^2} M_{20}^{E2}, \quad (2.95)$$

where

$$M_{20}^{E2} \sin^2 \theta = 16 \sqrt{\frac{\pi}{15}} Q. \quad (2.96)$$

$R$  denotes the distance from the observer to the source. Comparing Eqs. (2.93) and (2.78) we find for the quadrupole strain (with the identification  $\theta_B = \theta$  and under the assumption that the news function has angular dependence  $N \propto \sin^2 \theta$ )

$$h_+(u_B) = \frac{2}{R} \left( \int_0^{u_B} N du'_B + \text{const} \right). \quad (2.97)$$

As mentioned above, the quadrupole formula is only the first term in a Post-Newtonian expansion for the gravitational radiation. The next, non-vanishing contribution to the gravitational strain for our axisymmetric configuration is the hexadecapole contribution, which reads [105]

$$h_+^{HD} = \frac{9}{8} \sqrt{\frac{5}{\pi}} \sin^2 \theta \left( 1 - \frac{7}{6} \sin^2 \theta \right) \frac{A_{40}^{E2}}{R}. \quad (2.98)$$

The quantity  $A_{40}^{E2}$  is defined as

$$A_{40}^{E2} = \frac{d^4}{du_B^4} M_{40}^{E2}, \quad (2.99)$$

$$M_{40}^{E2} = \frac{\sqrt{5}}{63} \pi^{\frac{3}{2}} \int_0^R dr' \int_0^\pi \sin \theta' d\theta' r'^6 \rho \left( 7 \cos^4 \theta' - 6 \cos^2 \theta' + \frac{3}{5} \right), \quad (2.100)$$

---

<sup>2</sup>Our notation follows the work [105].  $E2$  denotes the electric part, 20 denotes the  $l = 2, m = 0$  quadrupolar part in an expansion of the gravitational wave strain in tensor harmonics.

or alternatively

$$A_{40}^{E2} = \frac{d^4}{du_B^3} N_{40}^{E2}, \quad (2.101)$$

$$N_{40}^{E2} = \frac{4\sqrt{5}}{63} \pi^{\frac{3}{2}} \int_0^R dr' \int_0^\pi \sin \theta' d\theta' r'^5 \rho \left( v_1 (7 \cos^4 \theta' - 6 \cos^2 \theta' + \frac{3}{5}) \right. \\ \left. + v_2 (3 - 7 \cos^2 \theta') \sin \theta' \cos \theta' \right). \quad (2.102)$$



## Chapter 3

# The numerical implementation

We use an equidistant grid covering the numerical domain  $(x, y) \in [0, 1] \times [-1, 1]$  with grid spacings  $\Delta x = 1/N_x$ ,  $\Delta y = 1/N_y$ , where  $N_x + 1$  is the number of grid points in the radial direction and  $2N_y + 1$  is the number of grid points in the angular direction ( $N_y$  is the number of angular grid zones per hemisphere). All variables are defined on the grid  $(u^n, x_i, y_j) =$

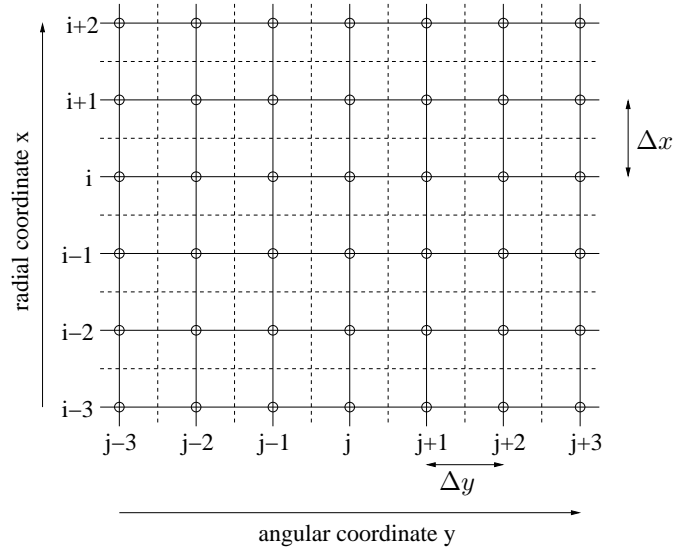


Figure 3.1: Distribution of the spatial grid cells. The vertical lines denote the curves of constant  $y$ , the horizontal lines the curves of constant  $x$ . All fluid quantities and the metric fields  $\gamma$ ,  $\beta$ ,  $S$  (and  $\mu$ ) are defined at the cross section of two solid lines. The dashed lines correspond to the cell interfaces.

$(n\Delta u, i\Delta x, j\Delta y)$  (see Fig. 3.1), except for the quantities  $\hat{U}$  and  $\tau$  which are defined on a

staggered grid  $(u^n, x_{i+1/2}, y_{j+1/2}) = (n\Delta u, (i + 1/2)\Delta x, (j + 1/2)\Delta y)$ . As it was shown by [60] for an axisymmetric characteristic code in vacuum, the use of a staggered grid is necessary for stability. This result carries over to the general relativistic matter system, since the matter terms enter the metric equations only on the level of non-principal terms.

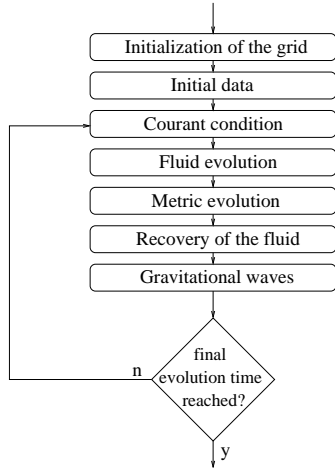


Figure 3.2: Flow chart sketching the numerical implementation for the evolution of the coupled general relativistic fluid system.

and conserved quantities at the new time slice solving a nonlinear system of algebraic equations. In the last step of the evolution loop, the physical information, in particular the gravitational wave content of the data, can be extracted. We repeat the evolution in time, until the final time has been reached.

In the following sections, we describe the different parts of the numerical implementation in more detail.

### 3.1 Implementation of the fluid equations: High-resolution shock-capturing methods

Having written the equations of general relativistic fluid dynamics in the form of Eqs. (2.29)-(2.32), they form of first order hyperbolic system of balance laws, or - in the absence of source terms - a first order hyperbolic system of conservation laws. There is a detailed mathematical theory about the well-posedness of systems of conservation laws [51] and a detailed theory about their numerical solution [90, 52]. The explicit knowledge of the characteristic information of hyperbolic systems of conservation laws provides the mathematical framework for their numerical integration by means of exact or approximate Riemann solvers. These solvers are based on the solution of local Riemann problems, i.e the solution of discontinuous initial data together with the system of conservation laws. Hence, featuring a *shock capturing* property by construction, they are very well suited to deal with weak solutions (e.g. shocks) as they

Fig. 3.2 shows a schematic flow chart of our numerical implementation. In a first step, the numerical grid as shown in Fig. 3.1 has to be created. Having the grid at hand, the initial data can be constructed, which is going to be evolved forward in time. In order to fulfill the stability requirements of the explicit numerical algorithms, we have to calculate the Courant conditions (i.e. the maximal time step) for our data. Concerning the time update, we first evolve the fluid variables forward in time. Since we use high-resolution shock-capturing schemes for the fluid update, we solve the equations not directly for the primitive quantities  $w = (\rho, u^x, u_y, \epsilon)$ , but for the conserved quantities (see Sec. 2.2.1). Having obtained the conserved quantities at the new time step, we solve for the metric variables at the new time slice. As the evolution of the metric equations requires the knowledge the primitive variables, we have to recover the latter from the metric



are encountered in astrophysical situations like the supernova core collapse. High-resolution shock-capturing schemes are capable of resolving steep gradients and discontinuous data, while providing a high order of accuracy in smooth parts of the solution. The numerical order of a particular high-resolution shock-capturing scheme depends on the procedure how the local Riemann problems are constructed from a smooth solution. This procedure is the so-called *reconstruction* scheme.

In our implementation of the fluid equations we closely follow the work of Papadopoulos and Font [117] (see also [40]). Making use of the hyperbolic mathematical character of the fluid equations we construct a (local) Riemann problem at each cell-interface of the numerical grid. At cell  $i, j$  the state-vector  $\mathbf{U}$  is updated in time (from  $u^n$  to  $u^{n+1}$ ) using a conservative algorithm

$$\begin{aligned} \mathbf{U}_{i,j}^{n+1} = \mathbf{U}_{i,j}^n & - \frac{\Delta u}{\Delta x} (\widehat{\mathbf{F}}_{i+1/2,j}^x - \widehat{\mathbf{F}}_{i-1/2,j}^x) \\ & - \frac{\Delta u}{\Delta y} (\widehat{\mathbf{F}}_{i,j+1/2}^y - \widehat{\mathbf{F}}_{i,j-1/2}^y) \\ & + \Delta u \mathbf{S}_{i,j}, \end{aligned} \tag{3.1}$$

where the numerical fluxes,  $\widehat{\mathbf{F}}^x$  and  $\widehat{\mathbf{F}}^y$ , are evaluated at the cell interfaces according to some particular exact or approximate Riemann solver or *flux-formula* which makes explicit use of the full spectral decomposition of the system. For our particular formulation of the hydrodynamic equations such characteristic information was presented in [117, 119]. The state vector is

$$\mathbf{U} = (\sqrt{-g}) \times \begin{pmatrix} T^{uu} \\ T^{ux} \\ T^u_y \\ J^u \end{pmatrix}. \tag{3.2}$$

The parentheses around the square root of the metric determinant are a visual reminder that we have included this term only in some cases (see the discussion in Sec 2.2.1). We note, as it was explicitly demonstrated in [117], that the eigenvalues and eigenvectors needed for the computation of the local Riemann problems are not affected by the inclusion or omission of the metric determinant in the above definition of the state vector. We have implemented a variety of reconstruction schemes and two approximate Riemann solvers.

### 3.1.1 Reconstruction schemes

Starting with initial data  $\mathbf{U}$  for the fluid variables at time  $u^n$ , we set up *directional* local Riemann problems at each cell interface by splitting up the two dimensional data into one dimensional data sets along the curves  $y = \text{const}$  and  $x = \text{const}$ , respectively. In the following, let us restrict the presentation to the description of the local Riemann problems along the curves  $y = \text{const}$ . With the location of the cell centers defined by  $x_i$ , the local Riemann problems are defined at interfaces  $x_{i+\frac{1}{2}}$  (see Fig. 3.3). With the data of the fluid variables  $\mathbf{U}(x)$  along the curve  $y = \text{const}$ , we define the reconstructed quantities of the fluid fields at  $x_{i+\frac{1}{2}}$  as  $\mathbf{U}_i^R$  and  $\mathbf{U}_{i+1}^L$ , where the upper indices  $R$  denotes right (to indicate the location of the interface with respect to the grid center  $x_i$ ) and  $L$  left, respectively. For the explicit definition of the reconstructed quantities, see the different reconstruction schemes below.

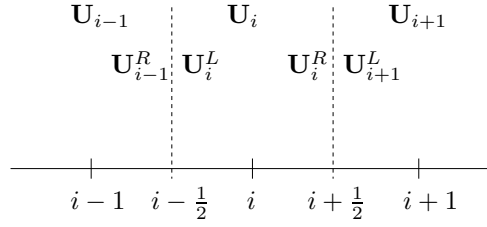


Figure 3.3: Definition of the reconstructed quantities at the interfaces  $\mathbf{U}_i^R$  and  $\mathbf{U}_{i+1}^L$  defining a local Riemann problem at  $x_{i+\frac{1}{2}}$ .

### Godunov scheme

The simplest reconstruction scheme goes back to Godunov [53]. Continuous data, which is going to be evolved in time, is split into local Riemann problems defining the quantities at the cell interfaces by the requirement, that the data are constant inside each cell (see Fig. 3.4), i.e.

$$\mathbf{U}_i^R = \mathbf{U}_i, \quad (3.3)$$

$$\mathbf{U}_{i+1}^L = \mathbf{U}_{i+1}. \quad (3.4)$$

We use the term Godunov scheme only for the piecewise constant reconstruction, in contrast

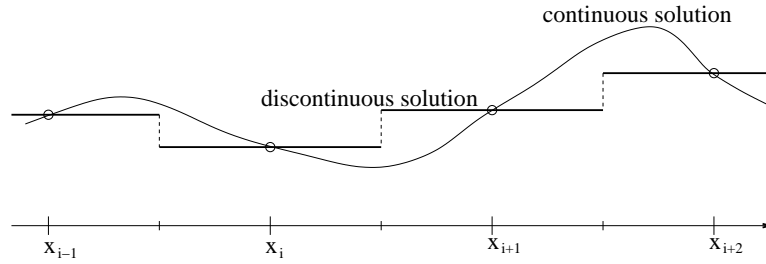


Figure 3.4: Godunov's scheme: At every interface  $x_{i-\frac{1}{2}}$ ,  $x_{i+\frac{1}{2}}$ ,  $x_{i+\frac{3}{2}}$ , a local Riemann problem is set up. The evolution of these data forward in time involves three elementary waves: shocks, rarefaction waves and contact discontinuities.

to the original paper [53], where in addition an exact Riemann solver was presented.

### MUSCL scheme

In contrast to the Godunov scheme, which is only first order accurate (even in smooth, monotonous parts of the flow), the MUSCL scheme (Monotonic Upstream Scheme for Conservation laws) is second order accurate [150]. The quantities at the interface  $\mathbf{U}^R$  and  $\mathbf{U}^L$  are calculated from the requirement

$$\mathbf{U}_i^R = \mathbf{U}_i + \sigma_i(x_{i+\frac{1}{2}} - x_i), \quad (3.5)$$

$$\mathbf{U}_{i+1}^L = \mathbf{U}_{i+1} + \sigma_{i+1}(x_{i+\frac{1}{2}} - x_{i+1}), \quad (3.6)$$

with linear slope

$$\sigma_i = \text{minmod}\left(\frac{\mathbf{U}_i - \mathbf{U}_{i-1}}{\Delta x}, \frac{\mathbf{U}_{i+1} - \mathbf{U}_i}{\Delta x}\right). \quad (3.7)$$

Here, the function “minmod” is defined as

$$\text{minmod}(a, b) = \begin{cases} a & \text{if } |a| \leq |b| \text{ and } ab > 0, \\ b & \text{if } |b| < |a| \text{ and } ab > 0, \\ 0 & \text{if } ab \leq 0. \end{cases} \quad (3.8)$$

As a consequence of the linear reconstruction, the MUSCL reconstruction scheme is second order accurate in smooth, monotonous parts of the flow.

### PPM scheme

The PPM method (piecewise parabolic method) by Colella and Woodward [27] is widely used in hydrodynamical simulations with the Euler equations. We have also implemented it for our general relativistic fluid system. The PPM scheme is third order accurate in smooth, monotonous parts of the flow. We refrain from presenting the details of the PPM scheme here, the interested reader is referred to the original work [27].

### MC scheme

The MC slope limiter (monotonized central-difference slope limiter) by van Leer [149] is second-order accurate in smooth, monotonous parts of the flow. It uses a linear reconstruction scheme with slope

$$\sigma_i = \text{MC}\left(\frac{\mathbf{U}_i - \mathbf{U}_{i-1}}{\Delta x}, \frac{\mathbf{U}_{i+1} - \mathbf{U}_i}{\Delta x}\right), \quad (3.9)$$

where the function “MC” is defined as

$$\text{MC}(a, b) = \begin{cases} \min(|2a|, |2b|, |c|) \times \text{sgn}(a) & \text{if } ab > 0, \\ 0 & \text{if } ab \leq 0, \end{cases} \quad (3.10)$$

with  $c = \frac{a+b}{2}$ .

We have mainly used the MC scheme for our numerical simulations of general relativistic hydrodynamics, for the following reasons: The shock capturing properties and the accuracy of the MC scheme are superior to that of the Godunov and MUSCL schemes, and comparable to that of the PPM scheme (for an independent comparison, see [42]). Comparing it to the PPM scheme, the MC scheme is substantially simpler and thus more efficient. In our numerical simulations, the advantage of the PPM scheme of being third order accurate in contrast to second order accurate for smooth parts of the flow does not pay off, as the metric equations, and hence the global coupled fluid-metric-equations, are only solved to second order accuracy.

### 3.1.2 Approximate Riemann solvers

For the time update of the fluid equations (3.1), which are based on the local Riemann problem with initial data

$$\mathbf{U} = \begin{cases} \mathbf{U}_i^R & \text{for } x_i \leq x < x_{i+\frac{1}{2}}, \\ \mathbf{U}_{i+1}^L & \text{for } x_{i+\frac{1}{2}} \leq x \leq x_{i+1}, \end{cases} \quad (3.11)$$

(see Fig. 3.3) the numerical fluxes have to be defined. These numerical fluxes include numerical viscosity terms needed for the evolution of discontinuous data.

### The HLL solver

The Harten, Lax, van Leer (HLL) solver [69], later improved by Einfeldt [35], defines the numerical viscosity term as a function of the characteristic speeds. It uses a single intermediate state for every local Riemann problem. The numerical flux function in the coordinate direction  $j$  reads

$$\widehat{\mathbf{F}}_{HLL}^j = \frac{a_+^{jR} \mathbf{F}^{jL} - a_-^{jL} \mathbf{F}^{jR} + a_+^{jR} a_-^{jL} (\mathbf{U}^R - \mathbf{U}^L)}{a_+^{jR} - a_-^{jL}}. \quad (3.12)$$

Here  $\mathbf{F}^{jL}$  and  $\mathbf{F}^{jR}$  denote the fluxes evaluated at the right and left state of the interface. Furthermore, we have

$$a_-^{jL} = \min\{0, \lambda_1^{jL}, \dots, \lambda_4^{jL}\}, \quad (3.13)$$

$$a_+^{jR} = \max\{0, \lambda_1^{jR}, \dots, \lambda_4^{jR}\}, \quad (3.14)$$

with characteristic speeds  $\lambda_k^j$ . These characteristic speeds are [117]

$$(\lambda_1^j, \dots, \lambda_4^j) = (\lambda_e^j, \lambda_e^j, \lambda_+^j, \lambda_-^j) \quad (3.15)$$

with

$$\lambda_e^j = \frac{u^j}{u^u}, \quad (3.16)$$

$$\lambda_{\pm}^x = \frac{1}{1 - c_s^2} \left( -\frac{g^{ux}}{(u^u)^2} c_s^2 + \frac{u^x}{u^u} (1 - c_s^2) \pm c_s \sqrt{(c_s \frac{g^{ux}}{(u^u)^2})^2 + (1 - c_s^2) (\frac{g^{xx}}{(u^u)^2} - 2 \frac{g^{ux} u^x}{(u^u)^3})} \right). \quad (3.17)$$

### The Marquina solver

The numerical flux according to Marquina [33] in the coordinate direction  $j$  is defined as

$$\widehat{\mathbf{F}}_{Marq}^j = \frac{1}{2} (\mathbf{F}^{jR} + \mathbf{F}^{jL} - \Delta \mathbf{q}^j) \quad (3.18)$$

where the viscosity term  $\Delta \mathbf{q}^j$  reads

$$\Delta \mathbf{q}^j = \mathbf{R}^{jR} |\mathbf{\Lambda}|_{\max}^j \mathbf{L}^{jR} \mathbf{U}^R - \mathbf{R}^{jL} |\mathbf{\Lambda}|_{\max}^j \mathbf{L}^{jL} \mathbf{U}^L. \quad (3.19)$$

The matrix  $|\mathbf{\Lambda}|_{\max}^j$  involves the characteristic speeds described in the last section and reads explicitly

$$|\mathbf{\Lambda}|_{\max}^j = \text{diag}(\max(\lambda_1^{jR}, \lambda_1^{jL}), \dots, \max(\lambda_4^{jR}, \lambda_4^{jL})). \quad (3.20)$$

$\mathbf{R}^j$  and  $\mathbf{L}^j$  are the matrices of right and left eigenvectors of the Jacobi matrix  $\frac{\partial \mathbf{F}^j}{\partial \mathbf{U}}$ , i.e.

$$\left( \frac{\partial \mathbf{F}^j}{\partial \mathbf{U}} - \lambda^j \mathbf{I} \right) \mathbf{R}^j = 0. \quad (3.21)$$

The right eigenvectors are explicitly given in [117]. The state vector there  $\widehat{\mathbf{U}}$ , however, differs slightly from our definition. It can be transformed by the linear transformation

$$\mathbf{U} = \mathbf{G}\widehat{\mathbf{U}} \quad (3.22)$$

with the matrix  $\mathbf{G}$ , which differs from the unity matrix only in the components

$$(\mathbf{G})_{yu} = g_{yu}, \quad (3.23)$$

$$(\mathbf{G})_{yy} = g_{yy}. \quad (3.24)$$

Explicitly, the matrix of right eigenvectors ( $\mathbf{R} = \mathbf{G}\widehat{\mathbf{R}}$ ) takes in the x-direction the form

$$\mathbf{R}^x = \begin{pmatrix} u^u & u_y u^u & u^u - \frac{\Lambda_{\pm}^x}{u^u} g^{ux} & u^u - \frac{\Lambda_{\pm}^x}{u^u} g^{ux} \\ u^x & u_y u^x & u^x + \frac{\Lambda_{\pm}^x}{(u^u)^2} (u^x g^{ux} - u^u g^{xx}) & u^x + \frac{\Lambda_{\pm}^x}{(u^u)^2} (u^x g^{ux} - u^u g^{xx}) \\ u_y & u_y u_y + g_{yy} & u_y & u_y \\ \frac{1}{\alpha} & u_y (\frac{1}{h} - \frac{1}{\alpha}) & \frac{1}{h} & \frac{1}{h} \end{pmatrix} \quad (3.25)$$

and in the y-direction the form

$$\mathbf{R}^y = \begin{pmatrix} u^u & u_x u^u & u^u & u^u \\ u^x & u_x u^x + 1 & u^x + \frac{\Lambda_{\pm}^y}{(u^u)^2} (u^y g^{ux} - u^u g^{xy}) & u^x + \frac{\Lambda_{\pm}^y}{(u^u)^2} (u^y g^{ux} - u^u g^{xy}) \\ u_y & u_x u_y & u_y - \frac{\Lambda_{\pm}^y}{u^u} & u_y - \frac{\Lambda_{\pm}^y}{u^u} \\ \frac{1}{\alpha} & u_x (\frac{1}{h} - \frac{1}{\alpha}) & \frac{1}{h} & \frac{1}{h} \end{pmatrix}. \quad (3.26)$$

Following the work of [117], we have used the notation

$$\alpha = 1 + \epsilon - \rho \frac{\frac{\partial p}{\partial \rho} |_{\epsilon}}{\frac{\partial p}{\partial \epsilon} |_{\rho}} \quad (3.27)$$

and

$$\Lambda_{\pm}^x = \frac{c_s^2}{(\frac{u^x}{u^u} - \lambda_{\pm})(1 - c_s^2) - c_s^2 \frac{g^{ux}}{(u^u)^2}}, \quad (3.28)$$

$$\Lambda_{\pm}^y = \frac{c_s^2}{(\frac{u^x}{u^u} - \lambda_{\pm})(1 - c_s^2)}. \quad (3.29)$$

From the matrix of right eigenvectors, we calculate the matrix of left eigenvectors by matrix inversion using the linear algebra package of MAPLE.

### 3.1.3 The recovery of the primitive variables

After every time step, we have to calculate the primitive variables  $w = (\rho, u^x, u_y, \epsilon)$  from the conserved quantities and the metric variables. The basic concepts for this recovery were presented in [117]. Defining the tensors  $J^a = \rho u^a$  and  $S^{ab} = g_{cd} T^{ac} T^{bd}$ , a short calculation using the normalization condition of the four velocity results in

$$S^{uu} = \left(\frac{p}{\rho} - 1 - \epsilon\right) \left(\frac{p}{\rho} + 1 + \epsilon\right) (J^u)^2 + p^2 g^{uu}. \quad (3.30)$$

Assuming  $p = \rho E(h)$  and using the definition of stress energy  $T^{uu}$ , a nonlinear equation for the enthalpy  $h$  can be derived,

$$(T^{uu})^2 S^{uu} - h(2E(h) - h)(J^u)^2 (T^{uu})^2 - (S^{uu} - h(E(h) - h)(J^u)^2) g^{uu} = 0. \quad (3.31)$$

The recovery simplifies in our null coordinate system, where  $g^{uu} = 0$ . Note, that  $J^u$  and  $T^{uu}$  are, up to the square root of the metric determinant, conserved quantities.

### The recovery for the ideal fluid EoS

For the ideal fluid EoS (2.50) we have

$$E(h) = \frac{\Gamma - 1}{\Gamma} (h - 1). \quad (3.32)$$

For this choice and our null coordinate system  $g^{uu} = 0$ , Eq. (3.31) simplifies to a quadratic equation in  $h$ ,

$$\frac{\Gamma - 2}{\Gamma} h^2 - 2 \frac{\Gamma - 1}{\Gamma} h = \frac{S^{uu}}{(J^u)^2}, \quad (3.33)$$

and can thus be solved analytically. Once having the enthalpy at hand, it is easy to solve for the remaining primitive quantities. We solve for the primitive variables  $\epsilon$ ,  $\rho$ ,  $u^x$  and  $u_y$  and then use the normalization condition to determine  $u^u$ .

### The recovery for the polytropic EoS

As we have shown in Sec. 2.2.2, the 4 conserved quantities are no longer independent when imposing the polytropic EoS (2.52) and the ideal fluid EoS (2.50). As a consequence the general procedure for the recovery cannot be used. We choose the conserved quantities  $J^u$ ,  $T^{uu}$ ,  $T_y^u$  as dynamic fields, from which we recover the primitive variables. For the polytropic EoS, the enthalpy is  $h = 1 + \kappa \frac{\Gamma}{\Gamma - 1} \rho^{\Gamma - 1}$ . We can thus define the implicit equation to recover the rest mass density  $\rho$ ,

$$f_{\text{imp}}(\rho) := 1 + \kappa \frac{\Gamma}{\Gamma - 1} \rho^{\Gamma - 1} - \frac{T^{uu}}{(J^u)^2} \rho = 0. \quad (3.34)$$

In the special case  $\Gamma = 2$ , this equation can be solved analytically. For all other values of  $\Gamma$  we solve it with the help of the Newton-Raphson procedure. With an initial guess  $\rho^*$  (where we use the value of the rest mass density on the previous time slice), we get an improved result for the rest mass density by

$$\rho = \rho^* - \frac{f_{\text{imp}}(\rho^*)}{f'_{\text{imp}}(\rho^*)}. \quad (3.35)$$

### The recovery for the hybrid EoS

For the hybrid EoS, the recovery algorithm is slightly more complicated. Let  $F(\rho, \epsilon) = \frac{p}{\rho}$ . From Eqs. (3.30), (2.60) and the definition of the specific enthalpy  $h$  we obtain the 3 equations for the 3 unknowns  $F$ ,  $\rho$  and  $\epsilon$

$$F(\rho, \epsilon) = \sqrt{L + (1 + \epsilon)^2}, \quad (3.36)$$

$$F(\rho, \epsilon) = (\Gamma_{th} - 1)\epsilon + G(\rho), \quad (3.37)$$

$$\rho = H(1 + \epsilon + F(\rho, \epsilon)). \quad (3.38)$$

In these equations we made use of the abbreviations

$$L = \frac{S^{uu}}{(J^u)^2}, \quad (3.39)$$

$$G(\rho) = \kappa \left( 1 - \frac{\Gamma_{th} - 1}{\Gamma - 1} \right) \rho^{\Gamma-1} - \frac{(\Gamma_{th} - 1)(\Gamma - \Gamma_1)}{(\Gamma_2 - 1)(\Gamma_1 - 1)} \kappa \rho_n^{\Gamma-1}, \quad (3.40)$$

$$H = \frac{(J^u)^2}{T^{uu}}. \quad (3.41)$$

From Eqs. (3.36)-(3.38) we deduce a single implicit equation for the rest mass density  $\rho$

$$f_{\text{imp}}(\rho) := \left( \frac{\rho}{H} \right)^2 - 2 \frac{\rho}{H} (1 + \epsilon) - L = 0, \quad (3.42)$$

where we consider the internal energy as function of  $\rho$

$$\epsilon = \frac{1}{\Gamma_{th}} \left( \frac{\rho}{H} - (1 + G(\rho)) \right). \quad (3.43)$$

Again, we solve Eq. (3.42) with a Newton-Raphson method.

## 3.2 Implementation of the metric equations

Our numerical implementation of the metric equations relies on experience of solving the vacuum field equations of general relativity in the characteristic approach [163], and in particular on [60]. For the presentation here, we focus the discussion on the necessary adaptations and generalizations.

### 3.2.1 Solving the wave equation

For the time update of the metric field  $\hat{\gamma}$ , we have implemented two different algorithms to solve the wave equation (2.24). The first algorithm, which is used almost everywhere in this work, is the so-called *parallelogram algorithm* [60]. The second algorithm is due to Lehner [89]. In this second approach, dissipation can be included. Hence, we will call it *dissipative algorithm*.

#### The parallelogram algorithm

In the parallelogram algorithm, the time update for the metric field  $\hat{\gamma}$  is based on a parallelogram consisting of ingoing and outgoing characteristics [64, 60, 162]. We closely follow the implementation of [60] to which the reader is referred for more details. In contrast to this work, however, the wave equation is formulated for a single quantity in the whole numerical domain, which ensures regularity at future null infinity  $\mathcal{J}^+$ , i.e. in the limit  $r \rightarrow \infty$ . This regularization is accomplished by writing the parallelogram identity in terms of the quantity

$$\Phi = \hat{\psi} f, \quad (3.44)$$

where the quantities on the right hand side were defined in Eq. (2.23) and Eq. (2.13). Explicitly, for a parallelogram  $\Sigma$  with left upper corner  $P$ , right upper corner  $Q$ , left lower corner  $R$  and right lower corner  $S$  (see Fig. 3.5) the algorithm reduces to

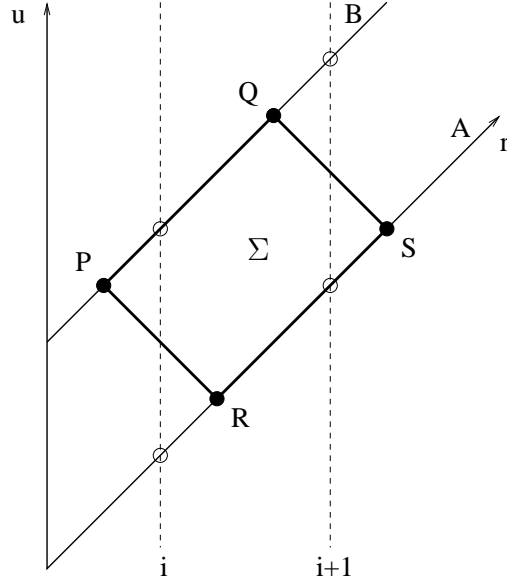


Figure 3.5: Parallelogram  $PQRS$  consisting of ingoing and outgoing light cones. We have displayed the outgoing light cones at two different coordinate values  $u$ ,  $A$  and  $B$ , foliating our spacetime. For simplicity, all null lines have angles  $45^\circ$ . In addition to the parallelogram we have marked radial grid points at  $i$  and  $i + 1$ .

$$\begin{aligned} \Phi_Q &= \frac{1}{4} \Delta u r_Q f|_Q \hat{H}_c + \frac{f|_Q}{f|_P} (\Phi_P - \frac{1}{4} \Delta u r_P f|_P \hat{H}_c) \\ &+ \frac{f|_Q}{f|_S} (\Phi_S + \frac{1}{4} \Delta u r_S f|_S \hat{H}_c) - \frac{f|_Q}{f|_R} (\Phi_R + \frac{1}{4} \Delta u r_R f|_R \hat{H}_c). \end{aligned} \quad (3.45)$$

Using suitable interpolation techniques one obtains the field  $\Phi_{i+1}$  at the new time level to second order accuracy. In the above equation  $\hat{H}_c$  denotes the expression defined in Eq. (2.27) approximated to second order accuracy at the center of the parallelogram. The regularity of Eq. (3.45) can be easily seen for our compactified grids

$$r(x) = a \frac{x}{1 - x^b}, \quad b \geq 1, \quad (3.46)$$

as

$$rf = \sqrt{a} \frac{x}{\sqrt{1 + (b-1)x^b}}. \quad (3.47)$$

Moreover, as  $\lim_{r \rightarrow \infty} f = 0$ , regularity of the quotient  $\frac{f|_Q}{f|_S}$  has to be established (note that  $f|_P$  and  $f|_R$  are always finite). To this aim, we observe that

$$\frac{f|_Q}{f|_S} = \frac{1 - x_Q}{1 - x_S} \frac{\sum_{i=0}^{b-1} x_Q^i}{\sum_{j=0}^{b-1} x_S^j} \frac{\sqrt{1 + (b-1)x_S^b}}{\sqrt{1 + (b-1)x_Q^b}}. \quad (3.48)$$



All the terms on the right hand side of Eq. (3.48) are explicitly regular for  $x \rightarrow 1$  ( $r \rightarrow \infty$ ), except for the first factor which is regular according to the discussion in [60]. Similar results hold for the grid function

$$r(x) = a \tan\left(\frac{\pi}{2}x\right). \quad (3.49)$$

### The dissipative algorithm

Starting with the wave equation (2.24) in the form

$$2\hat{\psi}_{,ux} - \left(\frac{V}{r}f^2\right)_{,x}\hat{\psi}_{,x} - \left(\frac{V}{r}f^2\right)\hat{\psi}_{,xx} = f^{-2}\hat{H} \quad (3.50)$$

we discretize it with the stencils proposed in [89]. Evaluating the derivatives at the time interface  $n + \frac{1}{2}$  and radial interface  $i - \frac{1}{2}$  to second order accuracy, we obtain

$$\hat{\psi}_{,ux}\Big|_{i-\frac{1}{2}}^{n+\frac{1}{2}} = \frac{\hat{\psi}_i^{n+1} - \hat{\psi}_{i-1}^{n+1} - (1-\hat{\epsilon})(\hat{\psi}_i^n - \hat{\psi}_{i-1}^n) - \frac{1}{3}\hat{\epsilon}(\hat{\psi}_{i+1}^n - \hat{\psi}_{i-2}^n)}{\Delta u \Delta x}, \quad (3.51)$$

$$\hat{\psi}_{,x}\Big|_{i-\frac{1}{2}}^{n+\frac{1}{2}} = \frac{\hat{\psi}_i^{n+1} - \hat{\psi}_{i-1}^{n+1} + \hat{\psi}_i^n - \hat{\psi}_{i-1}^n}{2\Delta x}, \quad (3.52)$$

$$\hat{\psi}_{,xx}\Big|_{i-\frac{1}{2}}^{n+\frac{1}{2}} = \frac{\hat{\psi}_i^{n+1} - 2\hat{\psi}_{i-1}^{n+1} + \hat{\psi}_{i-2}^{n+1} + \hat{\psi}_{i+1}^n - 2\hat{\psi}_i^n + \hat{\psi}_{i-1}^n}{2(\Delta x)^2}. \quad (3.53)$$

We have included a parameter  $\hat{\epsilon}$  describing the numerical dissipation. For  $\hat{\epsilon} = 0$ , the numerical dissipation is switched off. As we have not taken special care to regularize the wave equation here, we cannot use the described approach in the neighborhood of future null infinity. Instead, we use the parallelogram algorithm at  $\mathcal{I}^+$ .

### 3.2.2 Solving the hypersurface equations

We discretize the hypersurface equation (2.19) (and similarly Eq. (2.21)) as

$$\beta_{i,j} = \beta_{i-1,j} + \mathcal{H}_{\beta_{i-1/2,j}}\Delta x, \quad (3.54)$$

where  $\mathcal{H}_\beta$  denotes the right hand side of Eq. (2.19). To solve the hypersurface equation (2.20), we discretize the alternative equation

$$\begin{aligned} & 2xf\left(r^4 f^4 \hat{U}_x\right)_{,x^4} + r^2 f^2 \left(-\frac{1}{2}(f^2)_{,x} \frac{r^2}{x^2} f^2\right)^{\frac{1}{2}} \\ & - \frac{r^2}{x^2} (f^2)^{\frac{3}{2}} (\beta_{,x} - \hat{\gamma}_{,x}\bar{y}) \hat{U}_{,x} = \frac{r^2}{x^2} f^3 e^{2(\beta - \bar{y}\hat{\gamma})} \mathcal{H}_U, \end{aligned} \quad (3.55)$$

where the right hand side of Eq. (2.20) has been denoted by  $2r^2\mathcal{H}_U$ . The derivative  $\partial/\partial x^4 = \frac{1}{4x^3}\partial/\partial x$  was introduced to ensure regularity at the origin.

### 3.2.3 The Courant condition

In order to obtain stability in our explicit algorithms when solving the fluid and metric equations they have to fulfill the Courant-Friedrichs-Lewy condition - the numerical domain of dependence must include the analytical domain of dependence. This condition limits the maximal time step allowed in each time update. Calculating the characteristic speeds for the fluid system, the fluid update sets a limit on the time step as

$$\Delta u \leq \min(c_1 \Delta x, c_2 \Delta y), \quad (3.56)$$

where  $c_1$  and  $c_2$  are constants and the minimum is calculated for the entire fluid grid. For the metric update, it can be shown [115] that the evolution near the origin sets the stricter theoretical limit

$$\Delta u = c_3 \Delta r (\Delta y)^2, \quad (3.57)$$

with  $c_3 = 0.5$ . In numerical experiments we found, however, that with our coupled code  $c_3 \approx 10$ , in good agreement with the result  $c_3 = 8$  reported in [115]. With this result the time step restriction from Eq. (3.57) is not much stronger than the time step restriction from Eq. (3.56), at least for the angular resolutions we can afford. As a consequence, it is not necessary to implement implicit methods for the metric update.

### 3.2.4 The origin treatment

As for the vacuum equations the origin of coordinates, where we assume that the coordinate system is a local Fermi system<sup>1</sup>, needs special care. We establish the regularity conditions by performing a power-series expansion of the metric and fluid variables at the origin. The main change in the falloff behavior of the metric variables due to the presence of the fluid is in  $\beta$ . We impose a falloff behavior of the metric field  $\hat{\gamma}$  as

$$\hat{\gamma} = a r^2 + b r^3, \quad (3.58)$$

where  $a$  and  $b$  are constants. At the origin the radial dependence of  $\beta$  is  $\beta = O(r^2)$ , instead of  $\beta = O(r^4)$  for the vacuum case (from Eq. (2.19)). To ensure regularity of the fluid at the origin, we have to impose [75]

$$u_r = D + Ey + O(r), \quad (3.59)$$

$$u_y = Er + O(r^2), \quad (3.60)$$

where  $D$  and  $E$  fulfill  $-D^2 + E^2 = -1$ . With the definitions (the leading terms of the power-series expansion can be extracted from the hypersurface equations)

$$\beta = \frac{r^2}{8} \kappa \rho h (D + Ey)^2 + F(y) r^3, \quad (3.61)$$

$$\hat{U} = 4y(ar + \frac{3}{5}br^2) + \frac{1}{2} \kappa \rho h (D + Ey) Er + C(y) r^2, \quad (3.62)$$

$$\kappa \rho h u_y u_y = \kappa \rho h E^2 r^2 + G(y) r^3, \quad (3.63)$$

<sup>1</sup>In a Fermi normal coordinate system, the metric takes Minkowski form along the entire world line (e.g.  $r = 0$ ), see [103].

the quadratic terms in  $r$  in the wave equation reduce to an equation for  $a$

$$a_{,u} = \frac{6}{5}b - \frac{1}{3}C_{,y} + \frac{1}{6}F_{,yy} + \frac{1}{12}G. \quad (3.64)$$

(In the absence of matter this reduces to  $a_{,u} = \frac{6}{5}b$ , see [60]). We extract  $a$ ,  $b$ ,  $C$ ,  $F$  and  $G$  at the old time slice and then solve Eq. (3.64) to obtain  $a$  at the new time slice. Inserting this value into the leading order in  $r$  of Eq. (3.58) and Eq. (3.62), we calculate  $\hat{\gamma}$  and  $\hat{U}$  at the two first grid points, which then allows us to start the marching algorithms described above for the metric update.

### 3.3 The fluid metric coupling

In the following, we describe the order of the time update from light cone  $A$  at time  $u$  to light cone  $B$  at time  $u + \Delta u$ , as shown in Fig. 3.5. Let us assume that we know the primitive and conserved fluid variables, and the metric quantities  $\hat{\gamma}$ ,  $\beta$ ,  $\hat{U}$  and  $S$  on the light cone  $A$ . In a first step we globally determine the conserved fluid variables on  $B$ . To this aim, we determine the fluxes and sources of the fluid system on  $A$  which allows us to obtain the conserved fluid variables on  $B$  according to Eq. (3.1). For the metric update, in contrast, we march from the origin to the exterior of the light cone  $B$ , solving the wave and hypersurface equations. Having previously obtained the variables up to grid point  $i$  (either from the specific boundary treatment at the origin or during the marching process), we first determine  $\hat{\gamma}$  at grid point  $i + 1$ . In a second step we solve for  $\beta$ ,  $\hat{U}$  and  $S$  at  $i + 1$  in that particular order, recovering the primitive variables with the metric thus obtained. Since the hypersurface integration for the metric depends on the primitive variables at the grid point to be determined, we iterate the hypersurface and recovery algorithm until convergence at each radial location.

In order to obtain a second order accurate evolution in time, we perform the time update with the second order Runge-Kutta algorithm of Shu and Osher [137].

### 3.4 Gravitational wave extraction

The theory of gravitational waves was already developed in detail in Sec. 2.3. The numerical integration of the relevant equations closely follows the description there.

#### 3.4.1 Numerical extraction of the Bondi news

In our numerical implementation we use a standard second order integration for the double integrals in Eq. (2.83) and we determine the conformal factor according to Eq. (2.81) afterwards. Moreover, to solve the hypersurface equations for the auxiliary variables  $\tau$  and  $\mu$  defined in Eqs. (2.68)-(2.69) ( $\mu$  is needed for the Bondi mass, Eq. (2.70)), we also use a second order discretization. By simply reading off the metric values at  $\mathcal{J}^+$ , it is finally possible to determine the Bondi mass and news.

#### 3.4.2 Numerical extraction of approximate gravitational waves

If we introduce our angular coordinate  $y = -\cos\theta$  in the numerical calculation of the multipole moments, i.e. in Eqs. (2.88), (2.92) and in Eqs. (2.100), (2.102), we could simply make use of

a standard second order discretization scheme for the numerical integration. However, in our numerical analysis, we found much faster convergence, if we identify in the integrals over the angle the Legendre polynomials

$$P^{(2)}(y) = \frac{1}{2}(3y^2 - 1), \quad (3.65)$$

$$P^{(4)}(y) = \frac{5}{8}(7y^4 - 6y^2 + \frac{3}{5}) \quad (3.66)$$

and integrate the corresponding terms separately. Making use of a relation between Legendre polynomials of degree  $l$ ,  $l + 1$  and  $l - 1$ ,

$$P^{(l)}(y) = \frac{1}{2l + 1} \left( \frac{dP^{(l+1)}(y)}{dy} - \frac{dP^{(l-1)}(y)}{dy} \right), \quad (3.67)$$

we discretize the angular integration as

$$\int_{-1}^1 dy f(r, y) P^{(l)}(y) \approx \sum_{j=-N_y}^{j=N_y-1} f(r, y_{j+\frac{1}{2}}) \frac{1}{2l + 1} \left( P^{(l+1)}(y) \Big|_{y_j}^{y_{j+1}} - P^{(l-1)}(y) \Big|_{y_j}^{y_{j+1}} \right), \quad (3.68)$$

where  $y_{-N_y} = -1$  and  $y_{N_y} = 1$ .

# Chapter 4

## Code tests

We have performed various tests aimed at checking the implementation and the accuracy of the numerical code. To the best of our knowledge we do not know of any regular exact (analytic) solution of the Einstein equations in axisymmetry with a non-vanishing perfect fluid matter field. Hence, it is even more important to check the different regimes of our implementation. Moreover, to test the overall implementation of the code we examine the global conservation properties which can be rigorously established due to the compactification of spacetime.

### 4.1 Tests for the metric solver

Our numerical code is based on the vacuum code of [60]. However, as we have generalized the coordinate system, we used two vacuum tests to establish the correctness of our metric solver. Going to the linearized regime around flat space time, one can find exact (linear) solutions of the metric equations. These are used as a testbed for our nonlinear code, when we study small amplitude gravitational waves in Sec. 4.1.1. In addition, there is an exact solution for the full vacuum equations which was already used to check the vacuum code of [60]. We use it here again for our generalized implementation.

#### 4.1.1 Linearized gravitational waves

Linearizing the vacuum Einstein equations around Minkowski space, global analytic multipole solutions of the field equations can be found [115]. For example, the quadrupole solution reads explicitly

$$\hat{\gamma} = 8A \left( \frac{r}{r+1} \right)^2 \frac{u \frac{r}{r+1} - u - 1}{(u+1)^4 \left( u \frac{r}{r+1} - \frac{r}{r+1} - u - 1 \right)^3}, \quad (4.1)$$

where  $A$  is the free amplitude of the linearized equations. As we are going to use this solution as a testbed for our fully nonlinear metric solver, we have to ensure that  $A$  is small. We choose  $A = -10^{-4}$ , for which we can reproduce the linear solution with our code (see Fig. 4.1). Similar results hold for higher multipoles.

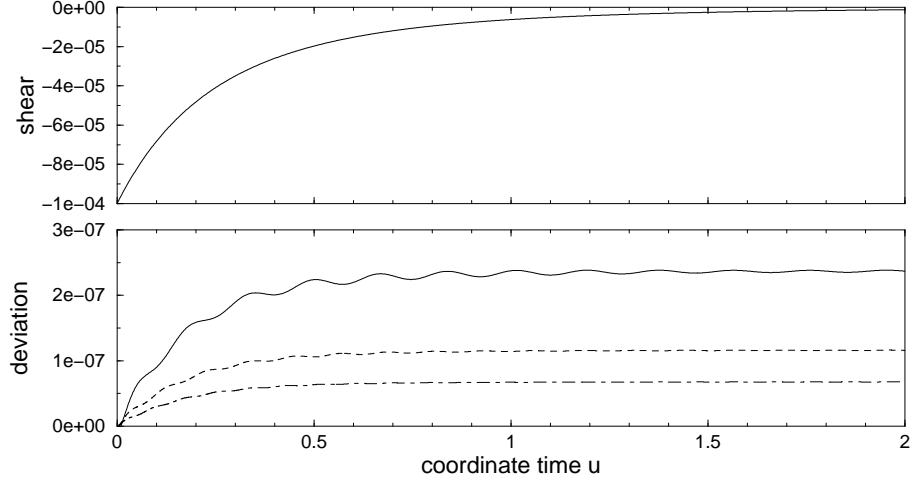


Figure 4.1: For a low amplitude gravitational wave, we reproduce the linear wave solution with our fully nonlinear evolution to second order accuracy. Upper Panel: Time evolution of the gravitational wave shear  $\hat{\gamma}$  at future null infinity ( $x = 1$ ) for a  $l = 2$  linearized wave. Lower Panel: Difference of the gravitational wave shear  $\hat{\gamma}$  taken from our numerical simulations and the exact linear result. The solid (dashed and dotted-dashed) line corresponds to a resolution  $(N_x, N_y) = (100, 8)$  ( $(N_x, N_y) = (150, 12)$  and  $(N_x, N_y) = (200, 16)$ ).

#### 4.1.2 SIMPLE

Following the work of [60] the Bondi metric (2.5) with metric functions

$$e^\gamma = \frac{1}{2}(1 + \Sigma), \quad (4.2)$$

$$e^{2\beta} = \frac{(1 + \Sigma)^2}{4\Sigma}, \quad (4.3)$$

$$U = -\frac{a^2 g \cos \theta}{\Sigma}, \quad (4.4)$$

$$V = \frac{r}{\Sigma}(2a^2 g^2 - a^2 r^2 + 1), \quad (4.5)$$

is a solution of the vacuum field equations for

$$\Sigma = \sqrt{1 + a^2 g^2}, \quad (4.6)$$

$$g = r \sin \theta, \quad (4.7)$$

where  $a$  is a constant. In the following, we choose  $a = 0.1$ . Being cylindrically symmetric, the above solution, which is called “SIMPLE”, is clearly not asymptotically flat. Hence, the solution cannot be used with a compactified grid. Instead, we impose boundary conditions at a finite radius  $r$ , thus restricting the solution to a compact region which includes the vertex at

$r = 0$ . We define a suitable L2-norm to measure deviations from the exact solution by

$$\text{norm}(r) = \left( \int_{-1}^1 \sum_{k=1}^4 (f_k(r, y) - f_k^e(r, y))^2 dy \right)^{\frac{1}{2}}. \quad (4.8)$$

Here, the summation includes the four metric fields  $f_k \in (\beta, \gamma, S, U)$ ,  $f_k^e$  denotes the exact solution. Using this norm we have checked that our metric solver is second order convergent (see Fig. 4.2).

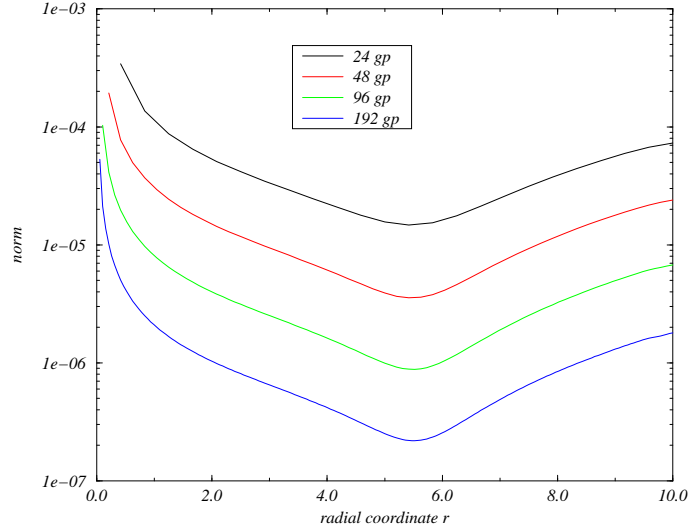


Figure 4.2: Convergence test for the exact vacuum solution SIMPLE. Plotted is a local norm measuring the deviation from the analytic solution (see text for more details) as a function of the radial coordinate  $r$  at time  $u = 1$  for different resolutions. In the diagram, we have indicated the number of radial zones  $N_x$  used, the number of angular zones was chosen as  $N_y = \frac{1}{3}N_x$ . The results show that our metric solver is second order convergent.

## 4.2 Tests concerning relativistic stars

In this section we describe tests of our code in dealing with relativistic stars. In the first subsection, we consider spherically symmetric equilibrium stars. We mention, that the code's ability to maintain spherical symmetry for spherically symmetric initial data is a first important test. The following subsection describes the conservation properties of a strongly perturbed, aspherical relativistic star.

### 4.2.1 Equilibrium relativistic stars

In order to obtain initial data for equilibrium relativistic stars, we solve the TOV equations (2.62)-(2.63) for a polytropic EoS (2.52).

### Numerical stability of stable relativistic stars

We experimented with different polytropic indices in the polytropic EoS. In what we describe here, we restrict ourselves to a particular model, for which the equilibrium properties are: an adiabatic exponent  $\Gamma = 2$  (i.e. a polytropic index  $n = 1$ ), a polytropic constant  $\kappa = 100$  and a central density  $\rho_c = 1.28 \times 10^{-3}$  (in our units  $c = G = M_\odot = 1$ ). The equilibrium model has a total mass  $M = 1.4M_\odot$ . The time light needs to travel across this neutron star corresponds to about 17 units in our coordinate time  $u$ . With complete initial data at hand we evolve stable equilibrium configurations in time. Both, for finite grids which only cover the star, as well as for compactified grids, where we cover the star and its entire exterior spacetime, the code is able to maintain the initial equilibrium profiles of the star, for times much longer than the light-crossing time. As a typical example Fig 4.3 shows the density profile of the neutron star at various integration times up to a final evolution time  $u = 10000$  for a small resolution run with 50 radial zones. Even though this corresponds to a very long-term, fully general relativistic hydrodynamic evolution, the density profile almost does not change, the equilibrium of the star being maintained to very good precision. The upper line corresponds to the initial model, the lowest line to the density profile at the time  $u = 10000$ , which corresponds to roughly 590 light-crossing times. Due to the discretization error, the star is excited to oscillate in its radial

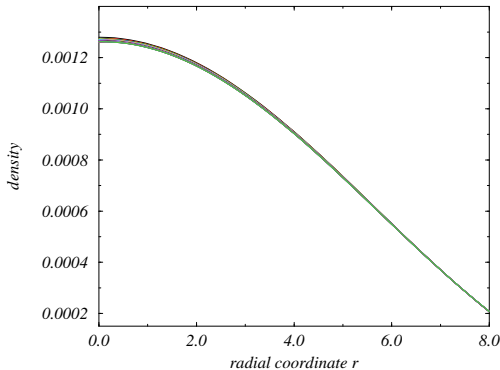


Figure 4.3: Density profile of the neutron star at the initial and subsequent times. The final time corresponds to  $u = 10000$  (roughly 590 light-crossing times). The equilibrium model is maintained to a very good precision after such very long integration times.

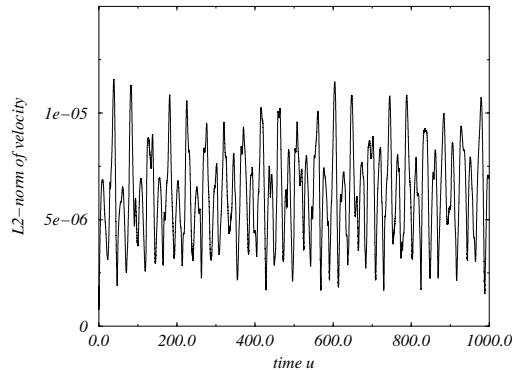


Figure 4.4: Radial velocity of the star, averaged over the radial coordinate, as a function of time. In order to resolve the oscillation pattern in the plot, the final evolution time is  $u = 1000$ , which corresponds to about 59 light-crossing times.

modes of pulsations. The amplitude of these radial oscillations does not increase during the evolution, which reflects the long-term stability of our numerical implementation (see Fig. 4.4). For similar evolutions, the extraction of the frequency of the pulsations will be discussed in Chapter 5.

Deviations from equilibrium converge to zero with increasing resolution with a second order



convergence rate. Figure 4.5 shows a suitable norm of all variables,

$$\text{norm}(r) = \left( \int_{-1}^1 \sum_{k=1}^8 (f_k(r, y) - f_k^e(r, y))^2 dy \right)^{\frac{1}{2}}, \quad (4.9)$$

as a function of the radial coordinate, which measures the deviation from the initial solution for different grid resolutions. The summation includes the field  $f_k \in (\beta, \gamma, S, U, \rho, \epsilon, u^x, u_y)$ .

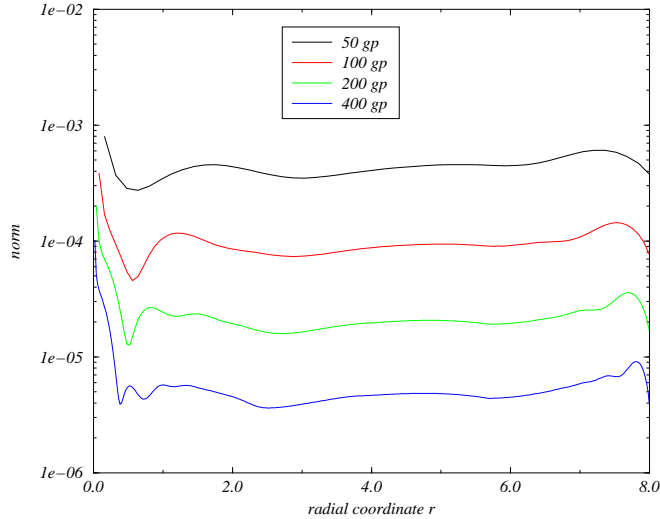


Figure 4.5: Convergence test for the Tolmann-Oppenheimer-Volkoff solution. Plotted is a suitable norm of all variables, which measures the deviation from equilibrium, for the indicated number of radial grid points (gp), after about two light-crossing times. To good approximation the solution is second order convergent.

### Migration of an unstable relativistic star

Following [42] we have checked the code on the dynamical evolution of an unstable spherical star. In such a model the sign of the discretization error of the numerical scheme controls the fate of the evolution: the star may either expand or collapse. In our code this sign is such that the unstable star “migrates” to the stable branch of the sequence of equilibrium models. In such a situation, the rest-mass of the star has to be conserved throughout the evolution. Despite being an academic problem this simulation represents an important test of the accuracy and self-consistency of the code in a highly dynamical situation.

As in [42] we have constructed a  $\Gamma = 2$ ,  $\kappa = 100$  polytropic star with mass  $M = 1.447 M_\odot$  and central rest-mass density  $\rho_c = 8.0 \times 10^{-3}$  (in units  $G = c = M_\odot = 1$ ). With this value of the central density, the equilibrium model is unstable with respect to radial oscillations, in contrast to the model we used above. As the radius of the star strongly increases during the evolution, we surround the star by a low density atmosphere ( $\rho_{atm} \approx 10^{-6} \rho_c$ ). In order to avoid numerical problems in these zones we reset the fluid variables to their original atmosphere

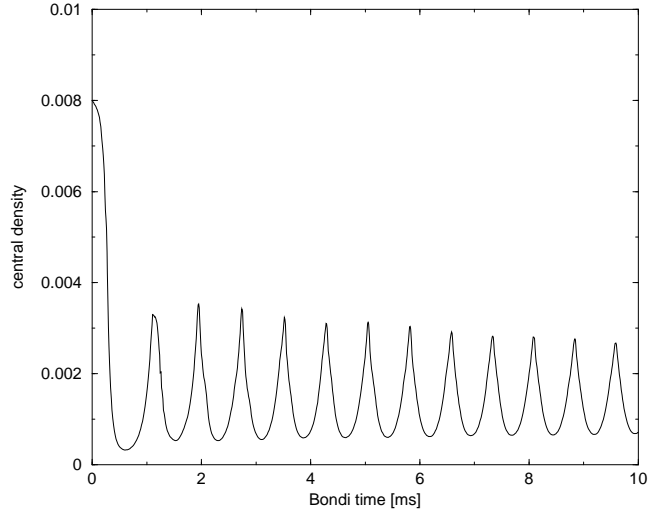


Figure 4.6: Evolution of the central rest-mass density during the migration of an unstable relativistic star ( $\Gamma = 2, \kappa = 100, M = 1.447M_{\odot}, \rho_c = 8.0 \times 10^{-3}; G = c = M_{\odot} = 1$ ) to a stable model with the same rest-mass. The central density of the (final) stable configuration is  $\rho_c = 1.35 \times 10^{-3}$ . The evolution shows the expected behavior. Since we use a polytropic EoS, the amplitude of the oscillations is essentially undamped for the evolution times shown.

values once they have fallen below a threshold value (see [43] for more details). This artificial resetting enables the star to expand and to contract. Despite the use of an atmosphere the energy conservation properties are well satisfied.

Fig. 4.6 shows the evolution of the central density up to a final time of  $u_B = 10$  ms. On a very short dynamical timescale the star rapidly expands and its central rest-mass density drops well below its initial value. It finally reaches a value of less than  $\rho_c = 1.35 \times 10^{-3}$ , the central rest-mass density of the stable model of the same rest-mass. During the rapid decrease of the central density, the star acquires a large radial momentum. The star then enters a phase of large amplitude radial oscillations around the stable equilibrium model. As Fig. 4.6 shows the code is able to accurately recover (asymptotically) the expected values of the stable model. Furthermore, the displayed evolution is completely similar to that obtained with an independent fully three-dimensional code in Cartesian coordinates [42]. The evolution shown in Fig. 4.6 allows to study large amplitude oscillations of relativistic stars.

## 4.2.2 Global energy conservation

In this section we focus on a global energy conservation test. Starting with the equilibrium model of a neutron star with adiabatic exponent  $\Gamma = 2$ , polytropic constant  $\kappa = 100$  and central density  $\rho_c = 1.28 \times 10^{-3}$ , we use a strong gravitational wave to perturb the star,

$$\hat{\gamma} = 0.2 e^{-3(r-4)^2} y. \quad (4.10)$$

Prescribing such a large gravitational wave amplitude we do not aim to model an astrophysical situation, but we choose it to test our numerical implementation in the nonlinear regime.

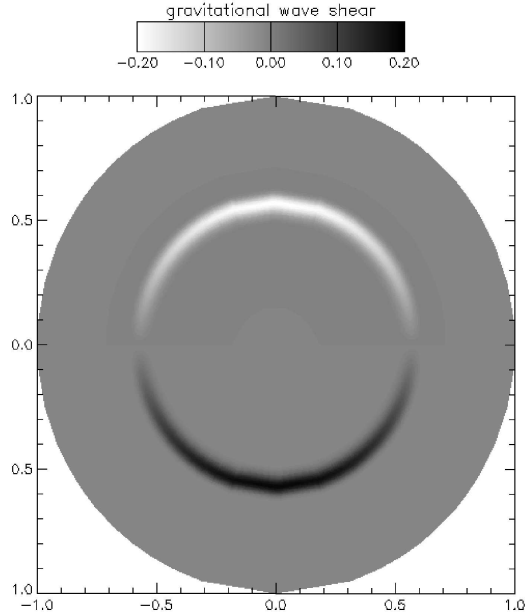


Figure 4.7: Contour plot of the initial gravitational wave shear  $\hat{\gamma}$ , Eq. (4.10). The axes labels denote the value of the radial coordinate  $x$  along the equator (horizontal axis) and the symmetry axis (vertical axis), and they run from the origin of the coordinate system at  $x = 0$  to future null infinity  $\mathcal{J}^+$  at  $x = 1$ . The numerical domain comprises the half circle to the right of the vertical line at  $x = 0$  (the symmetry axis), the left half is obtained from axisymmetry. The gravitational wave shear perturbation is located in a small ring at radius  $r \approx 4$ .

Fig. 4.7 shows a contour plot of the initial gravitational wave shear. In what follows we use a radial grid with  $r = 3\frac{x}{1-x}$ .

Fig. 4.8 shows the deviation from global energy conservation (see Eq. (2.79)) as a function of the grid resolution (circles) and the total energy radiated away in gravitational waves. The deviations from exact energy conservation converge to zero, as expected, which represents a very severe global test for our numerical implementation.

There are two additional consistency conditions we can use to check the code, which relate the metric quantities at  $\mathcal{J}^+$ . These are [115]

$$S - U_{,\theta} - U \cot \theta = 0, \quad (4.11)$$

$$\gamma_{,u} + \frac{1}{2}e^{-2\gamma} \sin \theta \left( e^{2\gamma} \frac{U}{\sin \theta} \right)_{,\theta} = 0. \quad (4.12)$$

Our code reproduces these conditions, the errors converging to zero with a convergence rate of 1. Fig. 4.9 shows the deviation from zero for the first condition, thus checking the leading term in the falloff behavior of the quantity  $S$  at  $\mathcal{J}^+$ .

The obtained first-order convergence rate can be explained by the use of a *total variation diminishing* high-resolution shock-capturing scheme for the fluid evolution, which, although it is second-order accurate in smooth, monotonous parts of the flow, reduces to first-order at local

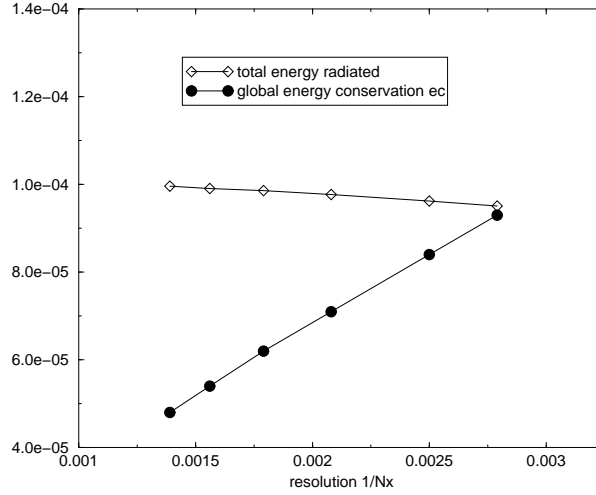


Figure 4.8: Global energy conservation test for a neutron star and a strong gravitational wave. Plotted are the deviation from global energy conservation  $ec$  (dark circles, see Eq. (2.79)) and the total energy emitted by gravitational waves as a function of the grid resolution. The final integration time is  $u_B = 2 \times 10^{-8}$  s, the total number of angular grid points  $N_y = N_x/20$ . We find linear convergence for the global energy conservation.

extrema, which are present in the interior of the numerical domain in this test (see [44] for alternative *essentially nonoscillatory* schemes).

### 4.3 Tests concerning supernova core collapse

In this section, we present tests aimed to calibrate our code specifically to the studies of supernova core collapse presented in Chapter 7.

#### 4.3.1 Shock reflection test

So far, we have not made any statement about the shock-capturing properties of our hydrodynamical schemes. In order to assess these properties in our code, we perform a shock reflection test in Minkowski space. This is a standard problem to calibrate hydrodynamical codes [96]. A cold, relativistically inflowing ideal gas is reflected at the origin of the coordinate system, which gives rise to a strong shock. We start the simulation with a constant density region, where  $\rho = \rho_0$ ,  $u^r = u_R^r$  and  $\epsilon = \epsilon_R = 0$  (we set  $\epsilon \approx 10^{-11}$  for numerical reasons). From the continuity equation it follows immediately, that the rest mass density in the unshocked region obeys

$$\rho_R(u, r) = \rho_0 \left( 1 - \frac{u_R^r}{u_R^u} u \right)^2. \quad (4.13)$$

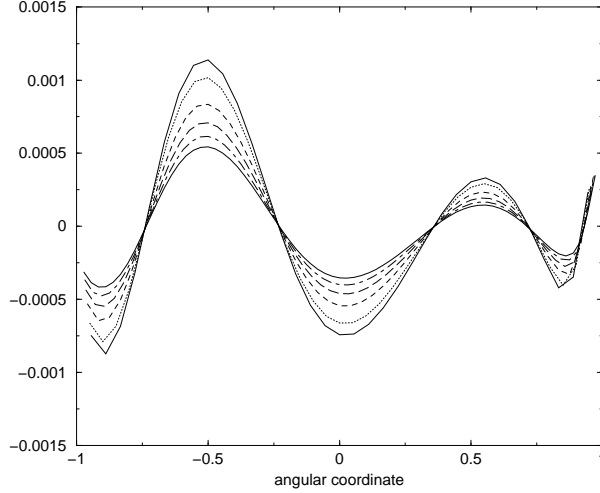


Figure 4.9: Consistency check for the global norm of Eq. (4.11) at  $\mathcal{J}^+$ . Plotted are deviations from zero as a function of the angular coordinate  $y$  and for the same resolutions used in Fig. 4.8. The errors decrease with resolution. The convergence rate is one.

From momentum conservation, it is clear that the velocity in the shocked region vanishes,  $u_L^r = 0$ . Evaluating the Rankine-Hugoniot jump conditions for the fluid equations, we obtain

$$s = \frac{(\Gamma - 1)\epsilon_L}{u_R^u - 1 - \Gamma\epsilon_L}, \quad (4.14)$$

$$\epsilon_L = u_R^u + u_R^r - 1, \quad (4.15)$$

$$\rho_L = \rho_s \frac{\Gamma(u_R^r)^2 - (\Gamma - 1)\epsilon_L}{(\Gamma - 1)\epsilon_L}, \quad (4.16)$$

$$p_L = (\Gamma - 1)\rho_L\epsilon_L. \quad (4.17)$$

Here,  $s$  denotes the shock speed and  $\rho_s = \rho_R(u, r = su)$  the rest mass density in front of the shock.

We used this test with different values of the fluid velocity, and different methods for the fluid evolution. Fig. (4.10) shows a typical result for the shock reflection test for an ultrarelativistic flow ( $u^r = -0.9999c$ ). For this result, we used the HLL solver and increased the numerical viscosity by a factor 2 in order to damp small post-shock oscillations. With the use of shock-capturing schemes, the shock front is very steep, we resolve it with only one or two radial zones. The deviation close to the origin, the so-called *wall heating*, is a well-known failure of finite-difference schemes for this problem [113], which is not important for our purposes.

### 4.3.2 Convergence tests

In the following, we will describe some tests which check various properties of the spherical collapse for the core collapse supernova studies. We choose a particular collapse model, for which the initial central density is  $\rho_c = 1.62 \times 10^{-8}$  (in units  $G = c = M_\odot = 1$ ), the polytropic

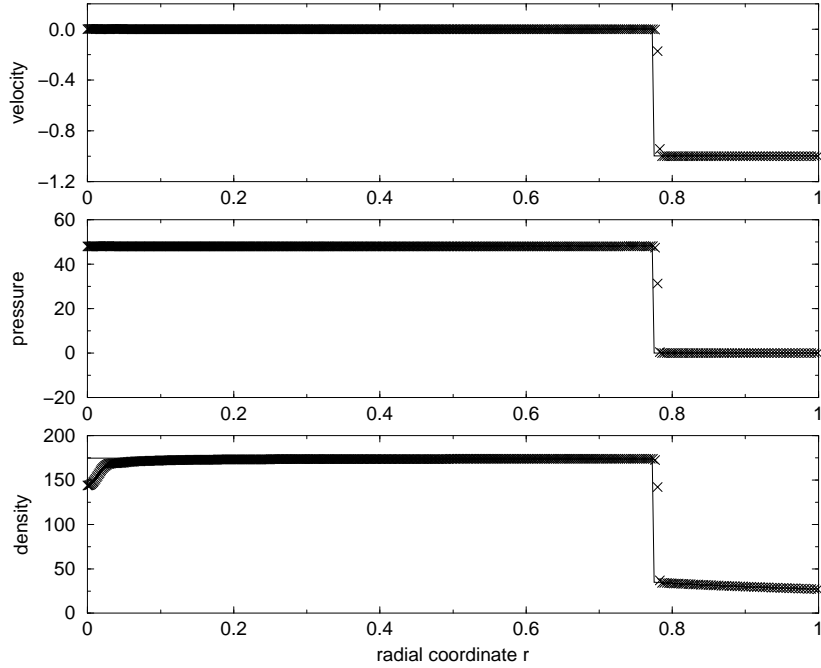


Figure 4.10: Shock reflection test for an ultrarelativistic flow with  $u^r = -0.9999c$  and  $\rho_0 = 8$  and EoS  $p = 5 \times 10^{-4} \rho^{\frac{5}{3}}$ , which is reflected at the origin of the coordinate system. We have plotted different fluid quantities after the evolution time  $u = 2.029$  as a function of the radial coordinate  $r$ . Top panel: fluid velocity  $u^r$ . Middle Panel: pressure  $p$ . Bottom Panel: rest mass density  $\rho$ . The solid line corresponds to the exact solution, the crosses are taken from our numerical simulation. For the above result, we made use of a non-equidistant radial grid  $r = x/(1 - x^{\frac{5}{2}})$  with 800 radial zones, the MC slope limiter and the HLL approximate Riemann solver.

constant is  $\kappa = 0.46$ , and the collapse is induced by resetting the adiabatic exponent to  $\Gamma_1 = 1.3$  (for the equilibrium model with  $\Gamma = \frac{4}{3}$ ). We use the hybrid EoS (see Sec. 2.2.2).

### Thermal energy during the infall phase

Before the central density of the collapsing core reaches nuclear densities, the collapse is exactly adiabatic. Hence, the thermal energy, which vanishes initially, should vanish throughout this phase. This can be easily checked and used for convergence tests. Fig. 4.11 shows the result after an integration time of 30 ms (when the central density has increased by roughly a factor 10). We find, that the errors from the exact result  $\epsilon_{th} = 0$  converge to zero, the convergence rate is 2. Note that, although  $\epsilon_{th} \geq 0$  from the physical point of view, the numerical errors can result in negative values for  $\epsilon_{th}$ .

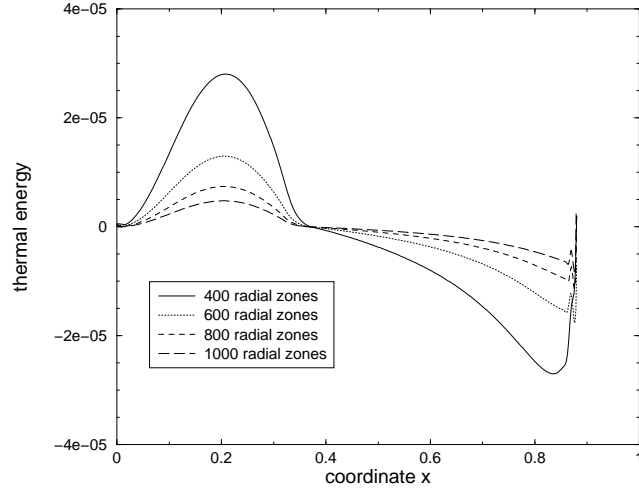


Figure 4.11: Thermal energy as a function of the radial coordinate  $x$  after 30 ms for a compactified grid  $r = \frac{200x}{1-x^2}$  for different resolutions. Due to numerical errors, the thermal energy is different from zero. Deviations converge to zero, the convergence rate is 2.

### Time of bounce

Using the axisymmetric code developed by Dimmelmeier et al. based on the conformally flat metric approach [32], we can perform comparisons between the evolutions of the same initial models. As the conformally flat metric approximation is exact for spherical models, comparisons in spherical symmetry are unambiguous.

We define the time of bounce as the time, when the central density reaches its maximum. In order to start with the same initial data, we started our collapse by ray-tracing the evolution of Dimmelmeier’s code to obtain the initial data on our null cone.<sup>1</sup> Fig 4.12 shows the evolution of the central density for the relativistic code of [32] and the results of our null code for two different grid functions. In Table 4.1, we have summarized our results for the time of bounce. Assuming

	code	grid function	radial resolution	time of bounce [ms]
1	CFC code [32]	see [32]	80*	38.32
2	null code	$r = \frac{150x}{1-x^4}$	600	40.86
3	null code	$r = \frac{150x}{1-x^4}$	800	39.90
4	null code	$r = \frac{150x}{1-x^4}$	1000	39.45
5	null code	$r = 100 \tan(\frac{\pi}{2}x)$	1200	38.92

\* This number for the radial resolution cannot be directly compared to the values for our code, as we resolve the exterior vacuum region up to future null infinity with our code as well.

Table 4.1: Summarized times of bounce for the grid functions and resolutions.

<sup>1</sup>There is no principal advantage in starting with initial data on a null cone or on a Cauchy slice. Ideally, results from stellar evolution would give exact initial conditions for the core collapse, thus eliminating the artificial procedure of resetting  $\Gamma$  to initiate the collapse.

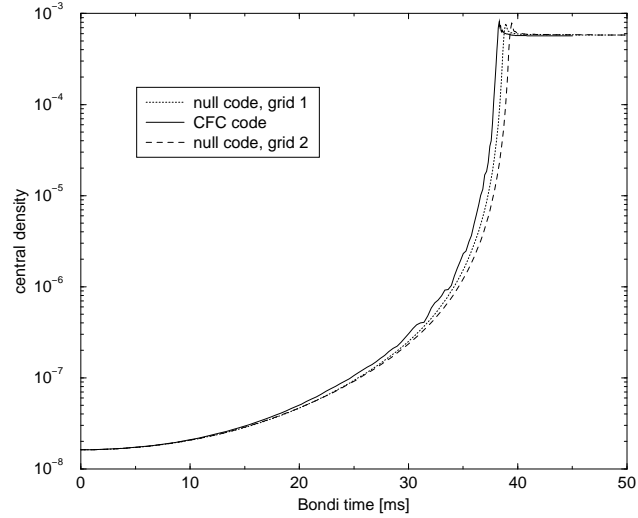


Figure 4.12: Evolution of a central density for a supernova core collapse induced by resetting the adiabatic exponent to  $\Gamma_1 = 1.30$ . The central density increases by almost 5 orders of magnitude, before the core bounces. In the late phase, when a neutron star has formed in the interior region, the central density stays almost constant. The different lines correspond to different grid functions and resolutions, see run 1, 4 and 5 in Table 4.1.

our code is exactly second order convergent and extrapolating our results to an hypothetical infinite resolution, we obtain from runs 3 and 4, that the infinite resolution run bounces after 38.65 ms. This is internally consistent, a comparison of runs 2 and 4 results in a value of 38.66 ms. Using an even higher resolution for a different grid function in run 5, we observe a time of bounce close to the converged result. Our results on the time of bounce are in very good agreement with the result of [32], who find a value of 38.32 ms. The observed difference of less than 1% should be either due to the fact that the result of [32] is not converged, or due to the different radial coordinates used in both codes, and thus small differences in the initial data.

As it can be seen in Fig. 4.12, the comparison does not only give very good agreement for the time of bounce, but also for the dynamics of the central density in general. This is very important, since it shows that the global dynamics of the core collapse is correctly described for our numerical implementation.



## Chapter 5

# Relativistic stars interacting with scalar fields

This chapter describes the first example of the use of characteristic numerical relativity in an astrophysical context. We study dynamical relativistic star spacetimes, collapse and generation of radiative signals. The numerical investigation is performed in spherical symmetry and uses a self-gravitating, massless scalar field. The latter serves as a simple matter model in general relativity which mimics gravitational waves. This analogy is motivated by the observation, that - despite of fundamental physical differences (e.g. concerning the spin) - the dynamical equation for the scalar field (i.e. the Klein-Gordon-equation) exhibits a similar mathematical structure as the evolution equation for gravitational waves in multidimensional general relativity. Scalar fields have been frequently used in studies of global properties of spacetimes, black hole formation and the properties of radiative signals. These studies include the interaction of scalar waves and black holes (e.g. [63, 95]) and especially the emergence of power-law tails in the radiative signal [67, 68, 65, 121], which arise from the late time backscattering of the scalar field at the exterior spacetime geometry [125, 126]. In contrast, there are only few studies of the interaction of scalar fields with fluid stellar objects. Recently [70] analyzed the scattering of scalar fields off boson stars and the emergence of critical phenomena for this setup. They found that the scalar field can either make the boson star collapse to a black hole or to disperse its mass to infinity.

Time-dependent simulations of the scattering of gravitational wave packets off relativistic stars, as a means of computing the frequency spectrum of the relativistic star (see, e.g. [85] for a recent review), have been studied by Allen et al. [1] for polytropic EoS, and by Ruoff [129] for more realistic EoS. Both simulations were performed using linear perturbation techniques. Pavlidou et al. [122] studied the radiative falloff of scalar fields in neutron star spacetimes, using (idealized) analytic, constant density relativistic star models and assuming stationarity for the fluid and the geometry.

In the present chapter we show results from the nonlinear dynamics of relativistic stars interacting with scalar fields. We are especially interested in the following questions: How does a stable relativistic star react when it interacts with the scalar field? Can the scalar field induce gravitational collapse? What is the result of the interaction on the scalar field? In order to answer these questions we numerically obtain spherically symmetric evolutions of

the Einstein-Klein-Gordon perfect fluid system. We study the reflection of finite scalar wave packets off relativistic stars for a series of models, parametrized by the central density, for a given polytropic EoS of polytropic index  $n = 1$ . Our study focuses on the dynamics of the system during the interaction, both the generation of nonlinear fluid oscillations and the gravitational collapse of the fluid component to a black hole.

## 5.1 Mathematical framework

We consider a general spherically symmetric spacetime with a two component stress energy tensor of a perfect fluid and a scalar field,  $T^{ab} = T_F^{ab} + T_\Phi^{ab}$ . The geometry of our setup follows the Tamburino-Winicour-formalism [146], as already described in Sec. 2.1.

### 5.1.1 Einstein equations

By adopting the Bondi-Sachs [18, 131] form of the metric element in spherical symmetry,

$$ds^2 = -\frac{e^{2\beta}V}{r}du^2 - 2e^{2\beta}dudr + r^2(d\theta^2 + \sin^2\theta d\phi^2), \quad (5.1)$$

the spacetime geometry is completely described by the two functions  $\beta(u, r)$  and  $V(u, r)$ .

A sufficient set of Einstein equations for obtaining the spacetime development is grouped as

$$G_{ur} = \kappa T_{ur}, \quad (5.2)$$

$$G_{rr} = \kappa T_{rr}, \quad (5.3)$$

$$G_{uu}|_\Upsilon = \kappa T_{uu}|_\Upsilon, \quad (5.4)$$

where the  $u$  coordinate is defined by the level surfaces of a null scalar.<sup>1</sup> The angular coordinates  $(x^2, x^3) = (\theta, \phi)$  are both Killing coordinates here. The first two Einstein equations, Eqs. (5.2) and (5.3), contain only radial derivatives and are to be integrated along each null surface. The last equation (5.4) is a *conservation* condition, satisfied on the vertex of the null cones  $\Upsilon$  due to the regularity conditions. As in Sec 2.1, we choose  $\Upsilon$  to be a timelike geodesic which coincides with the origin of a relativistic star at  $r = 0$ . Equation (5.3) may be substituted for by the equivalent expression  $g^{AB}R_{AB} = 8\pi g^{AB}(T_{AB} - g_{AB}T/2)$ , where  $R_{ab}$  is the Ricci tensor and the indices  $(A, B)$  run over the angular coordinates  $x^2, x^3$ .  $T$  is the trace of the stress energy tensor  $T_{ab}$ ,  $T = g^{ab}T_{ab}$ .

Using the line element and Eqs. (5.2) and (5.3) the  $\beta$  and  $V$  hypersurface equations are given by

$$\beta_{,r} = 2\pi r T_{rr}, \quad (5.5)$$

$$V_{,r} = e^{2\beta}(1 - 4\pi r^2(g^{AB}T_{AB} - T)). \quad (5.6)$$

The comma in the above equations indicates, as usual, partial differentiation. Boundary conditions for  $(\beta(u)\Upsilon, V(u)\Upsilon)$ , needed for the radial integrations, are provided by imposing regularity at the origin, where the coordinate system is assumed to be a local Fermi system, leading to

---

<sup>1</sup>Note however, that the coordinate vector  $(\frac{\partial}{\partial u})^a$  is timelike.

$\beta = O(r^2)$ ,  $V = r + O(r^3)$ . By imposing such conditions at the origin, the lapse of coordinate time  $du$  is related to the corresponding lapse of “retarded time”  $d\tau$  measured by distant observers at  $r \rightarrow \infty$  by

$$d\tau = e^{2H} du, \quad (5.7)$$

where  $H = \lim_{r \rightarrow \infty} \beta$ .

### 5.1.2 Scalar field equations

The dynamics of a scalar field  $\Phi$  is governed by the minimally coupled Klein-Gordon equation in spherical symmetry,

$$\nabla_a \nabla^a \Phi = 0, \quad (5.8)$$

where  $\nabla_a$  is the covariant derivative. The corresponding stress energy tensor is given by

$$T_{\Phi}^{ab} = \nabla^a \Phi \nabla^b \Phi + L g^{ab}, \quad (5.9)$$

where  $L$  is the massless scalar field Lagrangian ( $2L = -\nabla_a \Phi \nabla^a \Phi$ ). Using a characteristic foliation, Eq. (5.8), takes the form

$$2(r\Phi_{,u})_{,r} = \frac{1}{r}(rV\Phi_{,r})_{,r}. \quad (5.10)$$

In terms of the intrinsic 2-metric of the  $(u, r)$  sub-manifold,

$$\eta_{CD} dx^C dx^D = -e^{2\beta} du \left( \frac{V}{r} du + 2dr \right), \quad (5.11)$$

where the indices  $(C, D)$  run over the coordinates  $(u, r)$ , Eq. (5.10) reduces to

$$\square^{(2)} g = \frac{e^{-2\beta}}{r} g \left( \frac{V}{r} \right)_{,r}, \quad (5.12)$$

where

$$g = r\Phi \quad (5.13)$$

and  $\square^{(2)}$  is the D'Alembertian operator associated with  $\eta_{CD}$ .

### 5.1.3 Hydrodynamic equations

The evolution of the fluid is determined by the local conservation laws of stress energy and density current

$$\nabla_a T_F^{ab} = 0, \quad (5.14)$$

$$\nabla_a (\rho u^a) = 0, \quad (5.15)$$

where  $T_F^{ab}$  is the stress energy tensor of a perfect fluid

$$T_F^{ab} = \rho h u^a u^b + p g^{ab}. \quad (5.16)$$

Following [119], after introducing the definitions  $D = \rho u^0$ ,  $S^r = T_F^{0r}$  and  $E = T_F^{00}$ , the fluid equations can be cast into a first-order flux-conservative, hyperbolic system for the state-vector  $\mathbf{U} = (D, S^r, E)$  :

$$D_{,u} + F_{,r}^{r0} = -(\ln \sqrt{-g})_{,u} D - (\ln \sqrt{-g})_{,r} F^{r0}, \quad (5.17)$$

$$S_{,u}^r + F_{,r}^{r1} = -(\ln \sqrt{-g})_{,u} S^r - (\ln \sqrt{-g})_{,r} F^{r1} - \Gamma_{ab}^r T_F^{ab}, \quad (5.18)$$

$$E_{,u} + F_{,r}^{r4} = -(\ln \sqrt{-g})_{,u} E - (\ln \sqrt{-g})_{,r} F^{r4} - \Gamma_{ab}^u T_F^{ab}, \quad (5.19)$$

$\Gamma_{ab}^c$  are the Christoffel symbols. In contrast to the description in Sec 2.2, we solve the fluid equations on the radial grid  $r$  and we have explicitly used the Christoffel symbols in the source terms. The precise form of the vector of fluxes  $\mathbf{F}$  can be obtained by using Eqs. (5.14)-(5.15) (see also [119]). The explicit relations between the primitive variables  $\mathbf{w} = (\rho, \varepsilon, u^r)$  and the conserved variables  $\mathbf{U} = (D, S^r, E)$ , for a perfect fluid EoS,  $p = (\Gamma - 1)\rho\varepsilon$ , where  $\Gamma$  is the adiabatic index of the fluid, are given in Sec 2.2.2.

With the above definitions, the metric equations (5.5)-(5.6) read, for the combined stress energy tensor of a fluid-scalar field system,

$$\beta_{,r} = 2\pi r(\rho h(u_r)^2 + (\Phi_{,r})^2), \quad (5.20)$$

$$V_{,r} = e^{2\beta}(1 - 4\pi r^2(\rho h - 2p)). \quad (5.21)$$

Following [92] we express the hydrodynamic quantities on the right-hand side of Eqs. (5.20)-(5.21) solely in terms of the conserved hydrodynamic quantities  $\mathbf{U}$ . This procedure has the advantage, that no iterations in the numerical integration of the hypersurface equations are necessary, as long as we use explicit algorithms for their solution.

In summary, the initial value problem consists of equations (5.4), (5.12), (5.17)-(5.19), (5.20), (5.21), the scalar field initial data  $\Phi(r, u_0)$  and initial and boundary data for the fluid variables  $(\rho, \varepsilon, u^r)$  on the initial slice  $\Sigma_0$  (at time  $u_0$ ). These equations and initial data are sufficient for obtaining a global solution to the problem.

#### 5.1.4 Global quantities

Making use of the characteristic formulation of general relativity and covering the infinite range of the radial coordinate with a finite grid allows us to refer to some global quantities of the spacetime such as the Bondi mass and the news function. Apart from their physical relevance, these quantities can be used in global tests of our numerical evolutions, as we will show below.

Instead of extracting the Bondi mass directly at future null infinity we use the expression

$$M = 4\pi \int_0^\infty r^2 e^{-2\beta} T_{ru} dr \quad (5.22)$$

for the Bondi mass at time  $u$  in our numerical implementation. Similarly, the news can be rewritten as [62]

$$N = \frac{1}{2} e^{-2H} \int_0^\infty \frac{V}{r} \Phi_{,r} dr. \quad (5.23)$$

With these definitions, global energy conservation can be established,

$$M(u) - M(0) = \int_0^u -4\pi N(\hat{u})^2 e^{2H(\hat{u})} d\hat{u}. \quad (5.24)$$

## 5.2 Numerical implementation

In order to study the interaction of the scalar field and the relativistic star in a global spacetime we use non-equidistant grids for the radial coordinate  $r$  extending to infinity. Furthermore, to avoid dealing with complicated stencils in the numerical implementation, we make use of the coordinate transformation given by Eq. (2.12). Unless otherwise stated we use the relation

$$r = \frac{15x}{1-x^4} \quad (5.25)$$

for all computations presented in this chapter. Using such a coordinate transformation, the repartition of grid points in the coordinate  $r$  is almost equidistant for small radii and gets infinitely sparse for  $x \rightarrow 1$ , which corresponds to future null infinity  $\mathcal{J}^+$ .

We use a second order Runge Kutta method to solve the metric equations (5.20) and (5.21). To determine the equilibrium models for the fluid configuration, we also use the Runge Kutta method to solve the Tolman-Oppenheimer-Volkoff equations, formulated on a null hypersurface, Eqs. (2.62) and (2.63).

The integration of the evolution equation for the scalar field, Eq. (5.12) (or equivalently Eq. (5.10)), proceeds with the specification of initial data  $\Phi(u_0, r)$  on the initial null cone  $u_0$ . For the characteristic evolution we have used and compared the two different algorithms which were described in Sec. 3.2.1. This is possible, since Eq. (5.12) and Eq. (2.24) have the same principal part when identifying the variables  $\hat{\psi}$  in Eq. (2.23) and  $g$  in Eq. (5.13). For the second algorithm we use the non-dissipative form of the algorithm setting  $\hat{\epsilon} = 0$ .

Due to the stencils of the two algorithms, we cannot use them at the origin, where regular behavior of the scalar field as  $\Phi = a + br + cr^2$  is assumed. The linear term introduces a kink at the origin, but this is necessary in our foliation - as can be seen from the analytic solution for the wave equation in Minkowski space consisting of an in-going and outgoing wave. Note that the scalar field enters the metric only through Eq. (5.20), thus respecting the regularity conditions at the origin. Substituting this ansatz for  $\Phi$  into Eq. (5.10) and grouping those terms with the same powers of  $r$  we find that  $a_{,u} = b$ ,  $b_{,u} = 1.5c$ . Extracting the coefficients  $a, b$  and  $c$  on the null cone  $u_0$ , we update  $a$  and  $b$  to obtain the scalar field at the first two grid points of the new hypersurface, which then allows us to start the marching procedure along the null hypersurface with either of the two algorithms described in Sec. 3.2.1.

By experimenting with both algorithms we found that, on the one hand, the scheme based upon a direct discretization of the wave equation is more accurate in the long-term behavior in the interior of the numerical domain. This was relevant to resolve the late time fall-off behavior of the scalar field, as we describe below in Sec. 5.4. On the other hand, the algorithm based upon the null parallelogram is superior close to future null infinity, where we regularized the equations following the work of [60]. Therefore, for the results presented in this chapter we have used a “hybrid algorithm”, in which a direct discretization of the Klein-Gordon equation (5.10) is used in the interior of the computational domain and the parallelogram algorithm is used close to future null infinity  $\mathcal{J}^+$ .

Concerning the numerical integration of the system of hydrodynamic equations, we employ the high-resolution shock-capturing schemes described in Sec. 3.1. In more precise terms the hydrodynamics solver uses the piecewise linear reconstruction procedure MUSCL at each cell-interface and the HLL approximate Riemann solver.

### 5.3 Code calibration

The assessment of the numerical implementation is achieved primarily by comparing with independent physical results and performing global energy conservation tests.

#### 5.3.1 Null cone evolution of stable stars

As a first step to calibrate our algorithms we quantify our results on the stability of neutron stars described in Sec 4.2.1. We use evolutions of stable relativistic stars to compute the frequencies of the radial modes of pulsation. Those frequencies are compared with results of linear evolutions from perturbation theory.

For all simulations presented in this chapter the star models are approximated by a polytropic EoS with polytropic constant  $\kappa = 100$  and adiabatic exponent  $\Gamma \equiv 1 + 1/n = 2$ . Hence, the index of the polytrope is  $n = 1$ . For the simulation presented in this section we choose the model with central density  $\rho_c = 1.5 \times 10^{-3}$  (recall that we use units in which  $G = c = M_\odot = 1$  - the value corresponds to  $\rho_c = 9.3 \times 10^{14} \text{ g cm}^{-3}$ ). This model is located in the stable branch of the central density - total mass - diagram (see Fig. 5.1).

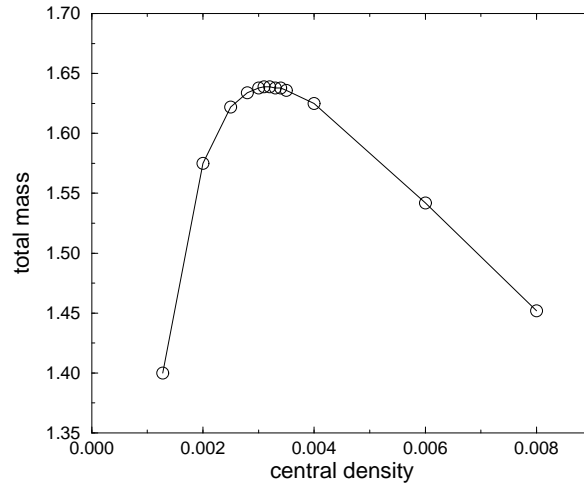


Figure 5.1: Stability curve for neutron star models with the polytropic equation of state  $p = \kappa\rho^\Gamma$ , with  $\kappa = 100$  and  $\Gamma = 2$ . Models lying to the left of the maximum of the curve, at about  $\rho_c = 3.2 \times 10^{-3}$ , are stable against gravitational collapse. The circles are calculated with our initial data solver and are connected by straight lines. We use units in which  $G = c = M_\odot = 1$ .

To compute the frequencies of radial pulsation modes, we allow the star to (radially) contract and expand during the evolution. Following [43] (see also [44]), we surround the star with a few zones representing an artificial “atmosphere” filling an otherwise vacuum region. The density in this atmosphere is set to sufficiently small values such that its presence does not affect the dynamics of the system. Typical values we choose are  $10^{-7} - 10^{-8}$  times the central density of the star. Furthermore, to avoid any numerical problems due to (shock) heating in the atmosphere (the fluid in those zones is not in equilibrium and, therefore, it will collapse/accrete onto the star), we follow the recipe described in [43] and enforce adiabatic evolution (by using the polytropic EoS) in the atmosphere and in the outer layers of the relativistic star (comprising the outermost 10 grid points). After each time step, if the density has fallen below 1.5 times the density of the atmosphere, the hydrodynamic quantities are reset to their atmosphere values. The innermost location where this procedure is done defines the radius of the star. As described in more detail in the next section the above values of the atmosphere density are small enough to guarantee conservation of energy despite the artificial resetting procedure.

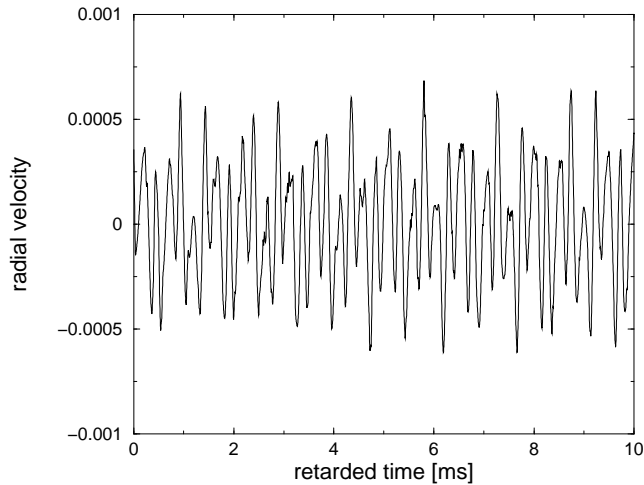


Figure 5.2: Time evolution of the radial velocity  $u^x$  at half radius of the star. The stellar model has a central density  $\rho_c = 1.5 \times 10^{-3}$ . The oscillations are essentially undamped for the evolution shown, which reflects the small viscosity of the hydrodynamic scheme employed.

When evolving our stellar model in time, we find small deviations around the equilibrium values due to the discretization errors. As a result, the star oscillates in a superposition of radial modes. Figure 5.2 shows the radial velocity at half stellar radius for the above model as a function of retarded time measured by distant observers. This simulation was performed with a grid of 800 zones covering the complete radial domain. This amounts to using about half of the available grid in resolving the relativistic star (We choose this resolution here to allow for comparisons with the results of Sec. 5.4, where we resolve the scalar field as well.) As shown in [44] one can use such evolutions to obtain the frequencies of the excited modes of pulsation of the star by simply Fourier transforming those data. In general, however, the excitation of

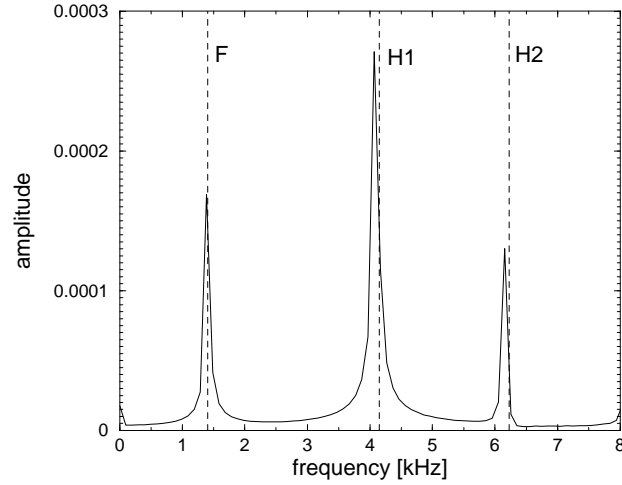


Figure 5.3: Fourier transform of the time evolution shown in Fig. 5.2. The peaks in the Fourier transform indicate the mode frequencies of the fundamental radial mode (around  $f = 1.4$  kHz) and the first two harmonics. The relativistic star model has a central density  $\rho_c = 1.5 \times 10^{-3}$ . The dashed vertical lines indicate the corresponding frequencies obtained with a perturbative (linear) code. The units in the  $y$ -axis are arbitrary.

the different modes by the truncation error of the numerical schemes may not be sufficient to accurately determine the mode frequencies. The discretization error introduces at each grid point a non-stationary perturbation. The pointwise nature of those perturbations implies that the spectrum of induced oscillations is fairly broad, practically covering all wavenumbers representable on a given grid resolution, but with varying power in different regimes. In order to excite the relevant modes more strongly, we perturb the density of the equilibrium models with an explicit function  $\rho = \rho_o + A\rho_c \sin(\pi r/R)$ , where  $R$  denotes the radius of the star (see Table 5.1) and  $\rho_o$  is the density of the unperturbed star. The typical amplitude we use for this perturbation is  $A = 10^{-6}$ .

Figure 5.3 shows the frequencies of the fundamental mode and the first two overtones obtained by a Fourier transform of the radial velocity profiles. The dashed vertical lines in this plot were obtained using a code [130] which solves the linearized perturbation equations. The agreement between the two codes is very good. Similar results were obtained for a relativistic polytrope with  $\rho_c = 2.8 \times 10^{-3}$ , for which the fundamental mode is already rather small, the star being close to the unstable branch. We note that the code is able to track considerably higher overtones as well, but for the sake of clarity in the comparison it is sufficient to show only the first two harmonics.



### 5.3.2 Scalar field dynamics in a regular spacetime

In this section we present results aimed to validate the numerical implementation of the Einstein-Klein-Gordon solver. For this purpose we investigate the reflection of a scalar field at the origin of the coordinate system, turning off the hydrodynamics module of the code. The initial data for the scalar field packet are

$$\Phi_0 = 2 \times 10^{-3} e^{-(r-14)^2}. \quad (5.26)$$

The location of this Gaussian pulse is chosen in such a way that, if superposed on the relativistic star spacetimes of the previous section, the scalar field data would initially lie outside the relativistic star. Evolving these data, the initial pulse approaches the origin, is reflected there (i.e. the pulse of ingoing waves is transformed to a pulse of outgoing waves), and radiates away, leaving behind Minkowski space. Such a sequence can be followed in Fig. 5.4, for a simulation employing a grid of 800 zones. We note the stability and smoothness of the solution, both at the origin and at  $\mathcal{J}^+$ . By evaluating global energy conservation, according to Eq. (5.24), after the pulse has reflected off the origin, we find that the energy is conserved (as expected) to second order accuracy. As an aside we note that by simply changing the origin treatment in the code, it is possible to study the evolution of a scalar field outside a spherical black hole. We performed such a simulation finding agreement with the results of [65].

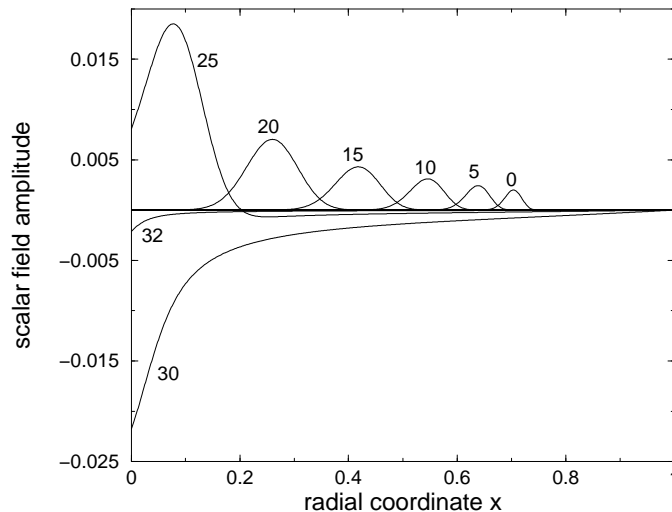


Figure 5.4: Radial profiles of the scattering of a scalar field off the origin of the coordinate system. The number labels refer to the time coordinate  $u$ . For times  $u \geq 35$  the pulse has completely radiated away leaving Minkowski spacetime behind.

### 5.3.3 Global energy conservation

We consider now the full set of equations and prescribe initial data consisting of a scalar field component given by Eq. (5.26), together with a stable, equilibrium, relativistic star model with initial central density  $\rho_c = 1.28 \times 10^{-3}$ ,  $\kappa = 100$  and  $\Gamma = 2$ . We calculate for this stellar model

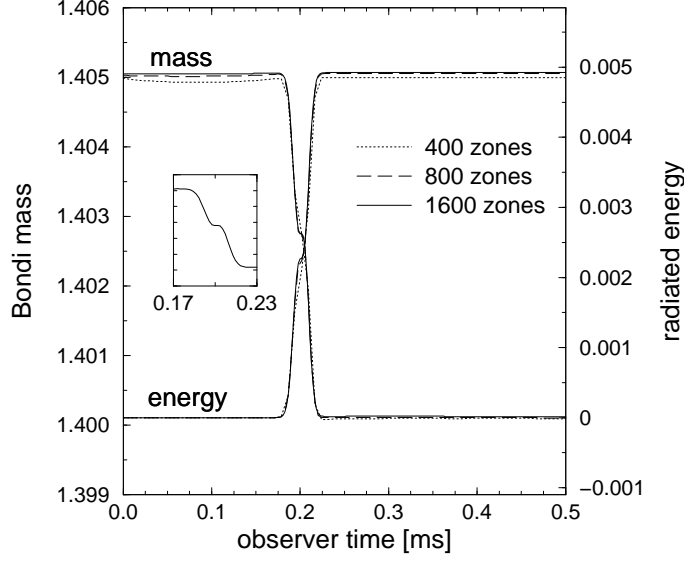


Figure 5.5: Bondi mass of the spacetime and total radiated energy of the scalar field as a function of retarded time for different resolutions. At the beginning, the scalar field contributes to the Bondi mass of the spacetime ( $1.405M_{\odot}$ ), before the Bondi mass drops in a small time interval, when the main part of scalar field mass (about  $5 \times 10^{-3}M_{\odot}$ ) is emitted to future null infinity  $\mathcal{J}^+$ . As the sum of the two curves is constant, the energy is globally conserved (with a relative error of about  $5 \times 10^{-6}$  for the run with 1600 zones.). The mass drops in two steps around 0.2 ms, which can be seen from the magnified figure obtained for the case of 1600 zones.

a total mass of  $1.4 M_{\odot}$ , in agreement with [44]. We perform simulations of the scalar field scattering off the relativistic star, focusing our study in this Section on the assessment of the global energy conservation properties of the coupled numerical algorithm. A comprehensive study of the dynamics of the scattering is deferred to Sec. 5.4.

Fig. 5.5 shows the Bondi mass of the relativistic star - scalar field spacetime as a function of retarded time, combined with the total mass of the scalar field radiated away to null infinity. As one can clearly see from this figure, the spacetime loses exactly the same amount of mass, which is radiated to null infinity by the scalar field.

By computing Eq. (5.24) at a fixed retarded time of  $\tau = 0.5$  ms for different grid resolutions, we find that our code conserves globally the energy with a convergence rate which lies in between 1 and 2. The fact that the convergence rate drops now below second order is, however, to be expected, since the approximate Riemann solver used for the integration of the hydrodynamic equations is only (locally) first order accurate at discontinuities (i.e., the surface of the star) and at local extrema (i.e., the center of the star) (see the related discussion in [44]). Nevertheless, for the highest resolution we have used, 2000 radial grid points, the relative error in the energy conservation is of the order of  $2 \times 10^{-6}$  for this very dynamical simulation.

At first sight the decay of the scalar field mass in two steps (as shown in Fig. 5.5 around 0.2 ms) seems surprising. However, looking at the radiated power  $\frac{dM_B}{du} = -4\pi e^{-2H} (\lim_{r \rightarrow \infty} g_{,u})^2$  and approximating the solution of Eq. (5.12) by the solution in Minkowski space  $g(u, r) =$

$f(\frac{u}{2} + r) - f(\frac{u}{2})$ , where  $f$  is determined by the initial profile with suitable falloff behavior for large radii, the radiated power reads  $\frac{dM_B}{du} = -\pi e^{-2H} f'(\frac{u}{2})^2$ . Hence the radiated power as a function of time measures the square of the derivative of the initial scalar field profile.

## 5.4 Dynamics of scalar field - relativistic star interactions

In this section we present our main results concerning the scattering of a scalar field pulse off a relativistic star. As mentioned before, we use  $n = 1$  relativistic polytropes as the underlying star model. All configurations we construct are stable and are characterized by increasing central densities and compactness. Their basic properties are summarized in Table 5.1.

Table 5.1: Equilibrium properties of the  $\kappa = 100$ ,  $n = 1$  relativistic star models in units in which  $c = G = M_\odot = 1$ . The entries are as follows:  $\rho_c$  is the central density,  $M$  and  $R$  are the mass and radius of the star, respectively, and  $C = 2M/R$  is the compactness parameter.

$\rho_c$ ( $10^{-3}$ )	$M$	$R$	$C = 2M/R$
1.5	1.47	9.26	0.317
2.2	1.60	8.45	0.379
2.8	1.63	7.91	0.412
2.9	1.64	7.84	0.418
3.0	1.64	7.76	0.423

On the initial outgoing light cone, in addition to the fluid data we introduce a scalar field component in the shape of a Gaussian pulse (according to Eq. (5.26)), thus fixing the pulse amplitude, width and location. For these initial data there is no significant initial overlap between the star and the scalar field which then makes it possible to associate a specific initial mass with each one of the matter fields.

In our exploration of the parameter space, we use the central density as the only free parameter, maintaining a single polytropic EoS and fixing the profile and amplitude of the scalar field. This is clearly a severe restriction in the parameter space of the scattering problem. Nevertheless, we choose this particular setup since we are interested in investigating the relativistic effects of the interaction, where the scalar field has a strong impact on the dynamics of the relativistic star. A detailed analysis of the whole parameter space is beyond the scope of this work.

When evolving in time the initial data, the scalar field travels inwards, enters the relativistic star and it is finally reflected at the origin of the coordinate system. Contrary to the Einstein-Klein-Gordon system in vacuum (which was discussed in Sec. 5.3.2), the presence of the star and its associated potential well may give rise to a phase of multiple reflections of the scalar field. This, in turn, reflects itself in the existence of quasi-periodic signals (trapped modes), as discussed, e.g., by [122], before its energy is radiated away. Furthermore, our relativistic star models have been chosen conveniently close to the maximum of the stability curve at about  $\rho_c = 3.2 \times 10^{-3}$  (see Fig. 5.1). Depending on the compactness of the neutron star onto which the wave pulse impacts, the stars are forced to either oscillate violently, or to collapse to a black hole on a dynamical timescale. Fig. 5.6 shows the spacetime diagram for the least compact relativistic star model of our sample, with  $\rho_c = 1.5 \times 10^{-3}$ . For this model, the scalar field is

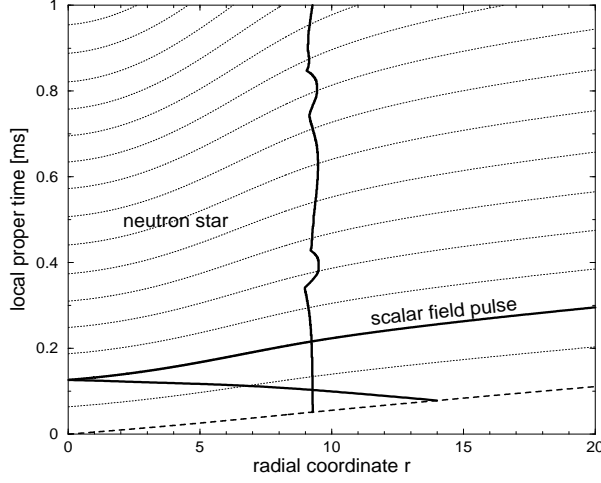


Figure 5.6: Spacetime diagram of the reflection of a Gaussian scalar field pulse off a relativistic star ( $\kappa = 100$ ,  $n = 1$  and  $\rho_c = 1.5 \times 10^{-3}$ ). The diagram focuses on the strong field region but was obtained from a global simulation of the spacetime. The dotted curves covering the whole diagram are outgoing light cones, which bend due to the spacetime curvature (the thicker dashed line corresponds to the initial light cone). The scalar field pulse, initially located at  $r = 14$ , travels inwards, enters the relativistic star and is reflected at the origin of the coordinate system (the solid line corresponds to the maximum value of the scalar field). The interaction with the scalar field triggers the oscillation of the relativistic star, which can be seen from the vertical solid line of varying location in the diagram, which indicates the radius of the star.

able to force the star to contract and to expand, pulsating radially, as can clearly be identified by the varying location of the star's radius (the vertical solid line in Fig. 5.6).

Fig. 5.7 displays the time evolution of the central density of the different relativistic stars in our setup. The solid lines correspond to the relativistic star-scalar field system. Correspondingly, the dashed horizontal lines indicate the evolution of the equilibrium relativistic star models *without* the presence of the scalar field. As already mentioned the initial fluid configurations are stable. The evolution is characterized by the appearance of small-amplitude oscillations associated with the radial modes of pulsation of the star (which are too small to be seen in the figure). On the other hand, all relativistic star-scalar field models with initial central density below  $2.8 \times 10^{-3}$  also oscillate around the stable equilibrium model. The oscillation frequencies of the two least compact models correspond to the frequencies calculated in the linear regime, even though the amplitude of the oscillations is now much larger due to transfer of energy from the scalar field. This is no longer the case for the model with a central density of  $\rho_c = 2.8 \times 10^{-3}$ . For this model, which is close to the threshold of black hole formation, the amplitude of the oscillations is big enough to show nonlinear effects, the oscillation frequency being much smaller than the value obtained from linear studies. For the models with central densities of  $\rho_c = 2.9 \times 10^{-3}$  and  $\rho_c = 3.0 \times 10^{-3}$  the interaction with the scalar field is able to

trigger their gravitational collapse to a black hole on a dynamical timescale. Unfortunately,

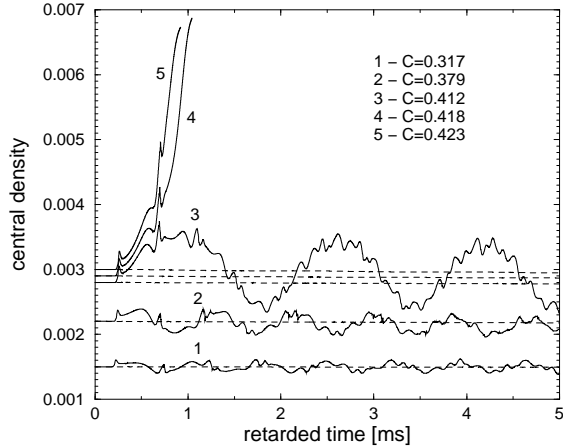


Figure 5.7: Central density of the relativistic stars interacting with the scalar field as a function of retarded time. The curves are labelled according to the stellar compactness in Table 5.1. The three least compact models, with  $\rho_c \leq 2.8 \times 10^{-3}$ , oscillate strongly around their equilibrium configuration after interacting with the scalar field. The other two more compact models collapse to a black hole on a dynamical timescale instead. The dashed lines are taken from our evolutions of the equilibrium model without the presence of the scalar field.

as a consequence of the violent dynamics, we are not able to follow the collapse process once the event horizon is about to form (similar problems were reported in [92] for the collapse of supermassive stars using a spherically symmetric characteristic code). However, convergence studies show clear evidence that these models collapse to black holes. Further evidence is given by the evolution of the relativistic star radii, as shown in Fig. 5.8, and the blow-up of the redshift between the stellar center and future null infinity. We have plotted in Fig. 5.9 the redshift factor  $e^{2H}$  relating the lapse of local proper time at the origin to the lapse of proper time at infinity according to Eq. (5.7). For example, for the model with central density  $\rho_c = 2.9 \times 10^{-3}$ , initially, the redshift factor  $e^{2H}$  between the center of the star and observers located at  $r \rightarrow \infty$  is 2.1. By the end of the simulation it has increased to a value of 59.5. This strong increase in the redshift factor explains that the increase of the central density is stopped towards the end of our numerical evolution (see Fig. 5.7). We note that global energy conservation is well maintained, even for these extreme hydrodynamic simulations. The relative deviation from energy conservation according to Eq. (5.24) when the evolution stops is of the order of  $10^{-4}$ .

By analyzing the energy transfer from the scalar field to the relativistic star during the interaction we find that it increases with the compactness of the stellar model. This behavior is shown in Table 5.2. We remark that the initial mass of the scalar field is not strictly the same in all cases considered, due to the different underlying geometry (determined by the stellar models) on which the initial scalar field data are prescribed. We evaluate the total radiated mass in the scalar field at a retarded time of  $\tau = 0.6$  ms (see Eq. (5.7)). The mass radiated

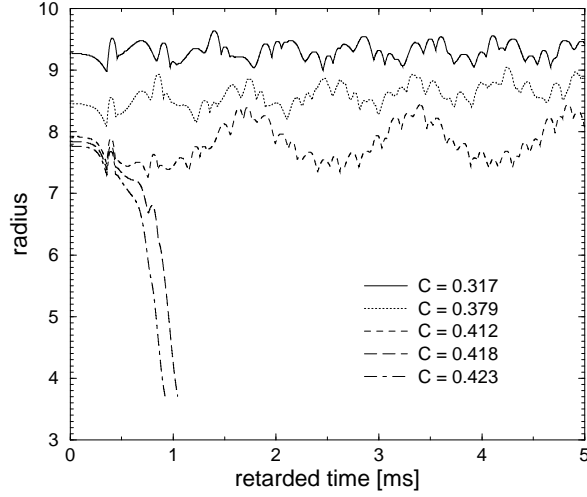


Figure 5.8: Time evolution of the radius of the different relativistic stars interacting with the scalar field. The radius of the two most compact models decreases dramatically, indicating that these models undergo gravitational collapse to a black hole.

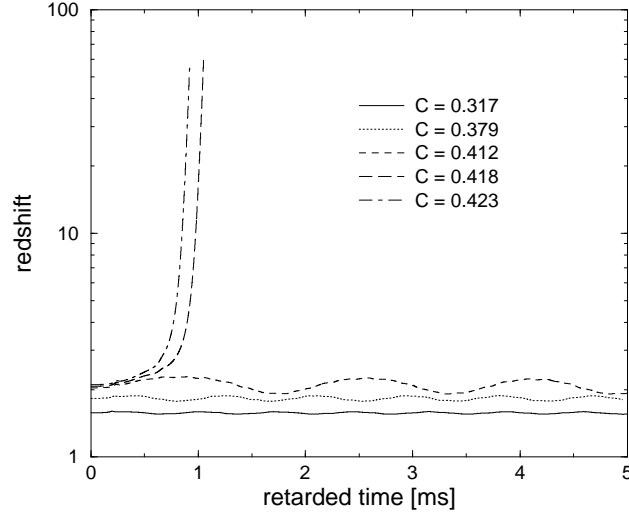


Figure 5.9: Time evolution of the redshift factor  $e^{2H}$  relating the lapse of proper time at the origin to the lapse of proper time at infinity according to Eq. (5.7). The rapid increase in the redshift factor for the two most compact models gives clear evidence for the formation of black holes.

away to infinity after this time is negligible.

Table 5.2: Energy transfer from the scalar field to the relativistic star during the scattering process. The entries are as follows:  $\rho_c$  is the central density of the relativistic star,  $M_0^\Phi$  is the initial mass of the scalar field,  $E_{\text{rad}}$  is the total radiated mass, and  $E_{\text{trans}}$  is the percentage of the energy transferred in the interaction. We use units in which  $G = c = M_\odot = 1$ .

$\rho_c$ ( $10^{-3}$ )	$M_0^\Phi$ ( $10^{-3}$ )	$E_{\text{rad}}$ ( $10^{-3}$ )	$E_{\text{trans}}$ (%)
1.5	4.90	4.86	0.8
2.2	4.80	4.72	1.7
2.8	4.76	4.65	2.3
2.9	4.75	4.63	2.5
3.0	4.75	4.62	2.7

Next we analyze the behavior of the scalar field in these scattering simulations. In Fig. 5.10 we plot the (retarded) time evolution of the news, Eq. (5.23), for the whole sample of our stellar models. The scalar field signal measured at null infinity can be divided into three phases. The first phase, before the main pulse reflects off the origin (not shown in the figure), is dominated by an initial backscattering with small signal amplitude. The second phase, whose duration

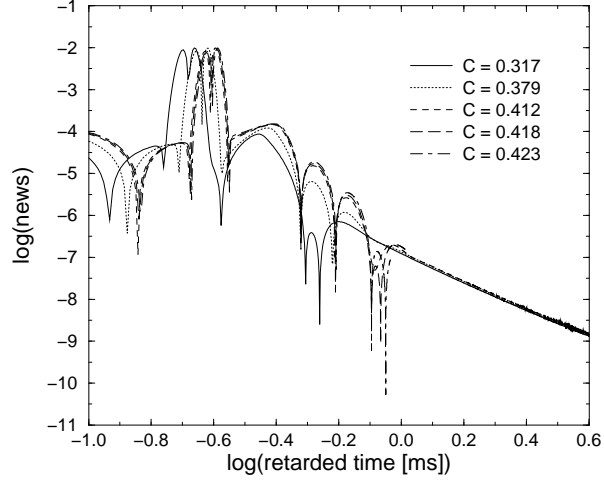


Figure 5.10: Time evolution of the news function during the scattering problem. The different lines correspond to the different models in our sample of Table 5.1, and are labelled in the plot with respect to the compactness parameter. The duration of the more dynamic quasi-normal ringing phase strongly depends on the compactness of the relativistic star model, increasing as the compactness increases. The late time behavior of the signal decays as an inverse power-law.

depends on the compactness of the relativistic star [122], is characterized by the reflection of the main scalar field back and forth between the origin and the maximum of the relativistic

star curvature potential, which, in turn, induces the appearance of quasi-normal oscillations on the scalar field. Most of the energy is radiated away in this period. Once the pulse has lost sufficient energy it enters a third phase, during which the behavior of the signal is dominated by a power-law tail  $N \propto t^{-\alpha}$ , with  $\alpha = 3$ , due to the reflection of the scalar field at the exterior Schwarzschild geometry [125, 126, 67, 68, 122]. Since the compactness of our models is well below the Buchdahl limit<sup>2</sup>,  $C = 8/9$ , the quasi-normal mode ringing phase does not last for an extended period of time. Therefore, after a few reflections trapped inside the curvature potential, the signal enters rapidly the power-law tail phase. From Fig. 5.10 one can see that the more compact the relativistic star, the larger the quasi-normal ring-down phase. We also point out that by going to more compact models, increasing the central density of the relativistic star beyond the maximum of the stability curve (i.e., going to the unstable branch) and freezing the hydrodynamics and metric evolution to avoid gravitational collapse, we are able to find a much longer ring-down phase. Our results, obtained for fully self-gravitating, polytropic relativistic star models, are in good agreement with previous findings by Pavlidou et al. [122], who used a more idealized setup consisting of constant density, static stars.

The study of the late time power-law tails requires increased resolution, especially for large radii. We have hence used a different radial coordinate for these simulations,  $r = 30x/(1 - x^4)$ . This allowed us to resolve the power-law behavior in Fig. 5.10, avoiding the evolution from being dominated by numerical noise mainly due to reflections. By performing a linear regression study of the tails in the time interval  $\log(\tau [ms]) \in [0.3; 0.7]$ , we obtain the results summarized in Table 5.3. We find the correct power-law behavior of the scalar field in our fully dynamical

Table 5.3: Late time power-law behavior of the news  $N \propto t^{-\alpha}$  for the (stable) relativistic star - scalar field scattering problem. The results agree with the value  $\alpha = 3$  predicted by linear theory.

$\rho_c (10^{-3})$	$\alpha$
1.5	3.06
2.2	3.05
2.8	3.05

evolutions, as predicted by both, linear analysis and by nonlinear numerical evolutions of scalar fields in the exterior black hole geometry [67, 68, 65]. Note that we measure the tails of the news, whereas the results of the above references read off the quantity  $g$  at future null infinity  $\mathcal{J}^+$ . Both quantities are related by

$$N = e^{-2H} g_{,u}. \quad (5.27)$$

<sup>2</sup>The Buchdahl limit sets a general limit on the compactness of a general relativistic static fluid sphere, whose density does not increase outwards [21].



## Chapter 6

# Non-radial pulsations of relativistic stars

Non-radial oscillations of neutron stars, although believed to emit only weak gravitational waves (at least in the absence of instabilities) are interesting sources for future gravitational wave detectors. In general, large amplitude oscillations of neutron stars, as they are expected to be generated especially during the formation process, are a nonlinear effect. In general relativity, however, most of the work on stellar pulsations which has been done so far, relies on the linearization of the general relativistic fluid equations around the equilibrium model of the star. The spacetime of a nonrotating star in equilibrium is static and spherically symmetric. A general linear perturbation can be written as a sum of quasi-normal modes, that are characterized by the indices  $(l, m)$  of the spherical harmonic  $Y_{l,m}$ , i.e. an arbitrary scalar quantity  $A$  is decomposed as <sup>1</sup>

$$A(r, \theta, \phi) = \sum_{l,m} f_{l,m}(r) Y_{l,m}(\theta, \phi). \quad (6.1)$$

Furthermore, according to the radial dependence of the functions  $f_{l,m}(r)$ , we can define subclasses of the oscillation modes. The first such classification of the different pulsation modes goes back to Cowling [29]. In the following, we aim at giving a short overview of the different non-radial oscillation modes of neutron stars, when the stars are approximated by a polytropic EoS, thus neglecting effects like magnetic fields etc. The radial dependence of the oscillation is classified with respect to the restoring force. The fundamental mode ( $f$ -mode) is a coherent oscillation, with no oscillation nodes in the stellar interior (it is therefore often referred to as a surface mode). We use upper indices to denote the angular structure of the mode, e.g.  ${}^2f$  denotes the  $l = 2$  fundamental mode. As in the case of the pressure mode ( $p$ -mode), the restoring force for the fundamental mode is the pressure, which counterbalances gravity. In order to distinguish between the different pressure modes arising from different numbers of oscillation nodes, one uses subscripts  $p_1, p_2$  etc. Typical frequencies of the  $f$ -mode for neutron stars are of the order  $f \approx 1 - 2$  kHz, and  $f > 4$  kHz for the  $p$ -modes. Assuming, that the modes are damped only due to the radiation in gravitational waves, typical damping times  $\tau$  for the  $f$ -mode are  $\tau < 1$  s and  $\tau > 1$  s for the  $p$ -modes. The rotational mode ( $r$ -mode) has recently attracted a lot

---

<sup>1</sup>Assuming, that the perturbations respect the Killing coordinate  $\phi$  with surface-orthogonal trajectories, it suffices to consider the case  $m = 0$ .

of interest. The restoring force for the rotational mode is the Coriolis force. The mode has been shown to be generically unstable with respect to the Chandrasekhar-Friedman-Schutz mechanism [25, 46], and hence it is a promising source strong gravitational radiation. Finally, the gravitational wave mode ( $w$ -mode) is an oscillation mode of spacetime curvature with almost no matter movement. This mode is rapidly damped, typical damping times are of the order of  $\tau < 10^{-4}$  s. Here, we focus on the  $f$ -mode and  $p$ -modes only. More details on pulsations of relativistic stars can be found in [83, 143, 84] and references therein.

In order to show, that gravitational waves from oscillating relativistic stars can be detected with second or third generation gravitational wave detectors, Fig. 6.1 shows the sensitivity curve of several experiments along with the expected gravitational wave amplitude of the  $f$ -mode, the first  $p$ -mode and the  $w$ -mode.

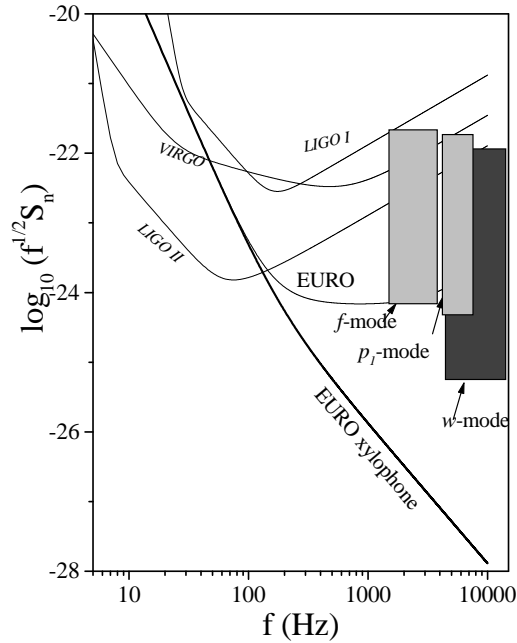


Figure 6.1: The spectral noise density for the new generation of laser interferometric gravitational wave detectors. The figure shows the sensitivity curves for the first generation detectors LIGO I and VIRGO, and for the second generation detector LIGO II. EURO is a third generation detector with idealized characteristics for gravitational wave astroseismology. The boxes represent the sensitivity needed to detect a mode into which an energy of  $10^{-6} M_{\odot} c^2$  is deposited. The upper limit of each box corresponds to an event in our galaxy and the lower limit to an event in the Virgo cluster. The figure was taken from [84].

Up to date, there are only few nonlinear simulations of non-radial pulsations of relativistic

stars. Most of the work was done in the so-called Cowling approximation, where the geometry of the spacetime is kept fixed (see e.g. [44, 41]). The importance of solving the field equations of general relativity along with the field equations of general relativistic fluid dynamics for the study of pulsations of relativistic stars can be already seen from the fact, that there are no  $w$ -modes in the Cowling approximation. A more detailed analysis shows [168] that the errors for the frequencies of the  $f$ -mode and the  $p$ -modes using the Cowling approximation can be up to 20% and more.

Along with the studies presented in [42], we present here the first studies of non-radial oscillations of relativistic stars solving the nonlinear field equations of general relativity and general relativistic fluid dynamics in axisymmetry. We focus our analysis on one specific stellar model. We choose a relativistic polytrope (2.52) with with adiabatic exponent  $\Gamma = 2$ , polytropic constant  $\kappa = 100$  and central density  $\rho_c = 1.28 \times 10^{-3}$  (in units in which  $c = M_\odot = G = 1$ ). This model, which has a mass of  $M = 1.4M_\odot$  has already been used in previous work [44, 41, 42], which allows us to compare our results for the radial frequencies and fixed background evolutions in axisymmetry.

## 6.1 The perturbations

Due to the discretization error introduced in the numerical solution of differential equations, different fluid modes will, in general, be excited in a numerical evolution of an equilibrium star. Here, in order to excite particular (non-radial) modes strongly, we further add deviations to the equilibrium model of the star in the initial data. In order to excite the radial oscillation modes of the star ( $l = 0$ ), we perturb the equilibrium configuration using the perturbation of density and pressure

$$\delta\rho = A\rho_c \sin\left(\frac{\pi r^2}{R^2}\right), \quad (6.2)$$

$$\delta p = \left(1 + \frac{1}{n}\right)p \frac{\delta\rho}{\rho}, \quad (6.3)$$

where  $A$  is the amplitude of the perturbation.

Additionally, to excite the  $l = 1, 2$  non-radial modes we perturb the meridional velocity component according to

$$u_y = A \sin\left(\frac{\pi r^2}{R^2}\right), \quad (6.4)$$

$$u_y = A \sin\left(\frac{\pi r^2}{R^2}\right) \cos\theta, \quad (6.5)$$

respectively. Fig. 6.2 shows the initial setup and a contour plot of the perturbation given by Eq. (6.5).

Following [44, 41], in order to determine the different oscillation modes, we analyze the time evolution of different (fluid and metric) variables at a fixed coordinate location. We have checked that the frequencies of the oscillation modes are largely independent of the specific location. Hence, for the results presented here, we restrict ourselves to extracting the frequencies at coordinates  $(x, y) = (\frac{\tilde{N}_x}{2}\Delta x, \frac{\tilde{N}_y}{2}\Delta y)$ , where  $\tilde{N}_x$  denotes the number of radial zones covering the

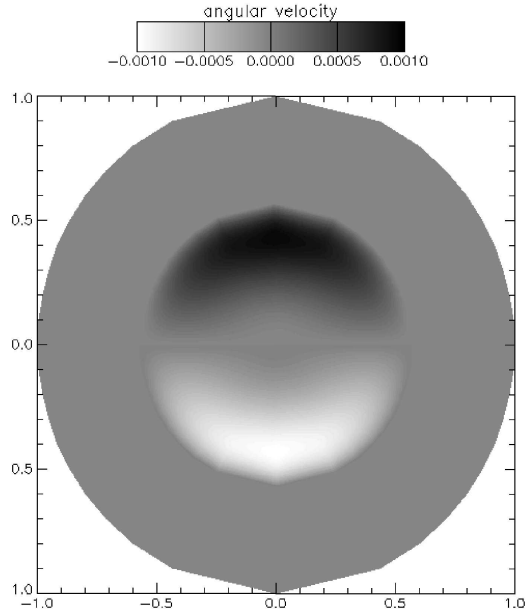


Figure 6.2: Contour plot of the meridional velocity perturbation  $u_y$ , Eq. (6.5). The axes labels denote the value of the radial coordinate  $x$  along the equator (horizontal axis) and the symmetry axis (vertical axis), and run from the origin of the coordinate system at  $x = 0$  to future null infinity  $\mathcal{J}^+$  at  $x = 1$ . The star corresponds to the inner circle, where the velocity perturbations are non-zero, with the north pole above.

star. In addition we use a radial coordinate

$$r = 15 \frac{x}{1 - x^4}, \quad (6.6)$$

and we choose a perturbation amplitude of  $A = 10^{-3}$ . We focus on the time evolution of the radial velocity  $u^x$  for the extraction of radial modes and on the meridional velocity  $u_y$  for the extraction of non-radial modes. The calculation of mode frequencies follows the work of [41], i.e. we determine the zeros of the first derivative of the Fourier transform. These zeros correspond to maxima in the Fourier transform which are associated with the excited modes of oscillation.

## 6.2 Fixed background evolutions

We start by presenting the results for the mode frequencies of the above stellar model obtained in evolutions in which we fix the background geometry of the spacetime (i.e. we adopt the Cowling approximation [29]). We compare the results to those in the literature, thus testing the hydrodynamics solver of our code.

Table 6.1 shows the results for the fundamental radial mode ( $F$ ) and the first three overtones  $(H_1 - H_3)^2$  and the  $f$  and  $p$  modes for both, the  $l = 1$  and  $l = 2$  perturbation. Our results are in

<sup>2</sup>The standard nomenclature of the radial modes differs from that of the non-radial modes. Instead of calling

Table 6.1: Mode frequencies obtained in the Cowling approximation for a relativistic polytrope with  $\kappa = 100$ ,  $n = 1$  and central density  $\rho_c = 1.28 \times 10^{-3}$  in units in which  $c = G = M_\odot = 1$ . The first column labels the different modes. The second column shows the frequencies obtained with our code, the third column the results obtained with a different nonlinear code based on Cauchy slices [41]. The fourth column indicates the frequencies obtained from a linear perturbation code [44] for the quadrupolar modes. The last column shows the relative difference between the present code and the results of [41] in percent.

Mode	Present Code [kHz]	Code [41] [kHz]	Perturbation [44] [kHz]	Difference [%]
$F$	2.690	2.706	-	0.59
$H_1$	4.636	4.547	-	1.96
$H_2$	6.532	6.320	-	3.35
$H_3$	8.418	8.153	-	3.25
${}^1f$	1.388	1.335	-	3.97
${}^1p_1$	3.504	3.473	-	0.89
${}^1p_2$	5.510	5.335	-	3.28
${}^1p_3$	7.400	7.136	-	3.70
${}^2f$	1.871	1.852	1.884	1.03
${}^2p_1$	4.143	4.100	4.110	1.05
${}^2p_2$	6.135	6.019	6.035	1.93
${}^2p_3$	8.087	7.867	7.873	2.80

good agreement (with an error smaller than 4% for each individual mode) with both, a different nonlinear code [41] and an independent linear code based upon perturbation theory [44]. There are several reasons which explain the observed differences: First, the angular grid resolution used in our simulations is rather low (we use resolutions with  $451 \times 21$  grid points in  $x$  and  $y$ , respectively) compared to the finer angular grids used in [41] ( $200 \times 80$ ). For the current setup - in contrast to [41] - only about one half of the radial zones is used to cover the star. We note that we use this choice here for comparisons with the results of the next section, where we also have to resolve gravitational waves in the exterior spacetime. Second, we have not implemented an atmosphere surrounding the star in [41], which enables the star to radially contract and expand. Therefore, the surface of the star may be too rigid, which may affect the mode frequencies slightly. Third, and perhaps most importantly, as described in Sec. 2.2 we use a second order reconstruction scheme at the cell interfaces, and not a third order scheme as in [41]. It is worth emphasizing the importance of using high-order schemes for the hydrodynamics in order to improve the frequency identification (see related discussion in [44]). Nevertheless, for our only purpose of assessing the validity of the code we think that the overall agreement found is satisfactory.

---

the radial modes  ${}^0f$ ,  ${}^0p_1$  etc., they are in general denoted as  $F$ ,  $H_1$  etc.

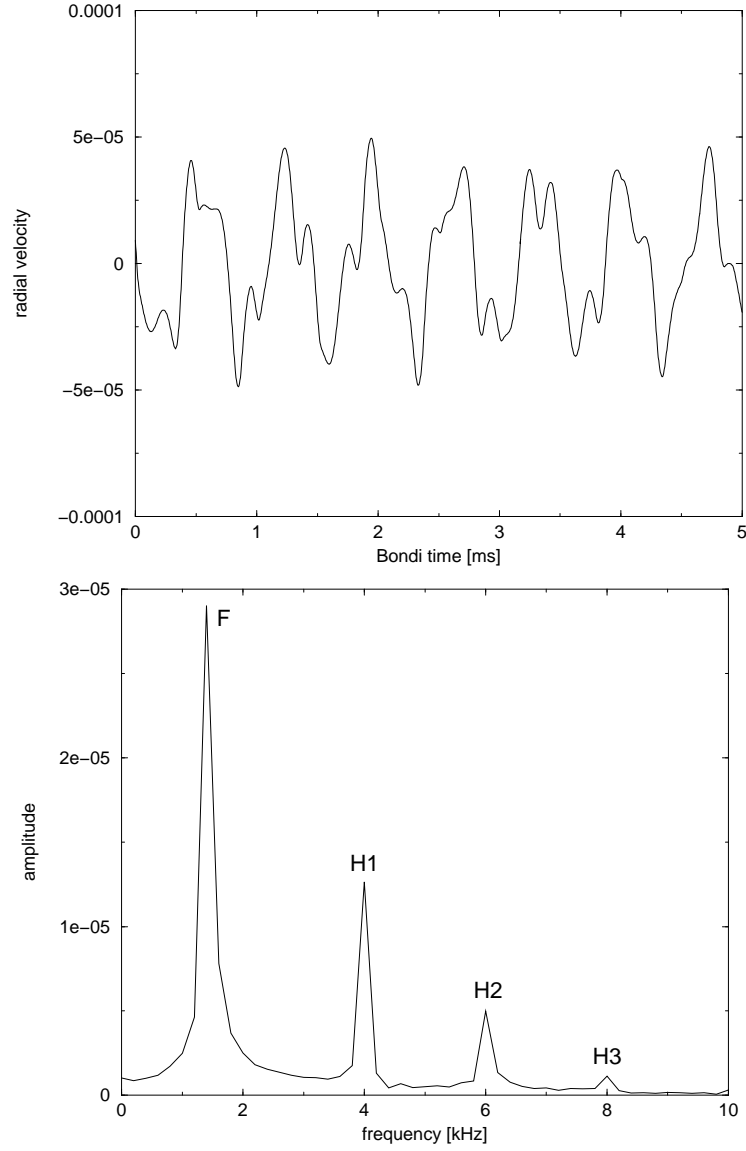


Figure 6.3: Pulsations of a  $\kappa = 100, n = 1, \rho_c = 1.28 \times 10^{-3}$  polytrope ( $c = G = M_\odot = 1$ ). Top panel: Time evolution of the radial velocity  $u^x$  for the  $l = 0$  perturbation. Bottom panel: Fourier transform of the radial velocity. We have labeled the different oscillation modes,  $F$  (fundamental) and  $H_1 - H_3$  (first three overtones).

### 6.3 Metric-fluid coupled evolutions

In this section we calculate the mode frequencies of the above stellar model from fully coupled evolutions of the fluid and the geometry. Apart from here (see also [138]), only in [42] non-radial pulsations of relativistic stars have been studied in general relativity using a time dependent evolution of the Einstein-perfect fluid system. Analyzing oscillations of relativistic stars in the characteristic approach has never been accomplished before.

Fig. 6.3 shows the (Bondi) time evolution of the radial velocity  $u^x$  for the  $l = 0$  perturbation (top panel), as well as the Fourier transform of this quantity. In the same way, Figs. 6.4 and 6.5 display the meridional velocity evolution  $u_y$  and the Fourier transform for the  $l = 1$  and  $l = 2$  perturbation, respectively. The final evolution time in Figs. 6.3-6.5 corresponds to 5 ms. The distinctive oscillatory pattern depicted in these figures is mainly a superposition of the lowest-order normal modes of oscillation of the fluid. The high-frequency modes are usually damped fast by the intrinsic viscosity of the numerical schemes, and at late times the star mostly pulsates in its lowest frequency modes.

We summarize our results on the mode frequencies in Table 6.2. Note that due to the conservation of linear momentum the  $^1f$  mode does not exist in Fig. 6.4 [41]. As in the Cowling simulations of the previous section we also find good agreement when comparing to results of an independent nonlinear code [42] and to results of linear perturbation theory [42, 82]. The reasons mentioned above for the observed discrepancies are still valid here, together with the possible new errors introduced by the metric evolution.

Table 6.2: Mode frequencies obtained in the coupled evolution for the relativistic polytrope with  $\kappa = 100$ ,  $n = 1$  and central density  $\rho_c = 1.28 \times 10^{-3}$  in units in which  $c = G = M_\odot = 1$ . The first column labels the different modes. The second column shows the frequencies obtained with our code and the third column shows the results obtained from linear perturbation theory [42, 82]. The last column shows the deviations in percent.

Mode	Present Code [kHz]	Perturbation [42], [82] [kHz]	Difference [%]
$F$	1.422	1.442	1.38
$H_1$	3.993	3.955	0.96
$H_2$	6.021	5.916	1.77
$H_3$	7.968	7.776	2.46
$^1p_1$	1.951	-	-
$^1p_2$	2.844	-	-
$^1p_3$	5.019	-	-
$^2f$	1.587	1.579	0.51
$^2p_1$	3.748	3.710	1.02
$^2p_2$	5.811	5.689	2.14
$^2p_3$	7.848	7.580	3.54

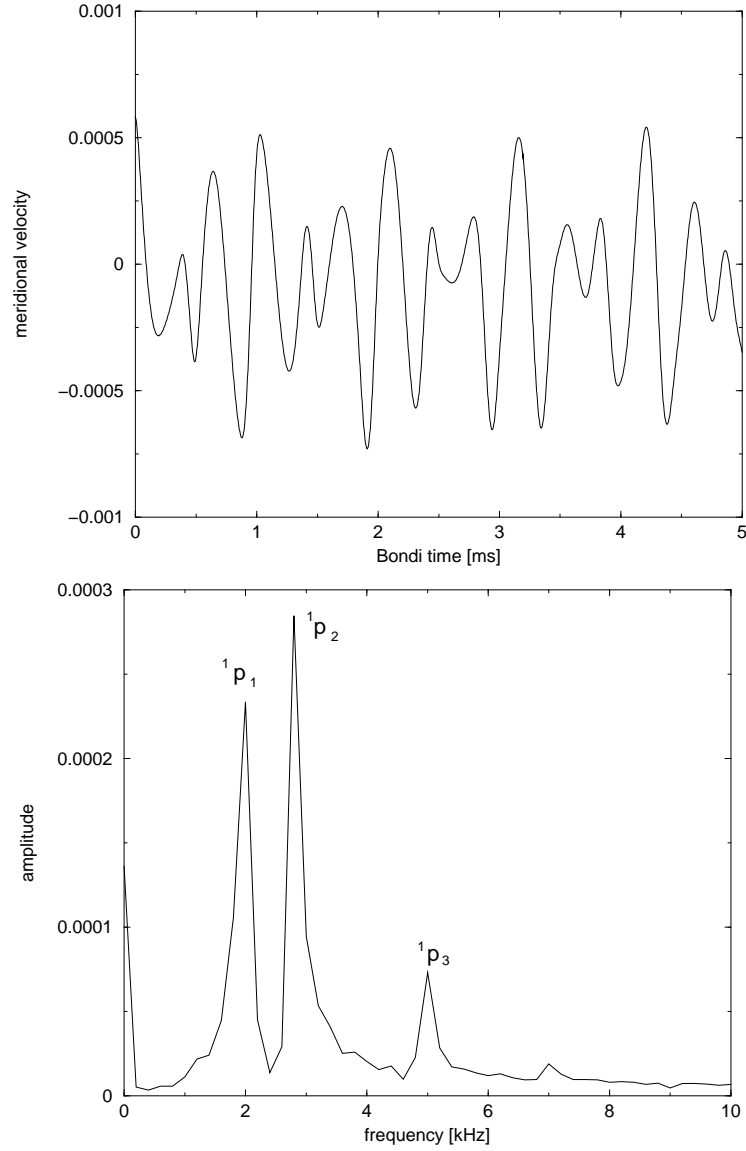


Figure 6.4: Pulsations of a  $\kappa = 100$ ,  $n = 1$ ,  $\rho_c = 1.28 \times 10^{-3}$  polytrope ( $c = G = M_\odot = 1$ ). Top panel: Time evolution of the meridional velocity  $u_y$  for the  $l = 1$  perturbation. Bottom panel: Fourier transform of the meridional velocity.



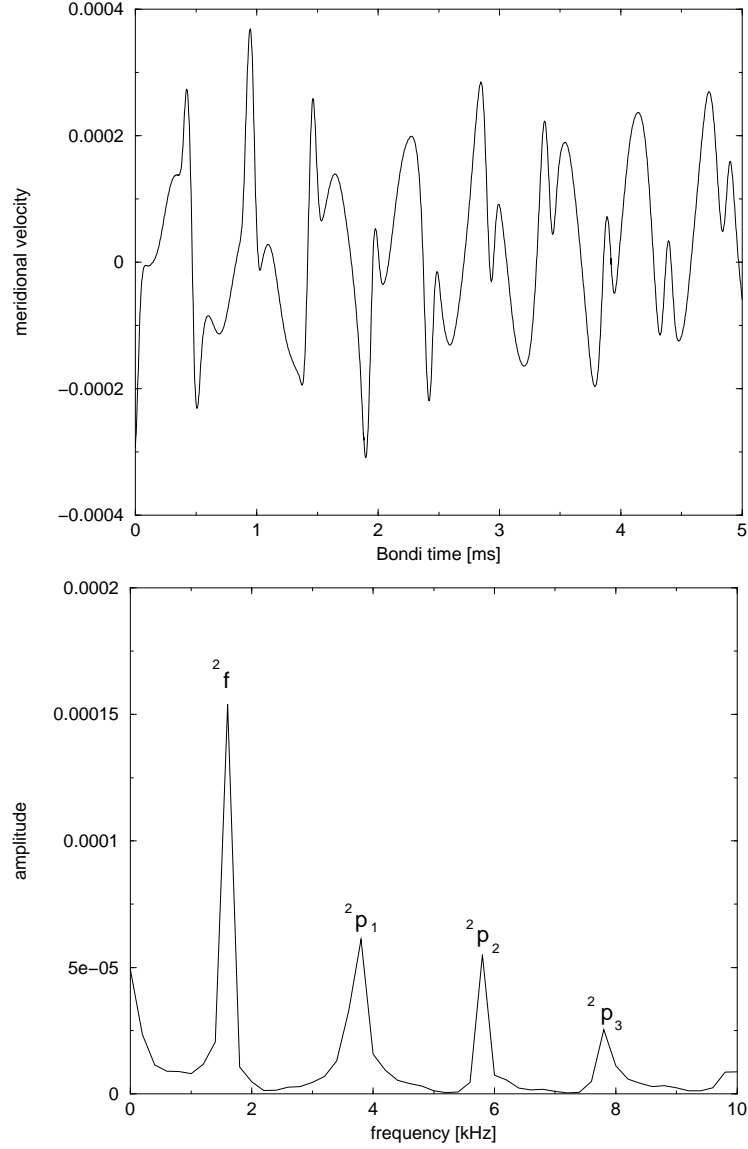


Figure 6.5: Pulsations of a  $\kappa = 100$ ,  $n = 1$ ,  $\rho_c = 1.28 \times 10^{-3}$  polytrope ( $c = G = M_\odot = 1$ ). Top panel: Time evolution of the meridional velocity  $u_y$  for the  $l = 2$  perturbation. Bottom panel: Fourier transform of the meridional velocity.

## 6.4 Gravitational waveform

Gravitational waves from oscillating neutron stars are likely to be detected by future gravitational wave detectors. If the detectors reach the necessary sensitivity, the gravitational waves of pulsating stars are relatively easy to identify due to the inherent periodicity. Measuring the frequency and the typical decay of the different oscillation modes, one can in principle deduce the mass and the radius of the star, and thus the EoS [2, 88].

In this section we use our routines for the gravitational wave extraction in our numerical implementation to study the gravitational wave signal from pulsating relativistic stars. We study the gravitational wave signal from the simulations of the above section concerning the  $l = 2$  perturbation. In Fig. 6.6 we plot the Bondi news function at the equator  $N(y_B = 0)$  as a function of the observer time. Due to the equatorial plane symmetry inherent to the perturbation, which is conserved during the evolution, we have  $y_B(y = 0) = 0$ . This enables us to directly plot  $N(y = 0)$ , thus avoiding suitable interpolations for the wave extraction, which would be otherwise needed for the coordinate transformation to local Bondi coordinates.

In order to estimate the amplitude of the signal in Fig. 6.6 we have also computed the gravitational wave emission due to the quadrupole formula Eq. (2.89)

$$N_0 = \ddot{Q}. \quad (6.7)$$

In contrast to Sec. 2.3.2, in order to account for all gravitating masses, we have included the contribution of the internal energy  $\epsilon$  to the quadrupole moment,

$$Q = \pi \sin^2 \theta \int_0^R dr' \int_0^\pi \sin \theta' d\theta' r'^4 \rho (1 + \epsilon) \left( \frac{3}{2} \cos^2 \theta' - \frac{1}{2} \right). \quad (6.8)$$

In our specific case, the internal energy gives rise to a 4% increase of the quadrupole news amplitude. In the numerical calculation of  $Q$  we equate the radial and angular coordinates  $r'$  and  $\theta'$  with the radial and angular coordinates  $r$  and  $\theta$ . Having included  $\epsilon$  into the integral, it is not possible to use the continuity equation to eliminate one time derivative. In order to avoid the numerical noise introduced by the three time derivatives in Eq. (6.7) we thus fit a cosine to the time evolution of the quadrupole moment  $Q$  obtained in the numerical simulation. The dashed line in Fig. 6.6 shows the third time derivative of this curve, where the time derivatives are taken with respect to Bondi time.

By evaluating the contributions of the gravitational wave signal in Fig. 6.6, we see that the dominant contribution originates from the  ${}^2f$  mode. The frequency we extract from the waveform is 1.57 kHz, in good agreement with the result shown in Table 6.2. There are additional contributions to the gravitational wave signal. The  ${}^1p_1$  mode is excited at the stellar surface, where we do not allow the star to radially contract or to expand.

Comparing the amplitude of the Bondi news and the “quadrupole news” Eq. (6.7) for the  ${}^2f$  mode we stress that the amplitudes roughly agree. We cannot exclude that the differences are mainly due to numerical errors. Due to the different contributions of the time derivative for  $\gamma$  and of gauge terms the calculation of  $N$  is a difficult task [76]. In addition, we note that the total energy radiated away corresponds only to a tiny fraction of the total mass of the spacetime. More precisely, whereas the total mass of spacetime is  $1.4M_\odot$ , the total mass radiated is only  $2.8 \times 10^{-9}M_\odot$ , which is smaller than the typical numerical errors in the determination of the Bondi mass. Moreover, most of this radiation is a consequence of the initial gravitational wave content and is radiated away between  $u_B = 0$  ms and  $u_B = 0.1$  ms. Additional differences in

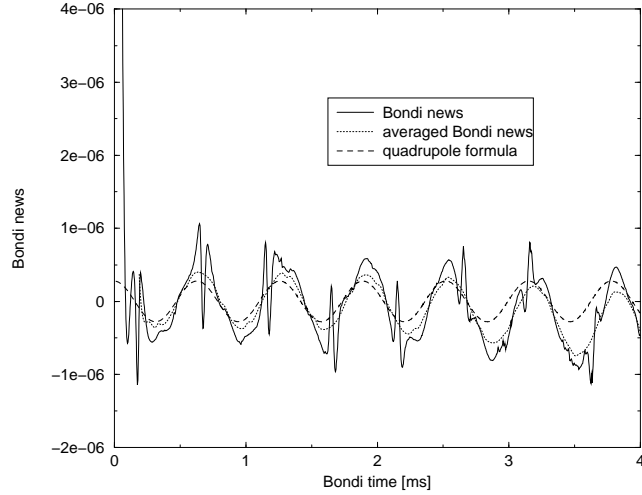


Figure 6.6: News function as a function of observer time at the equator at infinity. The (unphysical) initial part of the signal is due to the gravitational wave content in the initial data. The main oscillation frequency corresponds to the  ${}^2f$  mode with other frequencies overlaid. The main curve shows a suitable average of the numerical Bondi news smearing out higher frequencies. The dotted curve shows a suitable average of the numerical Bondi news smearing out higher frequencies. The average is calculated for a time interval of 0.3 ms. The dashed line corresponds to the estimated news of the  ${}^2f$  mode oscillation which is extracted using the quadrupole formula. See text for a detailed discussion.

the curves for the Bondi news and the quadrupole news in Fig. 6.6 might be caused by the rough estimate of the quadrupole  $Q$  in Eq. (6.8) which does not take into account the curvature of spacetime.

At late times (after about 3 ms), the Bondi news does not strictly oscillate around zero. This numerical effect can be weakened using more sophisticated numerical methods for the fluid update (e.g. third-order cell reconstruction procedures). We note that similar drifts are reported in [44, 42] in time evolutions of equilibrium models using a perfect fluid EoS. For the results shown in Fig. 6.6, we have used a polytropic EoS during the fluid evolution. This is legitimate as the effect of heating is negligible for our stellar object close to equilibrium. Finally, we note that the maximum deviation from global energy conservation, Eq. (2.79), in this simulation is  $2.5 \times 10^{-5} M_{\odot}$ , which is very adequate for the long integration time.



## Chapter 7

# Simulation of supernova core collapse

Supernova core collapse marks the final stage of the stellar evolution of massive stars. According to order of magnitude estimates, the total energy emitted in gravitational waves in such events can be as high as  $10^{-6} M_{\odot} c^2$ . Hence, supernovae are an important source of gravitational waves which could be detected with current or next generation gravitational wave laser interferometers. If detected, the gravitational wave signal could be used to probe the models of core collapse supernovae and to study the formation of neutron stars.

Since the collapse of the iron core and its bounce at nuclear densities is a complicated dynamical process, an adequate numerical description is demanding. As described in Chapter 2, we do not aim at modeling the microphysics in detail, but we take into account instead the most important features only. We use the hybrid EoS described in Sec. 2.2.2 to model the stiffening of the EoS at nuclear densities and the effects of thermal heating due to the presence of a shock. At the same time we focus on a fully general relativistic description of the collapse and bounce in axisymmetry.

### 7.1 Initial models

In the final stage of the stellar evolution of massive stars, the iron core in the stellar center has a central density of about  $\rho_c = 10^{10} \text{ g cm}^{-3}$  (see Fig. 1.4). As the pressure of the degenerate electrons is by far the most important contribution to the total pressure, the pressure in the iron core can be approximated by a polytropic equation of state Eq. (2.52) with adiabatic exponent  $\Gamma = \frac{4}{3}$ . In order to obtain an initial model for the iron core, we solve the Tolman-Oppenheimer-Volkoff equation (2.62) - (2.63) with the above central density, which corresponds to a central density of  $\rho_c = 1.6206 \times 10^{-8}$  in code units  $c = G = M_{\odot} = 1$ .

To initiate the gravitational collapse of a  $\Gamma = \frac{4}{3}$  relativistic polytrope (either perturbed or in equilibrium), we set the adiabatic index  $\Gamma_1$  in the hybrid EoS (2.60) to a value of 1.30, which mimics the softening of the EoS due to capture of electrons by iron group elements and due to the endothermic photodisintegration of heavy nuclei (see Eq. (1.1)). The chosen value is within the interval range analyzed in previous studies of rotational supernova core collapse based on Newtonian physics [169] and on the conformal flat metric approximation of general

relativity [31, 32]. A detailed parameter study of the influence of varying the adiabatic index  $\Gamma_1$  in the collapse dynamics is beyond the scope of the present analysis.

As we have not included rotation into the characteristic field equations of general relativity and the general relativistic fluid equations, the equilibrium initial model of the iron core is spherically symmetric. Furthermore, in the evolution of these data, spherical symmetry is conserved, i.e. during collapse, bounce and beyond. Therefore, as we are mainly interested in the core collapse as a source of gravitational waves, we add non-radial perturbations on top of the spherical data. Our analysis is thus restricted to collapse scenarios where the effects of rotation can be neglected and in which stellar evolution has led to asymmetries in the iron core, e.g. due to convection. The strongest gravitational wave signals are expected for perturbations of quadrupolar form. Hence, we further restrict our analysis to this case, varying the form and amplitude of the perturbation in the initial data. We note that the evolution of such data, however, can produce an arbitrary type of perturbation within the class of the imposed symmetry. We have classified the different models as follows:

- $\mathfrak{A}$ : the spherical model is unperturbed.
- $\mathfrak{B}$ : we prescribe a perturbation of the rest mass density

$$\delta\rho = A\rho_s \sin\left(\frac{\pi r^2}{R^2}\right)y^2, \quad (7.1)$$

where  $\rho_s$  denotes the spherical density distribution.

- $\mathfrak{C}$ : we prescribe a perturbation of the meridional velocity component

$$u_y = A \sin\left(\frac{\pi r^2}{R^2}\right)y. \quad (7.2)$$

Here,  $A$  is a free parameter describing the amplitude of the perturbation, and  $R$  denotes the radius of the iron core ( $R = 1.4 \times 10^3$  km). Note that we have already used a perturbation of the form  $\mathfrak{C}$  to study quadrupolar oscillations in relativistic stars, see Eq. (6.5) (Chapter 6). In the following, we have further classified models  $\mathfrak{B}$  and  $\mathfrak{C}$  according to the amplitude  $A$  of the perturbation. We have summarized the collapse models described in this Chapter in Table 7.1.

Table 7.1: Numerical models for the supernova core collapse. We have classified the models according to whether no perturbation was added to the spherical model (Type  $\mathfrak{A}$ ), a perturbation of the form Eq. (7.1) was added (Type  $\mathfrak{B}$ ) or a perturbation of the form Eq. (7.2) was added (Type  $\mathfrak{C}$ ).

model	amplitude $A$
$\mathfrak{A}$	-
$\mathfrak{B}001$	0.01
$\mathfrak{B}005$	0.05
$\mathfrak{B}01$	0.1
$\mathfrak{C}01$	0.1

One of the principal challenges of a numerical simulation of core collapse supernovae is the large radial extension to be covered by the computational domain. In our simulations, we

need a high radial resolution in order to obtain the converged result for the global dynamics. Moreover we extend the numerical grid to cover future null infinity for the extraction of gravitational waves. In all simulations described in this Chapter we used a radial grid function  $r = 100 \tan(\frac{\pi}{2}x)$ , the number of radial zones ranging from 450 – 800.

## 7.2 The dynamics of core collapse supernovae

We turn now to describe the dynamics of the iron core collapse we obtain from our numerical simulations.

### 7.2.1 Collapse and bounce

When evolving in time the initial models described in the previous section, the core starts to collapse. Fig. 7.1 shows the time evolution of the central density for model  $\mathfrak{B}01$ . When reaching nuclear density, the pressure increases strongly according to Eq. (2.55). The central density grows further, but its increase is soon stopped. Afterwards, it drops below its maximum value, finally approaching a quasi-equilibrium supra-nuclear value when a “proto-neutron star”<sup>1</sup> has formed in the central region.

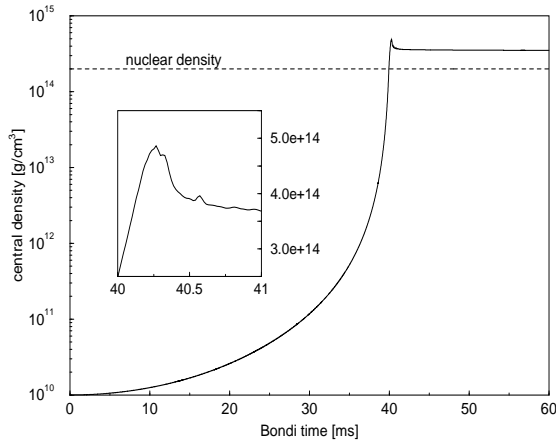


Figure 7.1: Evolution of the central density for the collapse model  $\mathfrak{B}01$  using a semilogarithmic scaling. During the collapse phase the central density increases by 4.5 orders of magnitude. When reaching supra-nuclear densities, the collapse is stopped as a consequence of the stiffening in the hybrid EoS at about 40 ms after the collapse was initiated. The central density finally approaches a new equilibrium supra-nuclear value. Shortly after bounce, oscillations appear in the central density, which can be seen from the inset (note the linear scaling).

Fig. 7.2 shows a spacetime diagram for the core collapse simulation of model  $\mathfrak{A}$  (the main aspects are similar for all our models). At the beginning of the collapse phase, the spacetime metric is close to the Minkowski metric, which is reflected in the diagram by the light cones being almost parallel straight lines. The effects of curvature can be most strongly seen close

<sup>1</sup>We use this term loosely, without claiming that we model the microphysics realistically.

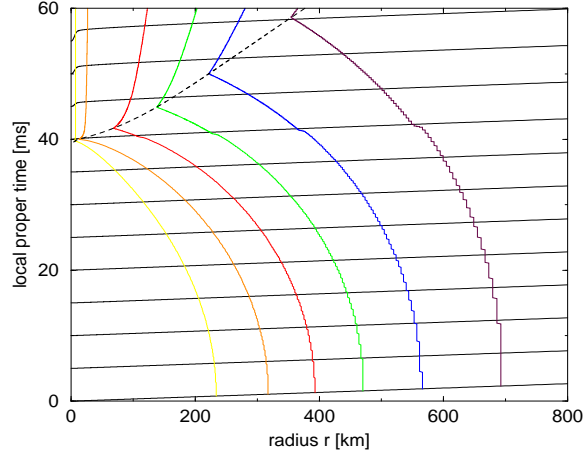


Figure 7.2: Spacetime diagram for the collapse model  $\mathfrak{A}$ . Plotted is the lapse of proper time as a function of the radial coordinate  $r$ . The black solid lines correspond to a subset of the light curves by which we foliate the spacetime (there is one light cone after every 5 ms, where time is measured by an observer at the origin). The colored curves correspond to different mass shells:  $M = 0.2M_{\odot}$  (yellow),  $M = 0.4M_{\odot}$  (orange),  $M = 0.6M_{\odot}$  (red),  $M = 0.8M_{\odot}$  (green),  $M = 1.0M_{\odot}$  (blue) and  $M = 1.2M_{\odot}$  (violet). After about 40 ms, a shock forms in the interior region close to the origin. This shock travels out, thereby transferring momentum to the infalling matter, which results in an outflow of material after the shock has passed. The location of the shock front is shown by the thick dashed line in the diagram. The diagram was obtained from a global simulation with 800 radial zones, extending the grid to future null infinity.

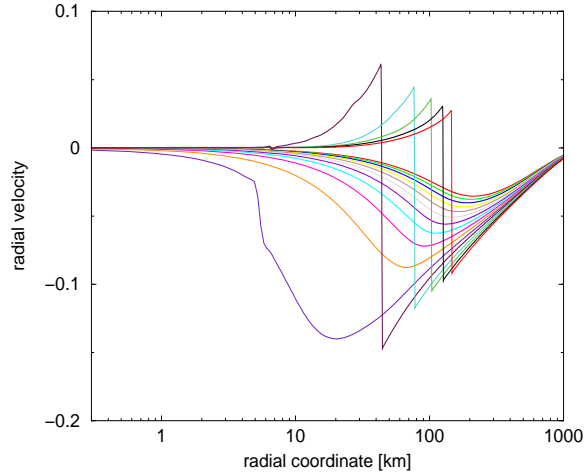


Figure 7.3: Snapshots of radial velocity profiles  $u^r$ , plotted as function of radius  $r$  for the collapse model  $\mathfrak{A}$ . The snapshots were taken between  $u_B = 30$  ms and  $u_B = 45$  ms, with a delay of 1 ms between subsequent outputs. The shock formation takes place at about 40 ms. In the outer part of the plotted region, the infall velocity of matter increases monotonically with time. For the simulation, we used 800 radial zones.



to the origin ( $r = 0$ ) after about 40 ms, when the proto-neutron star has formed. However, in comparison to the studies presented in the previous chapters, the forming neutron star is less compact. We observe a redshift factor  $e^{2H}$  relating the lapse of local proper time at the origin to the lapse of proper time at infinity of  $\sim 1.12$ . The diagram shows different mass shells and the location of the shock front (the dashed line). In order to localize the shock front, we search for coordinate locations with  $u_i^x - u_{i+1}^x \geq s$ , where  $s$  is a threshold value for a velocity jump to be adapted (typical values for our simulations are  $s = 10^{-5} \dots 10^{-4}$ ). In order to calculate the mass inside a fixed radius, we have made use of Eq. (5.22) with a perfect fluid stress energy tensor. For collapse model  $\mathfrak{A}$ , the general expression for the Bondi mass, Eq. (2.70), reduces to this simple form.

Fig. 7.3 shows different snapshots of the radial velocity  $u^r$  at evolution times close to bounce. In the late phases of the collapse, a homologous inner core can be distinguished. In this region, the infall velocity measured as function of radius is proportional to the radius. The homologous inner core shrinks with time. The outer limit of the homologous region, i.e. the sonic point, where the local sound speed has the same magnitude as the infall velocity, finally reaches a radius of less than 10 km after about 40 ms. At that time, a shock front forms, which moves outwards with a speed of  $\sim 0.1c$  initially. During its propagation it is gradually slowed down by the interaction with the infalling material in the outer region. It is worth to stress the ability of the code to resolve the steep shock front with only a few grid points (typically three). This can be further seen in Fig. 7.4, where we have plotted the rest mass density  $\rho$  at the shock front for a simulation of the collapse model  $\mathfrak{C}01$ .

The propagation of the shock front to the exterior through the infalling material heats the matter substantially. This can be seen in Fig. 7.5, where we plot the internal energy distribution  $\epsilon$  in the central region shortly after bounce. The figure further shows the contribution to the internal energy from the polytropic part, Eq. (2.56), and the thermal part, Eq. (2.59). In the very central region, the polytropic contribution constitutes the dominant part of the internal energy. In contrast, the thermal energy dominates the total internal energy in the post-shock region for radii larger than a certain value,  $\sim 13$  km in the specific situation shown in Fig. 7.5.

We have verified that in the global simulations of core collapse supernovae, the energy balance given by Eq. (2.79) is well preserved. Typical maximum values for the deviation from energy conservation are of the order of  $0.5 - 1\%$  for the simulations described in this section.

Figures 7.6 - 7.7 show various contour plots illustrating the collapse and bounce dynamics for the collapse model  $\mathfrak{B}01$ . For this particular simulation we used a resolution  $(N_x, N_y) = (600, 12)$ . Fig. 7.6 shows contour plots of the rest mass density covering the iron core up to a radius of 400 km at times 40 ms (i.e. at bounce), at 45 ms (when the shock has reached a radius of  $\sim 140$  km) and at 50 ms (when the shock wave has reached a radius of 250 km). We have plotted velocity vectors on top of the contour plots, normalized to the maximum velocity in the displayed region. After shock formation, the velocities in the inner region are small compared to the infall velocities of the core. Fig. 7.7 focuses on the inner region up to a radius of 30 km. In the collapse phase up to bounce at nuclear densities (upper panel), the initial aspherical contributions do not play a major role, the radial infall velocities dominate the dynamics. After bounce (middle and lower panel) the forming neutron star in the central region shows non-spherical oscillations, with fluid velocities up to about  $2 \times 10^{-3}c$ . Qualitatively, the dynamics for the collapse model  $\mathfrak{C}01$  is very similar to what is shown in Figs. 7.6-7.7 for model  $\mathfrak{B}01$ . However, the particular form of the non-spherical pulsations created after bounce differs.

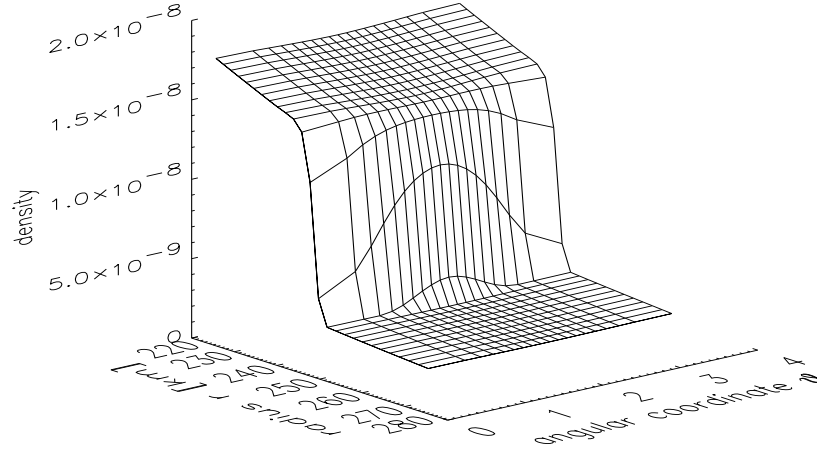


Figure 7.4: Rest mass density distribution  $\rho$  around the shock front for the collapse model  $\mathfrak{C}01$ . 50 ms after initiating the collapse, the shock has reached a radius of about 250 km. The figure shows a surface plot of the corresponding region, as a function of the radial coordinate  $r$  and the angular coordinate  $\theta$ . We plot every radial zone using a radial grid  $r = 100 \tan(\frac{\pi}{2}x)$  with 450 radial zones. The shock front is resolved with only three radial zones. The aspherical nature of the data is most prominent at the shock front.

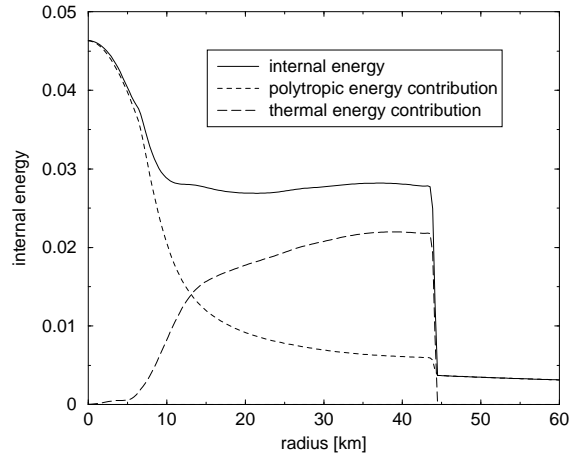


Figure 7.5: Radial distribution of the internal energy  $\epsilon$  (solid line) shortly after bounce ( $u_B = 41$  ms) for the collapse model  $\mathfrak{A}$ . The different contributions from the polytropic part  $\epsilon_p$  (dashed line) and the thermal part  $\epsilon_{th}$  (long-dashed line) to the total internal energy are also shown. In front of the shock which is located at a radius of  $\sim 45$  km, the thermal energy vanishes.

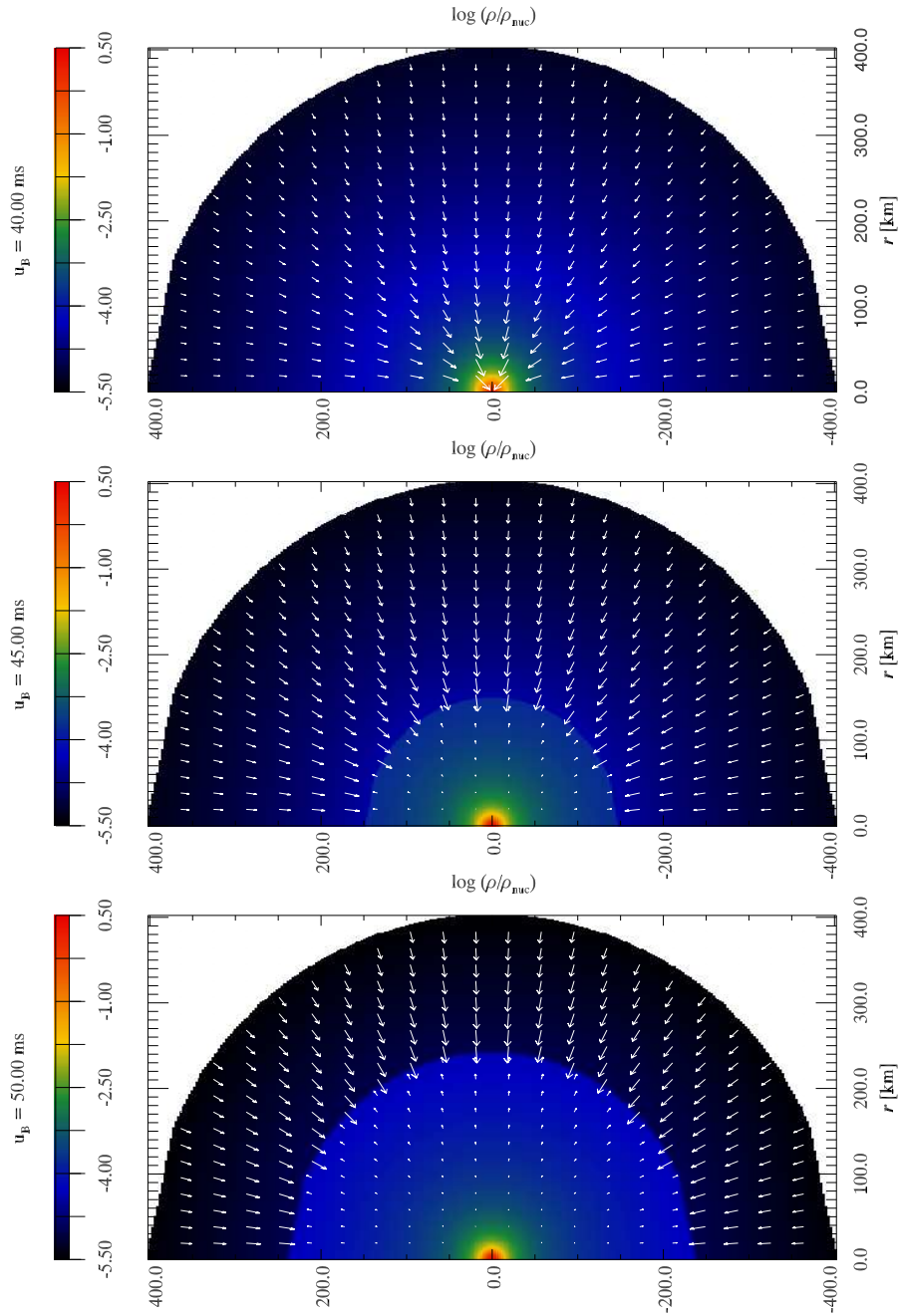


Figure 7.6: Contour plot of the rest mass density distribution for model  $\mathfrak{B}01$  at a Bondi time  $u_B = 40$  ms (upper panel),  $u_B = 45$  ms (middle panel) and  $u_B = 50$  ms (lower panel), obtained from a global evolution extending the grid to future null infinity. We only show a fraction of the core up to a radius of 400 km. Overlaid are velocity vectors. The fluid dynamics after bounce (middle and lower panel) is dominated by the outgoing shock (located at a radius of 140 km and 250 km respectively).

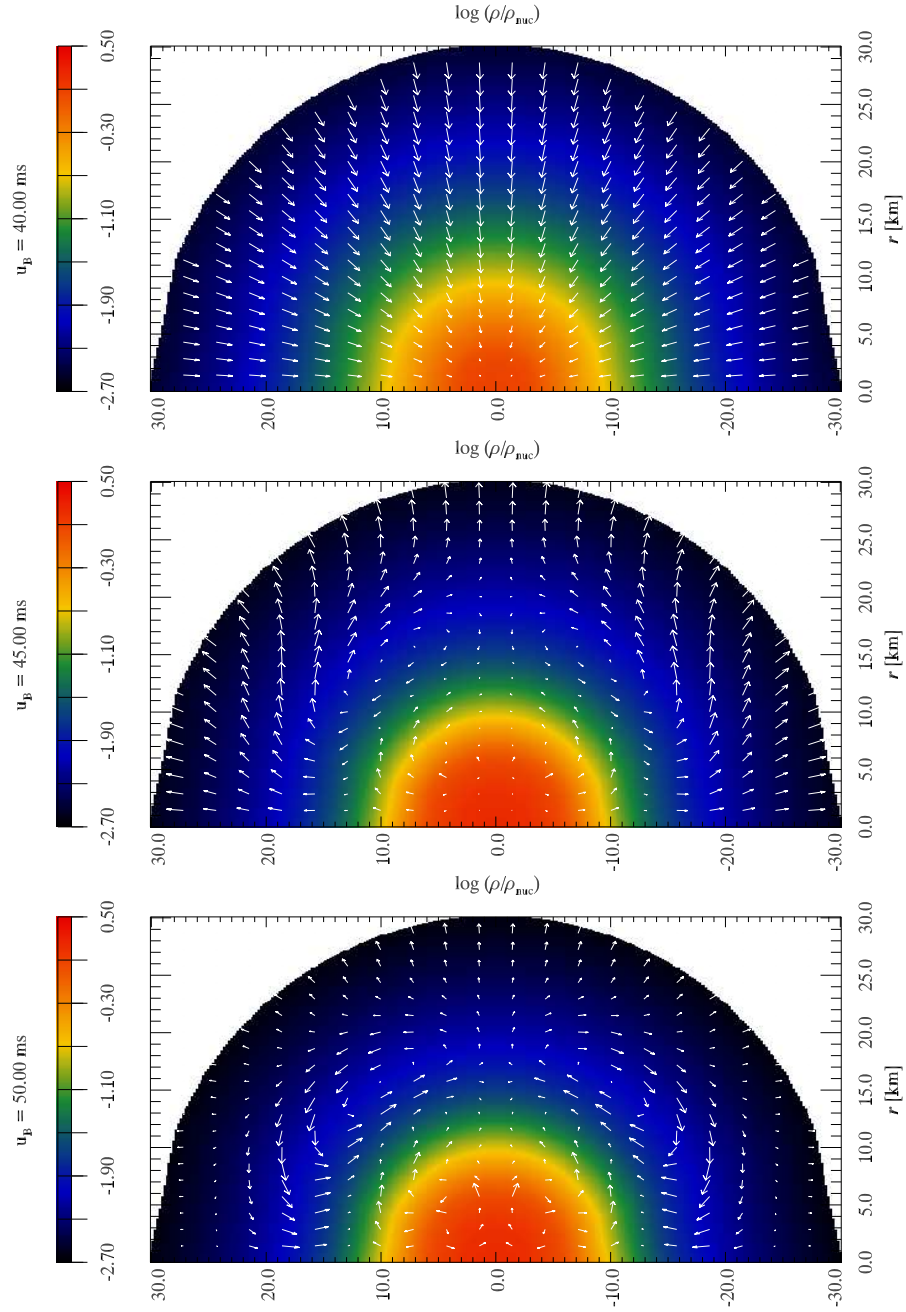


Figure 7.7: Same as Fig. 7.6, but focusing on the inner region of the iron core up to a radius of 30 km. At bounce (upper panel), the dynamics is well approximated by the spherical dynamics. In the later phases (middle and lower panels), the fluid dynamics is characterized by aspherical flows related to the oscillations of the newborn neutron star. The matter flow shows reflection symmetry with respect to the equator, which is inherent to the initial data and well preserved during the evolution.

### 7.2.2 Fluid oscillations in the outer core

When analyzing the dynamic behavior of the fluid after bounce, we found that the meridional velocity oscillates strongly in the entire region in front of the shock. This can be seen in the solid curve of Fig. 7.8, where we plot the meridional velocity component  $v_2 = ru^\theta$  for model  $\mathfrak{B}01$  at coordinate location  $r = 833$  km and  $y = 0.5$  as a function of Bondi time. Similar oscillations are observed in the entire region in front of the shock, where they are created directly after the formation of the proto-neutron star in the central region of the numerical domain. The only possibility to propagate information instantaneously (i.e. on a slice with constant retarded time  $u$ ) from the central region to the outer layers of the iron core is through the metric, since sound waves would need several 10 ms to cover the distance. There are two possible explanations for these oscillations. Either they are created when gravitational wave energy is absorbed in the region well in front of the shock, or they are created by our choice of coordinates, i.e. they are gauge effects. In the latter case, the oscillations would not be caused by a real flow, but as a consequence of the underlying coordinate system in which we describe the flow.

To clarify the origin of the oscillations, we estimate in the following the kinetic energy of the oscillations, assuming that they are a physical effect. From Fig. 7.8, the average amplitude of the oscillation<sup>2</sup> is of the order of  $\hat{v}_2 = 2 \times 10^{-4}c$ . Taking into account that the total mass in the pre-shock region is of the order of  $M_{ps} \approx 1M_\odot$ , the value of the kinetic energy in the oscillations is approximatively

$$E_{kin} \approx \frac{1}{2}M_{ps}(\hat{v}_2)^2 \approx 2 \times 10^{-8}M_\odot c^2. \quad (7.3)$$

This energy is comparable to the total energy radiated in gravitational waves in a typical core collapse supernova. Transferring such an amount of energy to the pre-shock region seems unphysical, as gravitational waves interact with matter only very weakly. Instead, as we describe next, we conclude that the oscillations are mainly introduced by our choice of coordinates.

Following the work of Bishop et al. [11] inertial coordinates can be established at future null infinity  $\mathcal{J}^+$ . The angular inertial coordinate  $\theta_B$  can be constructed solving the partial differential equation

$$(\partial_u + U\partial_\theta)\theta_B = 0, \quad (7.4)$$

with initial data  $\theta_B(u = 0) = \theta(u = 0)$ . Instead of solving the partial differential equation (7.4) directly, we determine the characteristic curves of Eq. (7.4)

$$\frac{d\theta}{du} = U(\theta, u), \quad (7.5)$$

$$\theta(u = 0) = \theta_B, \quad (7.6)$$

along which  $\theta_B$  is constant. With suitable interpolations,  $\theta_B$  can then be determined for arbitrary angles  $\theta$ .

Making use of Eq. (7.4), it is possible to define an “inertial” meridional velocity

$$u^{\theta_B} = \frac{\partial\theta_B}{\partial\theta}\Big|_u^{\mathcal{J}^+} (u^\theta - U)\Big|_u^{\mathcal{J}^+} u^u. \quad (7.7)$$

---

<sup>2</sup>Note that  $v_2$  vanishes at the polar axis and at the equator, so that the average velocity is substantially smaller than that shown in Fig. 7.8.

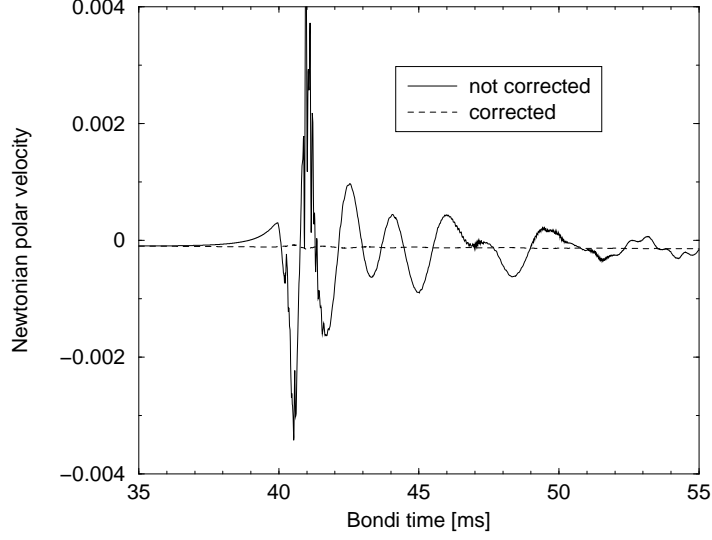


Figure 7.8: Meridional velocity component as a function of Bondi time at the fixed location  $r = 833$  km and  $y = 0.5$  for model  $\mathfrak{B}01$ . The radial location was chosen well in front of the shock. The solid line corresponds to the meridional velocity as extracted in our coordinate system,  $v_2 = ru^\theta$ , in units of the speed of light  $c$ . The dashed line corresponds to the meridional velocity evaluated in inertial Bondi coordinates defined at future null infinity. See text for more details.

The dashed line in Figure 7.8 shows the corrected (“inertial”) angular velocity  $ru^{\theta_B}$ . Remarkably, the oscillations have almost disappeared, which clearly shows that gauge effects can play a major role for the oscillations in the pre-shock region.

## 7.3 Gravitational waves from core collapse supernovae

After having described the global dynamics, we focus the discussion on the gravitational waves obtained from our simulations of supernova core collapse.

### 7.3.1 Quadrupole gravitational waves

There are two possibilities of calculating the gravitational wave strain  $A_{20}^{E2}$  defined in Eq. (2.95) from the quadrupole moment (see the discussion in Sec. 2.3.2). Either the quantity is directly calculated from the quadrupole moment  $Q$  (see Eq. (2.88)) according to Eq. (2.95) - (2.96), i.e.,

$$A_{20}^{E2} = \frac{16}{\sqrt{15}} \pi^{\frac{3}{2}} \frac{d^2}{du_B^2} \left[ \int_0^R dr' \int_0^\pi \sin \theta' d\theta' r'^4 \rho \left( \frac{3}{2} \cos^2 \theta' - \frac{1}{2} \right) \right], \quad (7.8)$$

or, alternatively, using the first moment of momentum formula in order to eliminate one time derivative analogous to the transition from Eq. (2.89) to Eq. (2.92), i.e.,

$$A_{20}^{E2} = \frac{16}{\sqrt{15}} \pi^{\frac{3}{2}} \frac{d}{du_B} \left[ \int_0^R dr' \int_0^\pi \sin \theta' d\theta' r'^3 \rho (v_1 (3 \cos^2 \theta' - 1) - 3v_2 \sin \theta' \cos \theta') \right]. \quad (7.9)$$

As shown in Fig. 7.9 we find good agreement between the two approaches. In order not to have the time derivatives dominated by numerical noise, we have averaged the quantities in brackets in Eq. (7.8) and Eq. (7.9) over a few neighboring grid points before calculating the time derivatives. This result checks the implementation of the continuity equation, and as

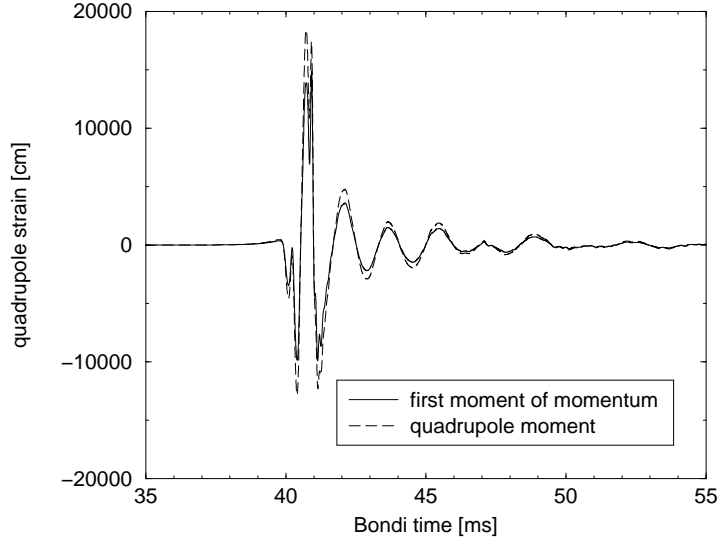


Figure 7.9: Gravitational wave strain  $A_{20}^{E2}$  for the simulation of the collapse model  $\mathfrak{B}01$ . The solid curve shows the result using the first moment of momentum approach Eq. (7.9), the dashed line is based on Eq. (7.8). The good agreement found between both approaches shows that our general relativistic fluid evolution is internally consistent.

this equation is not calculated separately, but as a part of a system of balance laws, our implementation of the fluid equations in general. We note that the equivalence between Eq. (7.8) and Eq. (7.9) is only strictly valid in the Minkowskian limit and for small velocities, which is the origin for the observed small differences between the curves in Fig. 7.9. Substituting  $\rho$  by  $\rho u^u e^{2\beta}$  in Eq. (7.8) and by  $\rho e^{2\beta}$  in Eq. (7.9), by which we restore the equivalence in a general relativistic spacetime, we find excellent agreement between the two approaches of calculating  $A_{20}^{E2}$ .

Since we are imposing only small perturbations from spherical symmetry, we expect a linear dependence of the non-spherical dynamics and the gravitational wave signal as a function of the perturbation amplitude. We have verified in a series of runs that the amplitude of the quadrupole moment (and thus the quadrupole radiation signal) scales linearly with the amplitude of the initial perturbations (see Fig. 7.10). This observation marks another important test for the correctness of the global dynamics of our code.

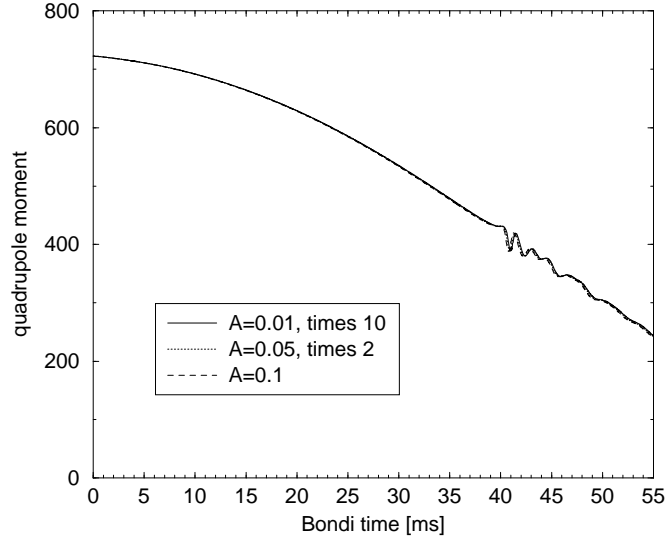


Figure 7.10: Quadrupole moment (in units  $c = G = M_{\odot} = 1$ ) as a function of time for three models of type  $\mathfrak{B}$  with perturbation amplitude  $A = 0.01$ ,  $A = 0.05$  and  $A = 0.1$ . The first two results are rescaled with respect to  $A = 0.1$  assuming a linear dependence. All three curves overlap in the diagram. The quadrupole moment (and hence the quadrupole signal) scales linearly with the amplitude of the perturbation in the chosen parameter region.

On the other hand, when comparing the quadrupole news given by Eq. (2.89) with the Bondi news signal evaluated at future null infinity, Eq. (2.77), we find important differences. This can be seen in Fig. 7.11, where we plot both, the Bondi news and the quadrupole news for model  $\mathfrak{B}01$ . We note that the differences manifest themselves not only in the amplitude of the oscillations, but also in the frequencies of the signals. This behavior is clearly different from the one observed in the neutron star pulsation studies in Sec. 6.4, where both signals showed good agreement. As already mentioned in Sec. 2.3.2, the quadrupole radiation term is only the first term in a post-Newtonian expansion of the gravitational wave signal. By extracting the hexadecapole moment for the above result, we found, however, that the associated amplitude is too small in order to explain the observed differences in Fig 7.11.<sup>3</sup>

As we have explained in detail above and in Sec. 4.3, the global dynamics of the core collapse and bounce is correctly reproduced with our numerical code. We have strong evidence that the quadrupole signals extracted from our collapse simulations do not correspond to physical gravitational wave signals. In the following, we describe the different arguments which support the above claim.

First, if the quadrupole radiation signal corresponded to the true physical signal, it would be very difficult to understand why the Bondi signal has a significantly smaller amplitude. In the calculation of the Bondi news, Eq. (2.77), the contribution of the different terms are relatively large and add up to a small signal (see the discussion in the next section). Under the

<sup>3</sup>In general, one would expect that the contribution of the hexadecapole moment increases the amplitude of the approximate signal. Note that here, however, the amplitude of the quadrupole news in Fig 7.11 is much larger than that of the Bondi news evaluated at  $\mathcal{J}^+$ .



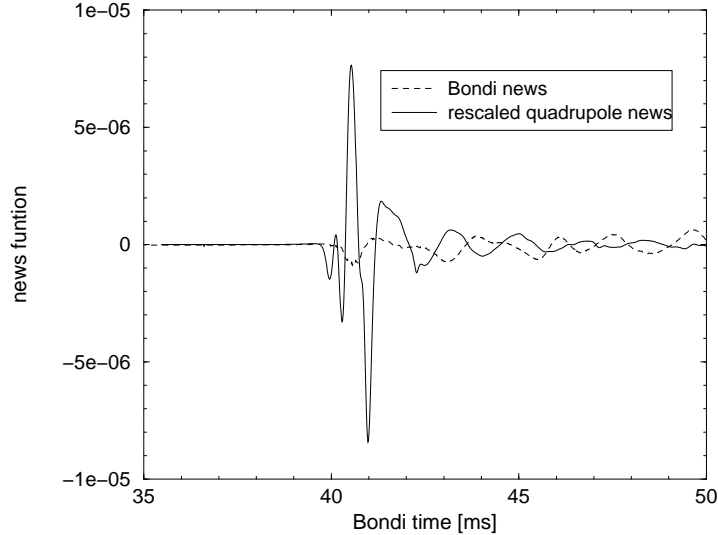


Figure 7.11: Bondi and quadrupole news as a function of time for model  $\mathfrak{B}01$ . The dark solid curve corresponds to the quadrupole news according to Eq. (2.92), the dashed curve to the Bondi news signal. For visualization reasons, we have divided the quadrupole news result by 50. We do not find agreement between the Bondi news and the quadrupole news.

assumption that the quadrupole news signal is correct and the Bondi news signal is wrong, it would be extremely unlikely that the possible errors in the contribution to the Bondi news add up to a very small signal.

Second, we have performed comparisons between our numerical code and the code of [31], finding much larger amplitudes for the quadrupole gravitational wave signal in our case. However, we note that comparing the results of both codes in axisymmetry is ambiguous, as possible differences might have different explanations. For example, the use of the conformally flat metric approach in [31] is clearly an approximation to general relativity, which should create some differences. Furthermore, the coordinate systems used in both codes for the computation of the quadrupole moment are different. Only in our code, the quadrupole moment is evaluated on a light cone, i.e. as a function of retarded time.

A third and physically motivated argument stems from the spatial distribution of matter in our simulation. As it can be seen from Fig 7.12, the main contribution in the radial integral of the quadrupole moment comes from the outer, infalling layers of matter. These outer layers are responsible for the oscillations in the quadrupole moment, which can be seen in Fig. 7.10. Following the reasoning of the last section it is natural to conclude that the calculation of the quadrupole moment is also affected by our choice of coordinates, i.e. by gauge effects.

For all these reasons we extract the quadrupole moment in the angular coordinate system defined by Eq. (7.4). However, introducing the inertial angular coordinate does not help to find better agreement between quadrupole and Bondi signals, the extracted quadrupole moment almost agrees with the results shown in Fig. 7.10. Since the difference of Bondi time between the different angular directions on our Tamburino-Winicour foliation is in general of the same order as the lapse of time for one time step, we expect a similar result when evaluating the

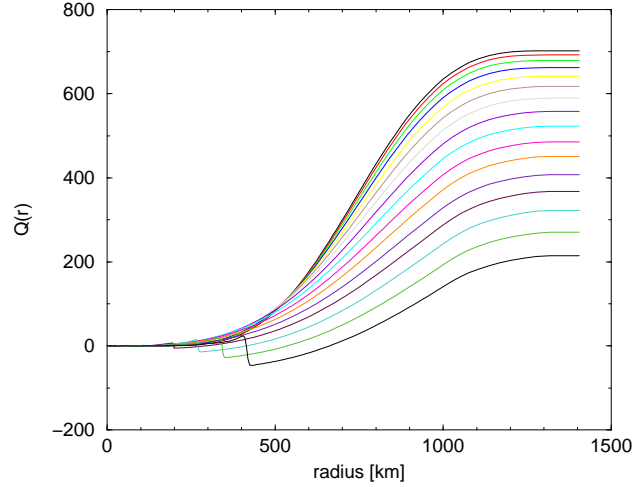


Figure 7.12: Radial contribution to the quadrupole moment. We plot the value of the integral  $Q(r) = \pi \sin^2 \theta \int_0^r dr' \int_0^\pi \sin \theta' d\theta' r'^4 \rho(\frac{3}{2} \cos^2 \theta' - \frac{1}{2})$  as a function of the radial coordinate  $r$  for different values of time. The data is plotted after a fixed number of time steps, starting with initial data at  $u_B = 0$  ms. The data was taken from a simulation of the supernova core collapse model  $\mathfrak{B}01$ . Large amplitude oscillations of the quadrupole moment, as they can be seen in Fig. 7.10, can only be created - at least shortly after bounce - in the outer region of the infalling matter well in front of the shock.

quadrupole moment at a fixed inertial time. However, by prescribing the necessary coordinate transformations to define Bondi coordinates only at  $\mathcal{J}^+$ , we do not take into account an inertial radial coordinate, which should be used for the evaluation of the quadrupole moment.

As we have discussed in detail in Sec. 6.4, we find good agreement between the Bondi signal and the quadrupole signal when calculating gravitational waves from pulsating relativistic stars. Hence the obvious question of why the quadrupole formula can be applied in the studies of neutron star pulsations arises. We think, this is mainly a consequence of the small velocities in the problem of neutron star pulsations. Whereas the typical maximum fluid velocities in the oscillation problem are of the order of  $10^{-5}c - 10^{-4}c$ , fluid velocities of up to  $0.2c$  are reached for the supernova core collapse. Furthermore, due to the non-spherical dynamics of the proto-neutron star formed in the interior of the collapsed region, the metric can pick up gauge contributions which are created as a consequence of our requirement to prescribe a local Minkowski frame at the vertex of the light cones. Gauge contributions may also play a more important role in the collapse scenario due to the enlarged radial extension of the collapsing iron core (about 1500 km), which is much larger than the corresponding one for neutron star pulsations (about 15 km).

We note that since the collapse involves fluid velocities of up to  $0.2c$ , it is not obvious whether the functional form for the quadrupole moment established in the slow motion limit on the light cone will still be valid. In fact, the situation could be similar to the case of the

total mass of spacetime, where a naive definition, even in spherical symmetry, as

$$M_n = 4\pi \int_0^R r'^2 \rho(1 + \epsilon) dr', \quad (7.10)$$

would only be a valid approximation for small fluid velocities. This can be understood from the comparison with the expression of the Bondi mass, Eq. (5.22), in the form

$$M_B = 4\pi \int_0^R r'^2 [\rho(1 + \epsilon)(-u^u u_u) - p(1 + u^u u_u)] dr', \quad (7.11)$$

(no summation is involved in this expression). Only vanishing fluid velocities, i.e.  $u^u u_u = -1$ , ensure that the two masses are equal,  $M_n = M_B$ .

We experimented with possible alternative functional forms for the quadrupole moment which brings up the existence of significant differences (see Fig. 7.13). An unambiguous clarification of which functional form has to be used for the quadrupole moment in the extended regime of validity of large fluid velocities could only be obtained by a derivation of the quadrupole formula in the Tamburino gauge. However, technical complications for such a derivation are so severe that it has only been accomplished for a simplified radiating dust model [75] (see the related discussion in Winicour [161]).

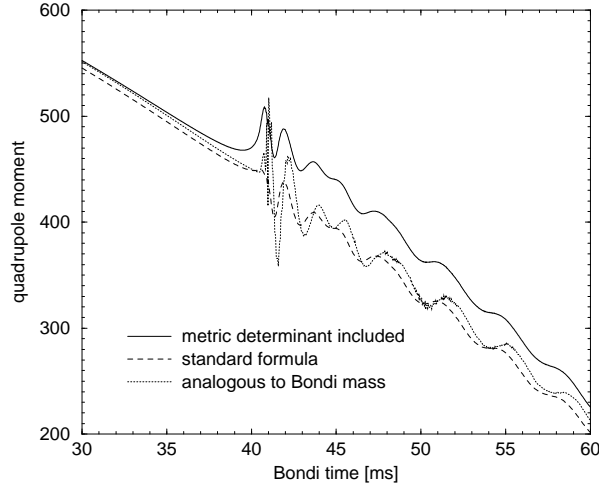


Figure 7.13: Time evolution of the quadrupole moment for slightly different definitions, which all have the correct weak field, slow motion limit. The dashed curve corresponds to the original quadrupole moment according to Eq. (2.88). The solid line corresponds to the quadrupole moment after substituting  $\rho$  by  $\sqrt{-g}\rho$  in Eq. (2.88). Finally, the dotted curve was obtained by substituting  $\rho$  by  $e^{2\beta}T_{ru}$ , a choice motivated by Eq. (5.22).

### 7.3.2 The Bondi news signal

The numerical extraction of the Bondi news is a very complicated undertaking, since reasons for possible numerical problems are diverse. First, its extraction involves calculating *non-leading*

terms from the metric expansion at future null infinity (see the discussion in Sec. 2.3.1). All the metric quantities are global quantities, and are thus sensitive to any numerical problem in the entire computational domain. Second, when calculating the gravitational signal in the Tamburino-Winicour approach, one has to take into account gauge effects. For the present calculations of the gravitational wave signal from core collapse, the gauge contributions are indeed the *dominant* contribution, which can easily influence the physical signal.

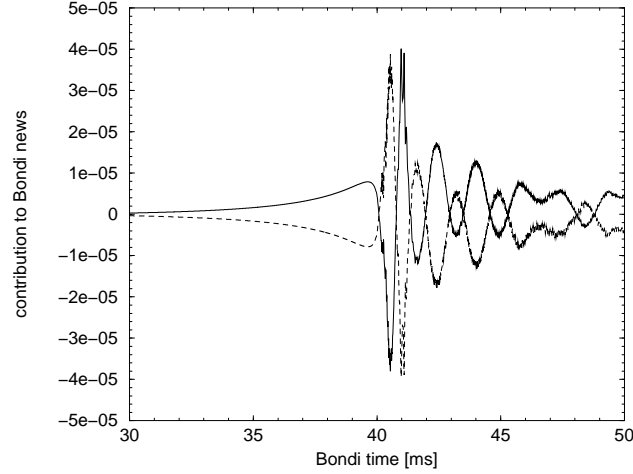


Figure 7.14: Different contributions to the Bondi news. The solid curve corresponds to the term involving  $c_u$  (first addend) in Eq. (2.77), the dashed curve to the contribution from the second and third addend. By summing up both contributions we obtain the Bondi news, which is close to zero. In addition, we note that when separating the third addend into angular derivatives of  $H$  and  $\omega$ , each single contribution has an amplitude 23 times larger than what is shown in the figure.

In order to stress these points, we plot in Fig. 7.14 the different contributions to the Bondi news for the collapse model  $\mathfrak{B}01$ . As it can be seen in this figure, the metric quantities show high frequency numerical noise, as soon as the shock forms at bounce (at a Bondi time of about 40 ms). In order to demonstrate that the noise is actually created at the shock, we plot in Fig. 7.15 the location of the shock together with the gravitational wave signal. Obviously the noise is created by the motion of the shock across the grid, the temporal behavior of the noise following the discontinuous jumps of the shock between adjacent grid cells. We would like to point out that due to the smaller radial resolution used in the outer layers of the core, the frequency of the noise slowly decreases with time.

As we have pointed out in the previous section, the shock front is well captured in only a few radial zones with our high-resolution shock-capturing scheme. It might seem surprising that a small localized error created in a few radial zones can have such a large effect on the gravitational wave signal. However, one has to keep in mind that the radial integration of the metric variables picks up this error and propagates it to future null infinity instantaneously. It is important to stress that the effect of the numerical noise on the dynamics of the collapse and bounce is negligible. However, the gravitational wave signal, i.e. the Bondi news, is extremely sensitive to it.

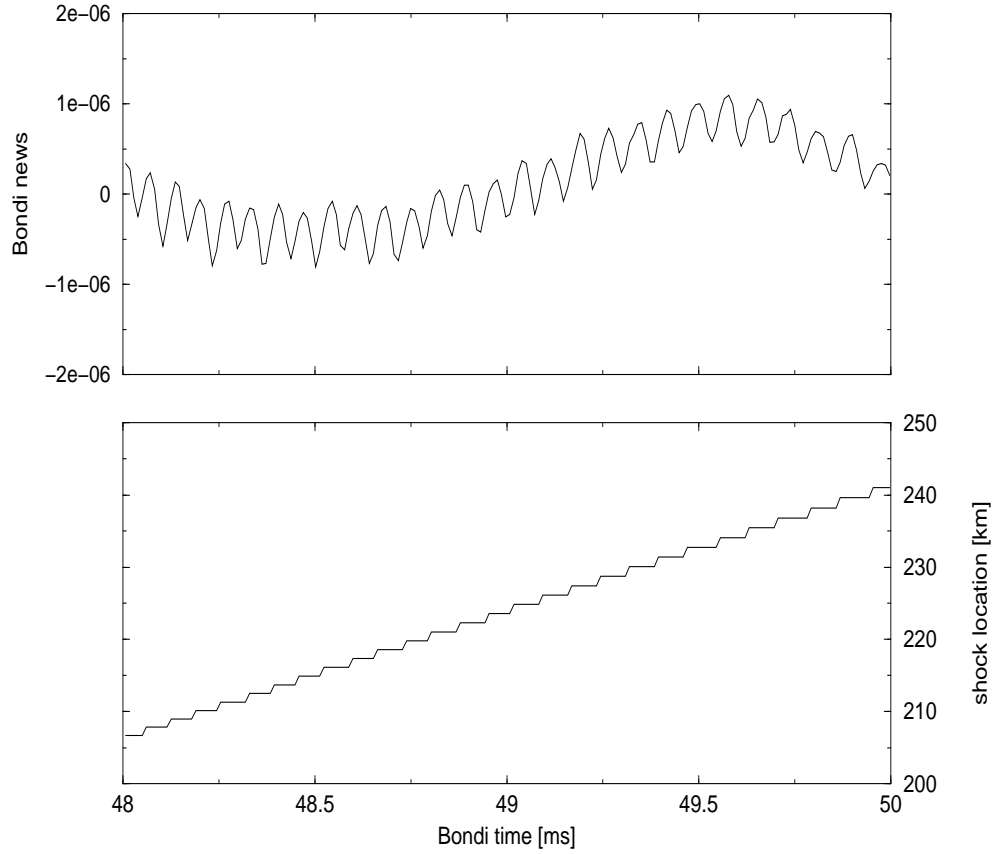


Figure 7.15: Upper panel: Bondi news as a function of time. High frequency noise is overlaid on top of a small frequency modulation. Lower panel: Radial location of the cross section of the shock front with the equator as a function of time. Due to the finite resolution, the location of the shock wave moves discontinuously. Finding the same frequency for the noise in the Bondi news, we have established that the noise is created at the shock, and propagated instantaneously to infinity in the numerical solution of the metric equations.

We have verified, that the frequency of the noise - as expected - increases with radial resolution. Unfortunately, the amplitude of the noise does not decrease substantially with radial resolution, at least not in the resolution regime accessible to us.<sup>4</sup> Therefore, we have tried to eliminate the noise by different methods. In a first attempt, we tried to smooth out the shock front, either in the hydrodynamical evolution itself or before using the fluid variables in the source terms of the metric equations. In both cases, it was impossible to obtain a smooth signal without changing the dynamics. In a second attempt, we rearranged the metric equations eliminating second derivatives which might be ill-behaved at the shock.<sup>5</sup> Defining a metric quantity

$$X = r^2 f^2 e^{2(\gamma-\beta)} \hat{U}_{,x} - 2(\beta_{,y} - \bar{y} \hat{\gamma}_{,y}), \quad (7.12)$$

and solving the hypersurface equations successively for  $\beta$ ,  $X$ ,  $U$  and  $S$  it is possible to eliminate all second derivatives from the hypersurface equations. Unfortunately, the noise is not affected by this rearrangement of the metric equations. Third, going to larger time steps for the fluid evolution only - solving the metric equations several times between one fluid time step - did not reduce the noise. After these attempts we decided to eliminate the noise from the gravitational wave signals only after the numerical evolution. We experimented with two different smoothing methods. In the first method, we calculate the Fourier transform of the data, and eliminate all frequencies beyond a certain threshold frequency (of about 5 - 10 kHz). When transforming back from Fourier space afterwards, all the high-frequency part of the data is removed. In a second method we simply average the signal over a few neighboring points. We have applied this second method in what is described below.

Fig. 7.16 shows the Bondi news signal for the collapse model  $\mathfrak{B}01$ . The figure focuses on the part of the signal around bounce. After the initial gravitational wave content is radiated away (in the first 5 ms, not depicted in the figure), the signal in the collapse stage is very weak. This is expected, as the dynamics is well reproduced by a spherical collapse model during this stage. At the bounce, the Bondi news shows a spike. Afterwards, a complicated series of oscillations is created due to the oscillation of the forming neutron star and the propagation of the shock to the exterior. Typical oscillation frequencies are of the order of 0.5 - 1 kHz, for which the maximum sensitivity is reached for the current gravitational wave laser interferometers (see Fig. 6.1).

Correspondingly, Fig. 7.17 shows the Bondi news signal for a the collapse model  $\mathfrak{C}01$ . Here again, after radiating away the initial gravitational wave content, the collapse phase is characterized by very small radiation of gravitational waves. At bounce, we again observe a strong spike in the signal. Afterwards, the oscillations in the signal are rather rapidly damped.

We stress that - as a consequence of the necessary smoothing techniques applied - only the main features of the gravitational wave signals in Figures 7.16 and 7.17 are reliably reproduced. This also applies to possible offsets of the Bondi news, which affect in particular the Bondi gravitational wave strain, Eq. (2.97). Comparing the Bondi news function for the different collapse models of type  $\mathfrak{B}$ , we observe to good approximation a linear dependence of the Bondi news with the perturbation amplitude. This is reflected in the total energy radiated away in

<sup>4</sup>For a resolution  $(N_x, N_y) = (600, 12)$ , one time step is accomplished in about 2 s of CPU time on the DEC-Alpha workstations where we run the simulations achieving a performance of several hundred MFlops. Taking into account that about  $7 \times 10^5$  time steps are needed to cover the evolution up to  $u_B = 50$  ms for this given resolution, one single simulation takes about 16 days.

<sup>5</sup>Note that only after rearranging the vacuum field equations, smooth results for the Bondi news are obtained in [55].

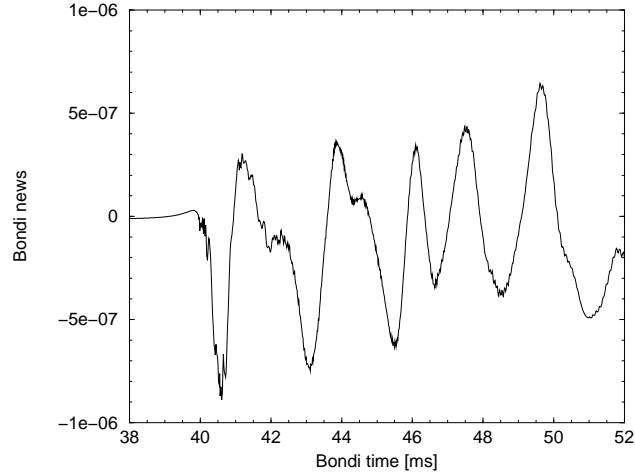


Figure 7.16: Bondi news as a function of Bondi time for the collapse model  $\mathfrak{B}01$ . The displayed time interval covers the late collapse stage until several ms after bounce. During the collapse stage, the gravitational wave signal is negligible. After bounce a complicated series of oscillations sets in.

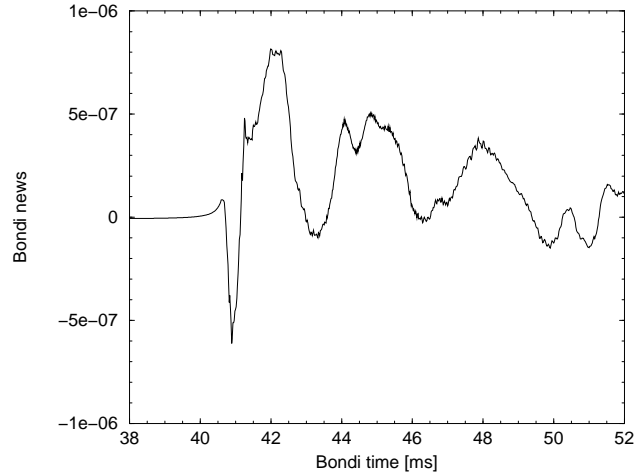


Figure 7.17: Bondi news as a function of time for the collapse model  $\mathfrak{C}01$ . The bounce at about 41 ms is characterized by a large spike in the gravitational wave signal. After bounce, the signal shows oscillations, with principal frequency of about 0.35 kHz.

gravitational waves, which scales quadratically with the amplitude of the initial perturbation. A summary of the results on the gravitational wave energy is listed in in Table 7.2.

Table 7.2: Total energy radiated in gravitational waves in the first 50 ms for the collapse simulations of type  $\mathfrak{B}$ . The initial gravitational wave content is the dominant contribution to the total energy. This energy scales quadratically with the amplitude of the initial perturbation, as can be inferred from the last column, where the corresponding energies have been rescaled with respect to the collapse model  $\mathfrak{B}01$ .

model	total energy radiated [ $M_{\odot}$ ]	rescaled result [ $M_{\odot}$ ]
$\mathfrak{B}001$	$4.305 \times 10^{-9}$	$4.305 \times 10^{-7}$
$\mathfrak{B}005$	$1.077 \times 10^{-7}$	$4.308 \times 10^{-7}$
$\mathfrak{B}01$	$4.322 \times 10^{-7}$	$4.322 \times 10^{-7}$

## 7.4 Summary

The work presented in this Chapter is pioneer in the use of the characteristic formulation of general relativity in simulations of supernova core collapse and in the extraction of the associated exact gravitational waves. Although our axisymmetric hydrodynamics code is accurate enough to allow for a detailed analysis of the global dynamics of core collapse in general, we have not found a robust method for the (Bondi news) gravitational wave extraction in the presence of strong shock waves. We note that, to the best of our knowledge, there is no further experience reported in the literature which could have guided us in our research.

Comparing our results to very recent existing work on relativistic supernova core collapse [30, 31], it is not surprising that numerical noise in the gravitational waveforms is more noticeable in our approach. Whereas in the conformal flat metric approach employed in [30, 31] the metric equations of general relativity reduce to elliptic equations, which naturally smooth out high-frequency numerical noise, we solve for the gravitational wave degrees of freedom directly using the full set of field equations of general relativity, and hence we have to solve a hyperbolic equation. It remains to be seen whether a similar numerical noise to the one we find when extracting the gravitational wave signal will be encountered in core collapse simulations solving the full set of Einstein equations in the Cauchy approach. In this respect we mention very recent axisymmetric simulations by Shibata using a conformal-traceless reformulation of the ADM system [135] where, despite of the fact that long-term rotational collapse simulations could be accurately performed, gravitational waves could not be extracted, even approximately, since the signals were entirely dominated by noise.

With the current analysis we have presented in this Chapter, it is not obvious how the numerical noise of the Bondi news can be effectively eliminated. Including rotation in the simulations, which would be the natural next step for a more realistic description of the scenario, could help in this respect. Due to the global asphericities introduced by rotation, one would expect, in general, gravitational wave signals of larger amplitude, which could make the numerical noise less important, if not completely irrelevant. In addition to this possibility we propose the following methods to improve our gravitational wave signals: In a first approach one should try



to rearrange the metric equations by introducing auxiliary fields which could effectively help to diminish the importance of high-order derivatives, especially of the fluid variables, which can be discontinuous. Unfortunately, to the best of our knowledge, there is no clear guideline to what is really needed to eliminate the numerical noise completely, apart from the hints given by [55]. Our attempts in this direction have not yet been successful, but we believe there is still room for improvement. Alternatively, one should try to implement pseudospectral methods for the metric update. Pseudospectral methods would allow a more efficient and accurate numerical solution of the metric equations. In a third promising line of research we propose to consider the inclusion of adaptive grids and methods of shock fitting into the current code. With the help of an adaptive grid, one could try to arrange the entire core collapse simulation in such a way that the shock front always stays at a fixed location of the numerical grid. By avoiding the movement of the shock front across the grid, one would expect the noise in the gravitational wave signals to disappear. But already increasing the radial resolution substantially in the neighborhood of the shock front could help to obtain an improved representation of the shock. All these issues are ripe for upcoming investigations.



## Chapter 8

# Conclusion and outlook

We have presented numerical algorithms to solve the coupled Einstein-perfect fluid system in axisymmetry. Our approach is based upon the characteristic formulation of general relativity in which spacetime is foliated with a family of outgoing light cones emanating from a regular center. Due to a compactification of the spacetime future null infinity is part of our finite numerical grid where we extract gravitational waves without approximation.

Applying the nonlinear, fully relativistic code to studies of neutron stars and gravitational collapse, it has successfully passed several tests, aimed at testing both the fluid evolution as well as the metric solver in the nonlinear regime. The code can accurately maintain long-term stability of neutron stars, and it can simulate supernova core collapse and bounce including strong relativistic shocks.

We have numerically analyzed the interaction of relativistic stars and scalar fields by means of nonlinear evolutions of the Einstein-Klein-Gordon perfect fluid system in spherical symmetry. We have built a sequence of stable, self-gravitating,  $\kappa = 100$ ,  $n = 1$  relativistic polytropes, increasing the central density from  $\rho_c = 1.5 \times 10^{-3}$  to  $3.0 \times 10^{-3}$  ( $G = c = M_\odot = 1$ ). Using a compactified spacetime foliation with outgoing null cones we have studied the fate of the relativistic stars when interacting with a sufficiently strong scalar field wave packet, as well as the dynamics and energetics of the process. We have found that by choosing a strong (finite amplitude) scalar field pulse with energy of the order of  $10^{-3} M_\odot$ , the relativistic star is either forced to oscillate in its radial modes of pulsations or to collapse to a black hole on a dynamical timescale. The fate of the star depends on its central density and, since we fix the polytropic equation of state, on its compactness. The energy transferred to the relativistic star increases with the compactness of the model. As the consequence of the interaction with the scalar field, depending on the compactness, we can distinguish between linear and nonlinear oscillations of the star, or finally gravitational collapse for the most compact objects. The radiative signals we have found consist of several quasi-normal oscillations and a late time power-law tail, in agreement with the results predicted by (linear) perturbation analysis of wave propagation in an exterior Schwarzschild geometry.

We have further applied the code to studies of neutron star oscillations. Modeling the neutron star by a relativistic polytrope with  $\kappa = 100$ ,  $n = 1$  and  $\rho_c = 1.28 \times 10^{-3}$  ( $G = c = M_\odot = 1$ ), we have extracted the frequencies of different radial and non-radial fluid modes both in evolutions fixing the spacetime geometry and in fully nonlinear simulations of the Einstein-perfect fluid system. Fixing the background geometry, we compare our results with

other nonlinear hydrodynamical codes, finding very good agreement. For the fully general relativistic simulations a comparison to linear perturbation studies was performed which further confirmed our results. We have also analyzed the gravitational wave signal arising in these time evolutions of perturbed stellar configurations. As expected, the quadrupolar fluid modes create the strongest radiation in gravitational waves. We have compared the gravitational wave signal extracted with the help of the quadrupole radiation formula and the exact gravitational wave signal extracted at future null infinity. Finding good agreement, we have thus established, that the application of the quadrupole radiation formula for the extraction of gravitational waves from (weakly) pulsating neutron stars is valid.

We finally applied our numerical code to studies of supernova core collapse. To this aim, we modeled the microphysics of the process approximately, focusing on a fully general relativistic treatment. We approximate the initial data of the iron core by a  $4/3$  polytrope with central density  $\rho_c = 10^{10} \text{ g cm}^{-3}$ , decreasing the adiabatic exponent to a value of 1.3 afterwards in order to initiate the collapse. Our equation of state takes into account the stiffening at nuclear densities and the effects of thermal heating from shock waves. During the collapse phase, the central density increases by almost 5 orders of magnitude, when the inner core bounces at supra-nuclear densities. A shock wave travels out from the central region, heating up the matter on its way out. In order to study the non-spherical dynamics, we add perturbations to the initial data. Whereas the collapse phase is well approximated by a spherical collapse, non-spherical oscillations are created after bounce, which cause the emission of gravitational waves. In our simulations we do not find agreement between the Bondi gravitational wave signal extracted at infinity and the gravitational wave signal extracted with the help of the quadrupole formula. We have strong evidence that the gravitational wave signal obtained from the application of the quadrupole formula is flawed by coordinate effects. The Bondi news function extracted at infinity after bounce show oscillations, typical oscillation frequencies for the dominant contribution being of the order of  $0.3 - 1 \text{ kHz}$ .

In this work, for the first time, we have studied relativistic stars and stellar collapse as sources of gravitational waves in the characteristic formulation of general relativity. In the future, it will be astrophysically very interesting to include rotation into the current characteristic code. Rotation introduces global asymmetries which can be responsible for strong gravitational wave signals. There are various applications of such a generalized code to studies of isolated compact objects as sources of gravitational waves, in particular supernova core collapse and the process of black hole formation. One should keep in mind that there is the well-founded hope, that gravitational waves will be “seen” for the first time in the near future.

# Bibliography

- [1] Allen, G., Andersson, N., Kokkotas, K. D., and Schutz, B. F., “Gravitational waves from pulsating stars: Evolving the perturbation equations for a relativistic star”, *Physical Review D*, **58**, 124012+, (1998).
- [2] Andersson, N., and Kokkotas, K. D., “Gravitational waves and pulsating stars: What can we learn from future observations?”, *Physical Review Letters*, **77**, 4134–4137, (1996).
- [3] Astone, P., and et al., “Search for gravitational wave bursts by the network of resonant detectors”, *Classical and Quantum Gravity*, **19**, 1367–1375, (2002).
- [4] Baade, W., and Zwicky, F., “Remarks on super-novae and cosmic rays”, *Physical Review*, **46**, 76–77, (1934).
- [5] Balberg, S., and Shapiro, S. L., “The properties of matter in white dwarfs and neutron stars”, in *Handbook of Elastic Properties*, Eds. H. E. Bass, V. M. Keppens, M. Levy and R. Raspert (Academic Press), (2002).
- [6] Bartnik, R., and Norton, A. H., “Numerical methods for the Einstein equations in null quasi-spherical coordinates”, *SIAM Journal of Scientific Computing*, **22**, 917–950, (2000).
- [7] Baumgarte, T. W., Shapiro, S. L., and Teukolsky, S. A., “Computing supernova collapse to neutron stars and black holes”, *The Astrophysical Journal*, **443**, 717–734, (1995).
- [8] Baumgarte, T. W., Shapiro, S. L., and Teukolsky, S. A., “Computing the delayed collapse of hot neutron stars to black holes”, *The Astrophysical Journal*, **458**, 680–691, (1996).
- [9] Belczynski, K., Kalogera, V., and Bulik, T., “A comprehensive study of binary compact objects as gravitational wave sources: evolutionary channels, rates, and physical properties”, *The Astrophysical Journal*, **572**, 407–431, (2002).
- [10] Bethe, H. A., and Wilson, J. R., “Revival of a stalled supernova shock by neutrino heating”, *The Astrophysical Journal*, **295**, 14–23, (1985).
- [11] Bishop, N. T., Gómez, R., Lehner, L., Maharaj, M., and Winicour, J., “High-powered gravitational news”, *Physical Review D*, **56**, 6298–6309, (1997).
- [12] Bishop, N. T., Gómez, R., Lehner, L., Maharaj, M., and Winicour, J., “Incorporation of matter into characteristic numerical relativity”, *Physical Review D*, **60**, 24005+, (1999).

- 
- [13] Bishop, N. T., Gomez, R., Holvorcem, P. R., Matzner, R. A., Papadopoulos, P., and Winicour, J., “Cauchy-characteristic matching: A new approach to radiation boundary conditions”, *Physical Review Letters*, **76**, 4303–4306, (1996).
- [14] Blanchet, L., “Gravitational radiation from post-Newtonian sources and inspiralling compact binaries”, *Living Reviews in Relativity*, **5**, 3, (2002).
- [15] Bloom, J. S., and et al., “Detection of a supernova signature associated with GRB 011121”, *Astrophysical Journal Letters*, **572**, L45–L49, (2002).
- [16] Bodenheimer, P., and Woosley, S. E., “A two-dimensional supernova model with rotation and nuclear burning”, *The Astrophysical Journal*, **269**, 281–291, (1983).
- [17] Bonazzola, S., and Marck, J. A., “Efficiency of gravitational radiation from axisymmetric and 3 D stellar collapse. I - Polytropic case”, *Astronomy & Astrophysics*, **267**, 623–633, (1993).
- [18] Bondi, H., van der Burg, M. G. J., and Metzner, A. W. K., “Gravitational waves in general relativity, VII. Waves from axi-symmetric isolated systems”, *Proceedings of the Royal Society A*, **269**, 21–52, (1962).
- [19] Brown, G. E., and Bethe, H. A., “A scenario for a large number of low-mass black holes in the Galaxy”, *The Astrophysical Journal*, **423**, 659–664, (1994).
- [20] Brown, J. D., “Astrophysical sources for ground-based gravitational wave detectors”, in Centrella, J. M., ed., *AIP conference Proceedings*, volume 575, American Institute of Physics, New York, (2001).
- [21] Buchdahl, H. A., “General relativistic fluid spheres”, *Physical Review*, **116**, 1027–1034, (1959).
- [22] Burrows, A., and Hayes, J., “Pulsar recoil and gravitational radiation due to asymmetrical stellar collapse and explosion”, *Physical Review Letters*, **76**, 352–355, (1996).
- [23] Burrows, A., and Lattimer, J. M., “The birth of neutron stars”, *The Astrophysical Journal*, **307**, 178–196, (1986).
- [24] Cappellaro, E., Turatto, M., Tsvetkov, D. Y., Bartunov, O. S., Pollas, C., Evans, R., and Hamuy, M., “The rate of supernovae from the combined sample of five searches”, *Astronomy & Astrophysics*, **322**, 431–441, (1997).
- [25] Chandrasekhar, S., “Solutions of two problems in the theory of gravitational radiation”, *Physical Review Letters*, **24**, 611–615, (1970).
- [26] Clark, D. H., and Stephenson, F. R., *The historical supernovae*, (Pergamon Press, Oxford, 1977).
- [27] Colella, P., and Woodward, P. R., “The piecewise parabolic method (PPM) for gas-dynamical simulations”, *Journal of Computational Physics*, **54**, 174–201, (1984).
- [28] Corkill, R. W., and Stewart, J. M., “Numerical methods for the characteristic initial value problem and the evolution of the vacuum field equations for space-times with two Killing vectors”, *Proceedings to the Royal Society London A*, **386**, 373–391, (1983).

- 
- [29] Cowling, T. G., “The non-radial oscillations of polytropic stars”, *Monthly Notices of the Royal Astronomical Society*, **101**, 367–375, (1941).
- [30] Dimmelmeier, H., Font, J. A., and Müller, E., “Gravitational waves from relativistic rotational core collapse”, *Astrophysical Journal Letters*, **560**, L163–L166, (2001).
- [31] Dimmelmeier, H., Font, J. A., and Müller, E., “Relativistic simulations of rotational core collapse I. Methods, initial models, and code tests”, *Astronomy & Astrophysics*, **388**, 917–935, (2002).
- [32] Dimmelmeier, H., Font, J. A., and Müller, E., “Relativistic simulations of rotational core collapse II. Collapse dynamics and gravitational radiation”, *Astronomy & Astrophysics*, **393**, 523–542, (2002).
- [33] Donat, R., and Marquina, A., “Capturing shock reflections: an improved flux formula”, *Journal of Computational Physics*, **146**, 42–58, (1996).
- [34] Eddington, A. S., *The mathematical theory of relativity*, (Cambridge University Press, Cambridge, 1923).
- [35] Einfeldt, B., “On Godunov-type methods for gas dynamics”, *SIAM Journal of Numerical Analysis*, **25**, 294–318, (1988).
- [36] Evans, C. R., “An approach for calculating axisymmetric gravitational collapse”, in *Dynamical Spacetimes and Numerical Relativity*, 3–39, Cambridge University Press, Cambridge, (1986).
- [37] Filippenko, A. V., “Optical spectra of supernovae”, *Annual Review of Astronomy & Astrophysics*, **35**, 309–355, (1997).
- [38] Finn, L. S., “Supernovae, gravitational radiation, and the quadrupole formula”, in *Frontiers in numerical relativity*, 126–145, Cambridge University Press, Cambridge, (1989).
- [39] Finn, L. S., and Evans, C. R., “Determining gravitational radiation from Newtonian self-gravitating systems”, *The Astrophysical Journal*, **351**, 588–600, (1990).
- [40] Font, J. A., “Numerical hydrodynamics in general relativity”, *Living Reviews in Relativity*, **3**, 2, (2000).
- [41] Font, J. A., Dimmelmeier, H., Gupta, A., and Stergioulas, N., “Axisymmetric modes of rotating relativistic stars in the Cowling approximation”, *Monthly Notices of the Royal Astronomical Society*, **325**, 1463–1470, (2001).
- [42] Font, J. A., Goodale, T., Iyer, S., Miller, M., Rezzolla, L., Seidel, E., Stergioulas, N., Suen, W., and Tobias, M., “Three-dimensional numerical general relativistic hydrodynamics. II. Long-term dynamics of single relativistic stars”, *Physical Review D*, **65**, 84024+, (2002).
- [43] Font, J. A., Miller, M., Suen, W., and Tobias, M., “Three-dimensional numerical general relativistic hydrodynamics: Formulations, methods, and code tests”, *Physical Review D*, **61**, 44011+, (2000).

- 
- [44] Font, J. A., Stergioulas, N., and Kokkotas, K. D., “Non-linear hydrodynamical evolution of rotating relativistic stars: numerical methods and code tests”, *Monthly Notices of the Royal Astronomical Society*, **313**, 678–688, (2000).
- [45] Frauendiener, J., “Conformal infinity”, *Living Reviews in Relativity*, **3**, 4, (2000).
- [46] Friedman, J. L., and Schutz, B. F., “Secular instability of rotating Newtonian stars”, *The Astrophysical Journal*, **222**, 281–296, (1978).
- [47] Friedrich, H., “On the regular and the asymptotic characteristic initial value problem for Einstein’s vacuum field equations”, *Proceedings to the Royal Society London A*, **375**, 169–184, (1981).
- [48] Friedrich, H., “Cauchy problems for the conformal vacuum field equations in general relativity”, *Communications of Mathematical Physics*, **91**, 445–472, (1983).
- [49] Fryer, C. L., and Heger, A., “Core-collapse simulations of rotating stars”, *The Astrophysical Journal*, **541**, 1033–1050, (2000).
- [50] Fryer, C. L., Holz, D. E., and Hughes, S. A., “Gravitational wave emission from core collapse of massive stars”, *The Astrophysical Journal*, **565**, 430–446, (2002).
- [51] Godlewski, E., and Raviart, P.-A., *Hyperbolic systems of conservation laws*, (Ellipses, Paris, 1991).
- [52] Godlewski, E., and Raviart, P.-A., *Numerical approximation of hyperbolic systems of conservation laws*, (Springer, Paris, 1996).
- [53] Godunov, S. K., “A finite difference method for the numerical computation and discontinuous solutions of the equations of fluid dynamics”, *Mat. Sb.*, **47**, 271, (1959).
- [54] Goldreich, P., and Weber, S. V., “Homologously collapsing stellar cores”, *The Astrophysical Journal*, **238**, 991–997, (1980).
- [55] Gómez, R., “Gravitational waveforms with controlled accuracy”, *Physical Review D*, **64**, 24007+, (2001).
- [56] Gómez, R., Husa, S., Lehner, L., and Winicour, J., “Gravitational waves from a fissioning white hole”, *Physical Review D*, **66**, 064019+, (2002).
- [57] Gómez, R., Laguna, P., Papadopoulos, P., and Winicour, J., “Cauchy-characteristic evolution of Einstein-Klein-Gordon systems”, *Physical Review D*, **54**, 4719–4727, (1996).
- [58] Gómez, R., Lehner, L., Marsa, R. L., Winicour, and et al., “Stable characteristic evolution of generic three-dimensional single-black-hole spacetimes”, *Physical Review Letters*, **80**, 3915–3918, (1998).
- [59] Gómez, R., Lehner, L., Papadopoulos, P., and Winicour, J., “The eth formalism in numerical relativity”, *Classical and Quantum Gravity*, **14**, 977–990, (1997).
- [60] Gómez, R., Papadopoulos, P., and Winicour, J., “Null cone evolution of axisymmetric vacuum space-times”, *Journal of Mathematical and Physical Sciences*, **35**, 4184–4204, (1994).



- 
- [61] Gómez, R., Reilly, P., Winicour, J., and Isaacson, R. A., “Post-Newtonian behavior of the Bondi mass”, *Physical Review D*, **47**, 3292–3302, (1993).
- [62] Gómez, R., and Winicour, J., “Asymptotics of gravitational collapse of scalar waves”, *Journal of Mathematical and Physical Sciences*, **33**, 1445–1457, (1992).
- [63] Gómez, R., and Winicour, J., “Gravitational wave forms at finite distances and at null infinity”, *Physical Review D*, **45**, 2776–2782, (1992).
- [64] Gómez, R., Winicour, J., and Isaacson, R., “Evolution of scalar fields from characteristic data”, *Journal of Computational Physics*, **98**, 11–25, (1992).
- [65] Gómez, R., Winicour, J., and Schmidt, B. G., “Newman-Penrose constants and the tails of self-gravitating waves”, *Physical Review D*, **49**, 2828–2836, (1994).
- [66] Grishchuk, L. P., Lipunov, V. M., Postnov, K. A., Prokhorov, M. E., and Sathyaprakash, B. S., “Gravitational wave astronomy: in anticipation of first sources to be detected”, *Physics-Uspokhi*, **71**, 3–59, (2001).
- [67] Gundlach, C., Price, R. H., and Pullin, J., “Late-time behavior of stellar collapse and explosions. I. Linearized perturbations”, *Physical Review D*, **49**, 883–889, (1994).
- [68] Gundlach, C., Price, R. H., and Pullin, J., “Late-time behavior of stellar collapse and explosions. II. Nonlinear evolution”, *Physical Review D*, **49**, 890–899, (1994).
- [69] Harten, A., Lax, P. D., and van Leer, B., “On upstream differencing and Godunov-type schemes for hyperbolic conservations laws”, *SIAM Review*, **25**, 35–61, (1983).
- [70] Hawley, S. H., and Choptuik, M. W., “Boson stars driven to the brink of black hole formation”, *Physical Review D*, **62**, 104024+, (2000).
- [71] Hillebrandt, W., “The equation of state of supernova and neutron star matter”, in *Proceedings of the international school of physics “Enrico Fermi”*, 399–437, North-Holland, Amsterdam, (1991).
- [72] Hughes, S. A., Marka, S., Bender, P. L., and Hogan, C. J., “New physics and astronomy with the new gravitational-wave observatories”, *astro-ph/0110349*, (2001).
- [73] Hulse, R. A., and Taylor, J. H., “Discovery of a pulsar in a binary system”, *Astrophysical Journal Letters*, **195**, L51–L53, (1975).
- [74] Imshennik, V. S., and Nadyozhin, D. K., “Supernova 1987A and the formation of rotating neutron stars”, *Soviet Astronomy Letters*, **18**, 79–88, (1992).
- [75] Isaacson, R. A., Welling, J. S., and Winicour, J., “Null cone computation of gravitational radiation”, *Journal of Mathematical and Physical Sciences*, **24**, 1824–1834, (1983).
- [76] Isaacson, R. A., Welling, J. S., and Winicour, J., “Extension of the Einstein quadrupole formula”, *Physical Review Letters*, **53**, 1870–1872, (1984).
- [77] Janka, H., Kifonidis, K., and Rampp, M., “Supernova explosions and neutron star formation”, in *Physics of Neutron Star Interiors*, 333+, Ed. by D. Blaschke, N.K. Glendenning and A. Sedrakian, Lecture Notes in Physics, vol. 578, (2001).

- 
- [78] Janka, H.-T., and Mönchmeyer, R., “Hydrostatic post bounce configurations of collapsed rotating iron cores: Neutrino emission”, *Astronomy & Astrophysics*, **226**, 69–87, (1989).
- [79] Janka, H.-T., Zwerger, T., and Mönchmeyer, R., “Does artificial viscosity destroy prompt type-II supernova explosions?”, *Astronomy & Astrophysics*, **268**, 360–368, (1993).
- [80] Kalogera, V., Narayan, R., Spergel, D. N., and Taylor, J. H., “The coalescence rate of double neutron star systems”, *The Astrophysical Journal*, **556**, 340–356, (2001).
- [81] Kifonidis, K., Plewa, T., Janka, H.-T., and Müller, E., “Nucleosynthesis and clump formation in a core-collapse supernova”, *Astrophysical Journal Letters*, **531**, L123–L126, (2000).
- [82] Kokkotas, K., “private communication”, (2001).
- [83] Kokkotas, K. D., “Pulsating relativistic stars”, in *Relativistic Gravitation and Gravitational Radiation*, 89–102, Cambridge University Press, Cambridge, (1997).
- [84] Kokkotas, K. D., and Andersson, N., “Oscillations and instabilities of relativistic stars”, in *Proceedings of SIGRAV XIV*, Springer, (2001).
- [85] Kokkotas, K. D., and Schmidt, B. G., “Quasi-normal modes of stars and black holes”, *Living Reviews in Relativity*, **2**, 2, (1999).
- [86] Lai, D., “Neutron star kicks and asymmetric supernovae”, in *Physics of Neutron Star Interiors*, 424+, Ed. by D. Blaschke, N.K. Glendenning and A. Sedrakian, Lecture Notes in Physics, vol. 578, (2001).
- [87] Landau, L., and Lifshitz, E., *The classical theory of fields*, (Addison-Wesley, New York, 1961).
- [88] Lattimer, J. M., and Prakash, M., “Neutron star structure and the equation of state”, *The Astrophysical Journal*, **550**, 426–442, (2001).
- [89] Lehner, L., “A dissipative algorithm for wave-like equations in the characteristic formulation”, *Journal of Computational Physics*, **149**, 59–74, (1999).
- [90] LeVeque, R. J., *Numerical methods for conservation laws*, (Birkhäuser, Basel, 1992).
- [91] Linke, F., *General relativistic simulations of collapsing supermassive stars*, (Diploma thesis, TU Munich, 2000).
- [92] Linke, F., Font, J. A., Janka, H.-T., Müller, E., and Papadopoulos, P., “Spherical collapse of supermassive stars: Neutrino emission and gamma-ray bursts”, *Astronomy & Astrophysics*, **376**, 568–579, (2001).
- [93] Longair, M. S., *High energy astrophysics*, (Cambridge University Press, Cambridge, 1994).
- [94] MacFadyen, A. I., and Woosley, S. E., “Collapsars: Gamma-ray bursts and explosions in “failed supernovae””, *The Astrophysical Journal*, **524**, 262–289, (1999).
- [95] Marsa, R. L., and Choptuik, M. W., “Black-hole-scalar-field interactions in spherical symmetry”, *Physical Review D*, **54**, 4929–4943, (1996).

- 
- [96] Marti, J. M., and Müller, E., “Numerical hydrodynamics in special relativity”, *Living Reviews in Relativity*, **2**, 3, (1999).
- [97] May, M. M., and White, R. H., “Hydrodynamic calculations of general-relativistic collapse”, *Physical Review*, **141**, 1232–1241, (1966).
- [98] Mészáros, P., “Gamma-Ray bursts: Accumulating afterglow implications, progenitor clues, and prospects”, *Science*, **291**, 79–84, (2001).
- [99] Mészáros, P., “Theories of gamma-ray bursts.”, *Annual Review of Astronomy & Astrophysics*, **40**, 137–169, (2002).
- [100] Migdal, A. B., “ $\pi$  Condensation in nuclear matter”, *Usp. Fiz. Nauk*, **105**, 2209, (1971).
- [101] Miller, J. C., and Motta, S., “Computations of spherical gravitational collapse using null slicing”, *Classical and Quantum Gravity*, **6**, 185–193, (1989).
- [102] Minkowski, R., “Spectra of supernovae”, *Publications of the Astronomical Society of the Pacific*, **53**, 224–225, (1941).
- [103] Misner, C. W., Thorne, K. S., and Wheeler, J. A., *Gravitation*, (W.H. Freeman, New York, 1970).
- [104] Mönchmeyer, R., and Müller, E., “A conservative second-order difference scheme for curvilinear coordinates - Part One - Assignment of variables on a staggered grid”, *Astronomy & Astrophysics*, **217**, 351–367, (1989).
- [105] Mönchmeyer, R., Schäfer, G., Müller, E., and Kates, R. E., “Gravitational waves from the collapse of rotating stellar cores”, *Astronomy & Astrophysics*, **246**, 417–440, (1991).
- [106] Müller, E., “Gravitational radiation from core-collapse supernovae”, *Classical and Quantum Gravity*, **14**, 1455–1460, (1997).
- [107] Müller, E., “Simulation of astrophysical fluid flow”, in *Saas-Fee Advanced Course 27: Computational Methods for Astrophysical Fluid Flow*, 343+, (1998).
- [108] Müller, E., and Hillebrandt, W., “The collapse of rotating stellar cores”, *Astronomy & Astrophysics*, **103**, 358–366, (1981).
- [109] Murdin, P., and Murdin, L., *Supernovae*, (Cambridge University Press, Cambridge, 1985).
- [110] N. N., <http://csep10.phys.utk.edu/guidry/violence/supernovae.html>, (Online Journal Through Astronomy, 2002).
- [111] Nakamura, T., “General relativistic collapse of axially symmetric stars Leading to the Formation of Rotating Black Holes”, *Progress of Theoretical Physics*, **65**, 1876–1890, (1981).
- [112] New, K. C., “Gravitational waves from gravitational collapse”, *gr-qc/0206041*, (2002).
- [113] Noh, W. F., “Errors for calculations of strong shocks using an artificial viscosity and an artificial heat flux”, *Journal of Computational Physics*, **72**, 78–120, (1987).

- 
- [114] Paczynski, B., “Are gamma-ray bursts in star-forming regions?”, *Astrophysical Journal Letters*, **494**, L45–L48, (1998).
- [115] Papadopoulos, P., *Algorithms for the gravitational characteristic initial value problem*, (Ph.D. thesis, University of Pittsburgh, 1993).
- [116] Papadopoulos, P., “Nonlinear harmonic generation in finite amplitude black hole oscillations”, *Physical Review D*, **65**, 84016+, (2002).
- [117] Papadopoulos, P., and Font, J. A., “Analysis of relativistic hydrodynamics in conservation form”, *gr-qc/9912094*, (1999).
- [118] Papadopoulos, P., and Font, J. A., “Matter flows around black holes and gravitational radiation”, *Physical Review D*, **59**, 044014+, (1999).
- [119] Papadopoulos, P., and Font, J. A., “Relativistic hydrodynamics on spacelike and null surfaces: Formalism and computations of spherically symmetric spacetimes”, *Physical Review D*, **61**, 024015+, (2000).
- [120] Papadopoulos, P., and Font, J. A., “Imprints of accretion on gravitational waves from black holes”, *Physical Review D*, **63**, 044016+, (2001).
- [121] Papadopoulos, P., and Laguna, P., “Cauchy-characteristic evolution of Einstein-Klein-Gordon systems: The black hole regime”, *Physical Review D*, **55**, 2038–2043, (1997).
- [122] Pavlidou, V., Tassis, K., Baumgarte, T. W., and Shapiro, S. L., “Radiative falloff in neutron star spacetimes”, *Physical Review D*, **62**, 84020+, (2000).
- [123] Penrose, R., “Asymptotic properties of fields and space-times”, *Physical Review Letters*, **10**, 66–68, (1963).
- [124] Press, W. H., “Gravitational radiation from sources which extend into their own wave zone”, *Physical Review D*, **15**, 965–968, (1977).
- [125] Price, R. H., “Nonspherical perturbations of relativistic gravitational collapse. I. Scalar and gravitational perturbations”, *Physical Review D*, **5**, 2419–2438, (1972).
- [126] Price, R. H., “Nonspherical perturbations of relativistic gravitational collapse. II. Integer-spin, zero-rest-mass fields”, *Physical Review D*, **5**, 2439–2454, (1972).
- [127] Rampp, M., Müller, E., and Ruffert, M., “Simulations of non-axisymmetric rotational core collapse”, *Astronomy & Astrophysics*, **332**, 969–983, (1998).
- [128] Romero, J. V., Ibanez, J. M. A., Marti, J. M. A., and Miralles, J. A., “A new spherically symmetric general relativistic hydrodynamical code”, *The Astrophysical Journal*, **462**, 839–854, (1996).
- [129] Ruoff, J., “New approach to the evolution of neutron star oscillations”, *Physical Review D*, **63**, 064018+, (2001).
- [130] Ruoff, J., “private communication”, (2001).

- 
- [131] Sachs, R. K., “Gravitational waves in general relativity: VIII Waves in asymptotically flat space-times”, *Proceedings to the Royal Society A*, **269**, 103, (1962).
- [132] Sawyer, R. F., and Scalapino, D. J., “Pion condensation in superdense nuclear matter”, *Physical Review D*, **7**, 953–964, (1973).
- [133] Shapiro, S. L., and Teukolsky, S. A., *Black holes, white dwarfs, and neutron stars: The physics of compact objects*, (Wiley, New York, 1983).
- [134] Shibata, M., “Axisymmetric simulations of rotating stellar collapse in full general relativity —Criteria for prompt collapse to black holes—”, *Progress of Theoretical Physics*, **104**, 325–358, (2000).
- [135] Shibata, M., “in preparation”, (2002).
- [136] Shibata, M., Baumgarte, T. W., and Shapiro, S. L., “Stability and collapse of rapidly rotating, supramassive neutron stars: 3D simulations in general relativity”, *Physical Review D*, **61**, 044012+, (2000).
- [137] Shu, C.-W., and Osher, S., “Efficient implementation of essentially non-oscillatory shock-capturing schemes, II”, *Journal of Computational Physics*, **83**, 32–78, (1989).
- [138] Siebel, F., Font, J. A., Müller, E., and Papadopoulos, P., “Simulating the dynamics of relativistic stars via a light-cone approach”, *Physical Review D*, **65**, 64038+, (2002).
- [139] Siebel, F., Font, J. A., and Papadopoulos, P., “Scalar field induced oscillations of relativistic stars and gravitational collapse”, *Physical Review D*, **65**, 24021+, (2002).
- [140] Stairs, I. H., Arzoumanian, Z., Camilo, F., Lyne, A. G., Nice, D. J., Taylor, J. H., Thorsett, S. E., and Wolszczan, A., “Measurement of relativistic orbital decay in the PSR B1534+12 binary system”, *The Astrophysical Journal*, **505**, 352–357, (1998).
- [141] Stark, R. F., and Piran, T., “Gravitational-wave emission from rotating gravitational collapse”, *Physical Review Letters*, **55**, 891–894, (1985).
- [142] Stark, R. F., and Piran, T., “A general relativistic code for rotating axisymmetric configurations and gravitational radiation: Numerical methods and tests”, *Computational Physics Reports*, **5**, 221–264, (1987).
- [143] Stergioulas, N., “Rotating stars in relativity”, *Living Reviews in Relativity*, **1**, 8, (1998).
- [144] Stewart, J. M., “The characteristic initial value problem in general relativity”, in *NATO Advanced Research Workshop on Astrophysical Radiation Hydrodynamics*, 531+, Ed. by Karl-Heinz A. Winkler, Michael L. Norman, D. Reidel Publishing Co., Dordrecht, Holland, (1986).
- [145] Symbalisty, E. M. D., “Magnetorotational iron core collapse”, *The Astrophysical Journal*, **285**, 729–746, (1984).
- [146] Tamburino, L. A., and Winicour, J. H., “Gravitational fields in finite and conformal Bondi frames”, *Physical Review*, **150**, 1039–1053, (1966).

- 
- [147] Taylor, J. H., and Weisberg, J. M., “A new test of general relativity - Gravitational radiation and the binary pulsar PSR 1913+16”, *The Astrophysical Journal*, **253**, 908–920, (1982).
- [148] Tooper, R. F., “Adiabatic fluid spheres in general relativity.”, *The Astrophysical Journal*, **142**, 1541–1562, (1965).
- [149] van Leer, B. J., “Towards the ultimate conservative difference scheme. IV. A new approach to numerical convection”, *Journal of Computational Physics*, **23**, 276–299, (1977).
- [150] van Leer, B. J., “Towards the ultimate conservative difference scheme. V. A second order sequel to Godunov’s method”, *Journal of Computational Physics*, **32**, 101–136, (1979).
- [151] Vietri, M., and Stella, L., “A gamma-ray burst model with small baryon contamination”, *Astrophysical Journal Letters*, **507**, L45–L48, (1998).
- [152] Wald, R. M., *General relativity*, (University of Chicago Press, Chicago, 1984).
- [153] Weber, F., “Strangeness in neutron stars”, *astro-ph/0008376*, (2000).
- [154] Weber, J., “Evidence for discovery of gravitational radiation”, *Physical Review Letters*, **22**, 1320–1324, (1969).
- [155] Weber, J., “Anisotropy and polarization in the gravitational-radiation experiments”, *Physical Review Letters*, **25**, 180–184, (1970).
- [156] Weisberg, J. M., and Taylor, J. H., “Observations of post-Newtonian timing effects in the binary pulsar PSR 1913 + 16”, *Physical Review Letters*, **52**, 1348–1350, (1984).
- [157] Wilson, J. R., “Supernovae and post-collapse behavior”, in *Numerical Astrophysics*, 422–434, Ed. by J.M. Centrella, J.M. LeBlanc and R.L. Bowers, Jones and Bartlett Publishers, Boston, (1985).
- [158] Wilson, J. R., Mathews, G. J., and Marronetti, P., “Relativistic numerical model for close neutron-star binaries.”, *Physical Review D*, **54**, 1317–1331, (1996).
- [159] Winicour, J., “Newtonian gravity on the null cone”, *Journal of Mathematical and Physical Sciences*, **24**, 1193–1198, (1983).
- [160] Winicour, J., “Null infinity from a quasi-Newtonian view”, *Journal of Mathematical and Physical Sciences*, **25**, 2506–2514, (1984).
- [161] Winicour, J., “The quadrupole radiation formula”, *General relativity and gravitation*, **19**, 281–287, (1987).
- [162] Winicour, J., “A new way to make waves”, *Proceedings of CIMENICS 2000*, (2000).
- [163] Winicour, J., “Characteristic evolution and matching”, *Living Reviews in Relativity*, **4**, 3, (2001).
- [164] Woosley, S. E., “Gamma-ray bursts from stellar mass accretion disks around black holes”, *The Astrophysical Journal*, **405**, 273–277, (1993).

- [165] Yahil, A., “Self-similar stellar collapse”, *The Astrophysical Journal*, **265**, 1047–1055, (1983).
- [166] Yahil, A., and Lattimer, J. M., “Supernovae for pedestrians”, in *NATO ASIC Proc. 90: Supernovae: A Survey of Current Research*, 53–70, (1982).
- [167] Yamada, S., and Sato, K., “Numerical study of rotating core collapse in supernova explosions”, *The Astrophysical Journal*, **434**, 268–276, (1994).
- [168] Yoshida, S., and Kojima, Y., “Accuracy of the relativistic Cowling approximation in slowly rotating stars”, *Monthly Notices of the Royal Astronomical Society*, **289**, 117–122, (1997).
- [169] Zwerger, T., and Müller, E., “Dynamics and gravitational wave signature of axisymmetric rotational core collapse.”, *Astronomy & Astrophysics*, **320**, 209–227, (1997).





# Acknowledgment

It is a pleasure to thank Ewald Müller, José Antonio Font and Philippos Papadopoulos for their excellent work in advising me during this PhD. In particular, I would like to thank Ewald Müller for his steady support and the many helpful discussions. He always was open for any problem which I confronted him with. I am very grateful to José Antonio Font for his steady encouragements, the useful help in general relativistic fluid dynamics and numerical problems in general, no matter whether in discussions, per e-mail or on the phone. And last but not least many thanks to Philippos Papadopoulos, who - not only during my half year stay in Portsmouth - helped me immensely with his analytical reasoning and profound knowledge of characteristic numerical relativity and well beyond.

I further thank Jeffrey Winicour, Nigel Bishop and Luis Lehner for helpful comments and discussions concerning the characteristic field equations of general relativity.

Concerning the studies of the neutron star - scalar field interaction, I am grateful to Johannes Ruoff for kindly providing us the frequencies of the fundamental modes of the neutron star models of Section 5.3.1, obtained with his perturbation code. Further thanks to Carsten Gundlach and José Maria Ibañez for helpful comments on this project.

Concerning the studies of neutron star pulsations, it is a pleasure to thank Kostas Kokkotas, who calculated mode frequencies for us using his linear perturbation code. I also would like to thank Nick Stergioulas for helpful comments and discussions.

At the MPA für Astrophysik, I am especially grateful to Harald Dimmelmeier, who helped me a lot sharing his knowledge on supernova core collapse, and performing reference runs with his code. I would also like to thank the other members of the hydro group for many helpful suggestions.